VIBRATION ANALYSIS FOR EARLY DETECTION OF BEARING FAILURES

GAM KHENG SHIANG

UNIVERSITI TUNKU ABDUL RAHMAN

VIBRATION ANALYSIS FOR EARLY DETECTION OF BEARING FAILURES

GAM KHENG SHIANG

A project report submitted in partial fulfilment of the requirements for the award of Bachelor of Mechanical Engineering with Honours

Lee Kong Chian Faculty of Engineering and Science
Universiti Tunku Abdul Rahman

October 2024

DECLARATION

I hereby declare that this project report is based on my original work except for citations and quotations which have been duly acknowledged. I also declare that it has not been previously and concurrently submitted for any other degree or award at UTAR or other institutions.

Signature : 翔

Name : GAM KHENG SHIANG

ID No. : 21UEB00685

Date : 07-10-2024

APPROVAL FOR SUBMISSION

I certify that this project report entitled **"VIBRATION ANALYSIS FOR EARLY DETECTION OF BEARING FAILURES"** was prepared by **GAM KHENG SHIANG** has met the required standard for submission in partial fulfilment of the requirements for the award of Bachelor of Mechanical Engineering with Honours at Universiti Tunku Abdul Rahman.

Approved by,

Signature :

Supervisor : Dr Kam Heng Keong

Date : 07/10/2024

Signature : -

Co-Supervisor : -

Date : -

The copyright of this report belongs to the author under the terms of the copyright Act 1987 as qualified by Intellectual Property Policy of Universiti Tunku Abdul Rahman. Due acknowledgement shall always be made of the use of any material contained in, or derived from, this report.

© 2024, GAM KHENG SHIANG. All right reserved.

ACKNOWLEDGEMENTS

I would like to thank everyone who contributed to the successful completion of this project. First, I would like to express my gratitude to my research supervisor, Dr. Kam Heng Keong, for his valuable advice and guidance throughout the development of the research. Next, I would like to extend my gratitude to Ir. Dr. Ng Kean Eng from ICA40 Sdn. Bhd. for his kind words, invaluable guidance, and support throughout the course of my project. His passion for research and strong work ethic have been a source of inspiration for me. I am also deeply thankful to the lab staff in the university’s mechanical workshop, particularly Mr. Mohd Rosnan, Mr. Mohd Izhar, and Mr. Ho. Their immense help with the practical and hands-on aspects of the project was crucial to its completion. The fabrication of the test rig components and the preparation of the bearing samples would not have been possible without their advice and assistance. In addition, I would like to thank Mr. Chung from MITS Solutions Asia for generously providing me the opportunity to use their learning kit, which played a crucial role in advancing my research. Last but not least, I would like to express my love and gratitude to my parents and friends, whose help and encouragement supported me along the way.

ABSTRACT

Bearing failures are a leading cause of rotating machinery failures in industries such as oil and gas, manufacturing, and power generation. Early detection of bearing failures using Predictive Maintenance (PdM) is critical for minimizing downtime and optimizing maintenance strategies. The aim of this study is to investigate the vibration characteristics of defective bearings by developing a reliable vibration monitoring system. The vibration monitoring algorithm utilizes time-domain parameters, frequency domain analysis, and envelope analysis to assess bearing conditions. The vibration indicators utilized in this study include K-factor, root mean square (RMS) acceleration, peak acceleration, crest factor, kurtosis, RMS velocity, RMS displacement, and peak-to-peak displacement. This research specifically focuses on types of bearing damage, including lubricant contamination, chemical corrosion, and mechanical damage. The key findings of this study highlight several important observations in bearing fault detection. First, the use of the envelope spectrum has proven to be highly valuable in visualizing specific bearing fault frequencies, which makes it a powerful tool for fault detection. The successful detection of the Ball Pass Frequency Outer (BPFO) was achieved with an error margin ranging from 0.31% to 1.24%. It was also observed that the K-factor, RMS acceleration, and peak acceleration are sensitive to operating speed, which may pose challenges in variable-speed applications. For indicators without speed dependency, thresholds are established based on the two-sigma criteria. The crest factor threshold is set at 7.49, while the kurtosis threshold is established at 4.11. The algorithm's analysis results were consistent with the physical inspection of disassembled bearings. In comparison to a commercial monitoring system, the crest factor was identified as the most consistent indicator for evaluating bearing condition, demonstrating a percentage difference ranging from 2.63% to 65.19%. In summary, the combination of RMS acceleration and kurtosis is proposed as a reliable method for identifying bearing faults.

TABLE OF CONTENTS

CHAPTER

LIST OF TABLES

LIST OF FIGURES

LIST OF SYMBOLS / ABBREVIATIONS

PM	preventive maintenance
PdM	predictive maintenance
ISO	International Organization for Standardization
RMS	root mean square
FFT	Fast Fourier Transform
IFFT	Inverse Fast Fourier Transform
FTF	fundamental train frequency
BPFO	ball pass frequency outer
BPFI	ball pass frequency inner
BSF	ball spin frequency
CF	crest factor
STFT	Short-Time Fourier Transform
IF	Instantaneous frequency
SK	Spectral kurtosis
HT	Hilbert transform
SPC	statistical process control
CUSUM	cumulative sum
RUL	remaining useful life
SVM	Support Vector Machines
RLS	Recursive Least Squares
DAQ	data acquisition system
VFD	variable frequency drive
AC	alternating current
HCl	hydrochloric acid
VI	Virtual Instrument
TDMS	Technical Data Management Streaming
MEMS	micro-electromechanical systems

LIST OF APPENDICES

CHAPTER 1

INTRODUCTION

1.1 General Introduction

In the modern industrial era, rotating machinery is crucial to the operation of industries such as oil and gas, manufacturing, and power generation. The reliability and efficiency of rotating machinery are critical factors which affect the productivity of industrial operations. In the event of a rotating machinery failure, unplanned downtime of the process will cause a loss of productivity and incur a substantial repair cost. To avoid these adverse consequences, the maintenance of rotating machinery is a high priority in any industry.

As one of the critical components in rotating machinery, rolling element bearing is frequently the subject of study. As bearings are subjected to repeated cyclic loading during their operation, bearings that have been extensively used are prone to failure. The main causes of bearing failure include fatigue, contamination, poor lubrication, overloading, and overspeeding. To minimize the risk of critical failure, proper maintenance strategy needs to be implemented.

Conventionally, the most prevalent strategy in the industry is the implementation of preventive maintenance (PM). PM is the predetermination of maintenance tasks that are based on the functionality of equipments and the expected lifetimes of their components. In practice, this means that maintenance activity is performed in regular intervals based on guidance from equipment manufacturer. While this conventional strategy has its advantages in terms of simplicity, it is susceptible to changes in machinery condition and the occurrence of unnecessary maintenance.

1.2 Importance of the Study

To mitigate the limitation of conventional maintenance strategies, this study aims to provide a better insight into the field of predictive maintenance (PdM). PdM not only aims for failure prevention, but it also strives to improve the process performance by extending the lifespan of equipment. In a conventional approach, equipment failure can occur unexpectedly, even if the scheduled maintenance interval has not been reached. Moreover, it might not be possible to define a suitable maintenance interval especially when the time-to-failure varies significantly. PdM addresses these issues by monitoring the equipment condition with continuous or periodical detection of failure indicators. By performing maintenance work at the optimal time, the occurrence of unscheduled breakdown is reduced by 70% to 75% (Selcuk, 2016). Moreover, this improves the reliability of the equipment and enhances the efficiency of the process. The employment of PdM strategy also improves the cost-effectiveness of any industrial operation. In manufacturing, maintenance costs attributes to between 15% and 60% of the overall operational expenses (Zonta et al., 2020). Implementing PdM can help to avoid additional expenses incurred by over-maintenance or emergency repairs, leading to maintenance cost reduction of 25% to 30% (Selcuk, 2016). Conventionally, bearings are replaced at predetermined intervals without assessment of actual condition. The premature replacements of bearings lead to the waste in their remaining useful life. However, with PdM, the lifespan of bearings can be prolonged as their health state can be accurately evaluated.

1.3 Problem Statement

In the practical application of predictive maintenance, there are several concerns which necessitates a targeted study. While some monitoring methods are capable of general bearing fault detection, they lack a holistic approach in determining the location of the defect in the bearing. This implies that only the replacement of bearings can be performed, while the identification and correction of the root cause remains hindered. Next, some methods are limited to diagnostic only, whereby the remaining useful life of the bearing and any potential future failures cannot be determined. This proves to be an issue in the planning of maintenance schedule as the failure time of the bearing cannot be estimated. Furthermore, there is a lack of comprehensive studies on smaller bearings and low-power motors. These smaller components are important in various applications where space, weight, and energy efficiency are prioritized. Industries that rely on smaller machinery such as precision manufacturing and small-scale industrial equipment will face challenges in effectively detecting early bearing failures using the available methods.

1.4 Aim and Objectives

The primary aim of this study is to develop a vibration monitoring system for the early detection of bearing failure. The objectives of this study are listed below.

(i) To develop signal processing algorithms for the vibration analysis of bearing fault.
(ii) To investigate the relationship between vibration patterns and bearing failure modes.
(iii) To evaluate the effectiveness and robustness of the monitoring system through controlled experiments and real-world applications.

1.5 Scope and Limitation of the Study

The scope of this study will be centred on improving the monitoring of rolling element bearing based on the concept of Predictive Maintenance. This study will be directed on improving monitoring system based on vibration analysis instead of other monitoring techniques. Hence, the accelerometer will be the sensor employed in the study. Techniques such as temperature monitoring, acoustic emission analysis, and oil analysis will not fall within the scope of the study. This study will be targeted at failure caused by bearings and its vibration data. Vibration which rises from faults in other machinery components such as gears, coupling, and shafts, will not be the centre of analysis. This also means that machinery issues such as unbalance, misalignment, and resonance will not be the target of analysis.

Due to the complex nature of bearing fault formation, the possible failure modes in this study will not be exhaustive. This study may not capture all possible bearing fault conditions in industrial settings, which leads to potential gap in fault detection. Next, the limitations of this study also arise from the limited range of bearing types tested. The threshold of the vibration indicators established may only be applicable to the particular bearing models examined. Therefore, it restricts the applicability of the findings to other bearing types unless further validation is conducted. Another limitation in this study is the compatibility between data acquisition hardware and signal processing software. The data acquisition module should be able to transfer data to the selected processing software without using any complicated middleware solutions. Lastly, complex diagnostics techniques will not be considered due to their high demand on computational time and power.

1.6 Contribution of the Study

This study makes several contributions to the field of bearing diagnostics. First, it evaluates the effectiveness and reliability of various vibration indicators in bearing monitoring. Next, it provides insights into the detection of localized faults in bearings through the use of envelope spectrum analysis. Lastly, it introduces various methods for inducing defects in bearings, offering new perspectives on bearing fault simulation.

1.7 Outline of the Report

This report consists of five chapters in total. Chapter 1 provides an introduction into background of the study, including the importance of predictive maintenance, the current problem statement, along with the objectives and contribution of the study. Chapter 2 is the literature review on researches performed by various academics. This chapter covers the review on bearing failure modes, review on bearing diagnostic methods and bearing prognostics methods. For instance, bearing diagnostic methods are further divided into time domain techniques, frequency domain analysis, and envelope analysis. Chapter 3 explains the methodology and work plan of the experiment. This chapter will elaborate on the experimental setup of the study. This includes the preparation of defective bearings, the development of vibration monitoring algorithm, and lastly the procedure for test rig setup and data collection. Chapter 4 presents and discusses the results obtained from the experiment. The vibration analysis of bearings will be analysed based on acceleration waveform, envelope spectrum, and vibration indicators. Moreover, the prediction of remaining useful life and the validation of algorithm will also be explored. Finally, Chapter 5 concludes the findings from the study and provides possible recommendations for future work.

CHAPTER 2

LITERATURE REVIEW

2.1 Introduction

In this chapter, a comprehensive overview of research relevant to bearing failure detection is provided. The main focus of this chapter is to explore bearing failure modes, bearing diagnostic methods, and prognostics techniques aimed at predicting bearing failures.

2.2 Review on Bearing Defects

In this subsection, various faults associated with bearings will be explored in detail while examining their underlying causes and failure mechanism.

In ISO 15243 standard, bearing failure modes are classified into six different categories which include rolling contact fatigue, wear, corrosion, electrical erosion, plastic deformation, and lastly cracking and fracture (International Organization for Standardization, 2017). On the other hand, Patidar and Soni (2013) classifies rolling element bearing faults into two categories, namely distributed defects and localized defects. Distributed defects include surface roughness, waviness, misaligned races, and off-size rolling elements. Distributed faults are not actual surface damages, instead they are irregularities in the bearing geometry due to imperfect manufacturing, faulty mounting, and misuse (Dolenc, Boškoski and Juričić, 2016). Localized defects are such as cracks, pits, and spalls on rolling element surfaces. These defects occur as a consequence of various failure modes that will be explored in the following section.

Surface roughness refers to irregularities or deviations such as peaks or valleys on the component surface. When surface roughness is significant, the ruggedness of the surface breaks through the lubricating film, comes in contact with the opposing surface, and results in increased vibration for the bearing (Kondhalkar and Diwakar, 2019). The stress distributions in near-surface region are proportional to the surface irregularities. High stress distribution is known to accelerates the creation of defects (Goepfert et al., 2008).

Waviness is defined as geometric imperfection of a ball, inner or outer race in a ball bearing. Waviness is always present in a ball bearing to varying degrees as a result of the manufacturing process, although it can also be generated by load or operating conditions (Jang and Jeong, 2004).

Upadhyay, Harsha and Jain (2009) differentiates waviness and surface roughness by their respective wavelengths. Surface roughness refers to surface features that are characterized by short wavelengths which are comparable to the contact width. Conversely, waviness refers to features with wavelengths much greater than contact width. Waviness extends over a greater distance and influences the macroscopic profile of the surface.

Misaligned races refers to a condition whereby the centreline of the inner race is not aligned with the centreline of the outer race. When bearing is misaligned, the rolling elements will exhibit uneven rolling paths. Typical causes of misalignment are improper assembly, bent shafts, and out-of-square shoulders on shafts or housings.

Off-size rolling elements refer to bearing rolling elements that deviate from the specified dimensions or tolerances. Off-sized balls increases the contact stiffness between the bearing ball and the raceway, especially when the diameter deviation is significant. This subsequently increase the local stress concentration at the contact area, which accelerates wear and degradation (Neisi et al., 2018).

2.3 Review on ISO 15243 Bearing Failure Modes

This subsection delves into the distinct types of failure modes categorized by ISO 15243 standard. These failure modes include fatigue, wear, corrosion, electrical erosion, plastic deformation, cracking, and facture.

2.3.1 Fatigue

Rolling contact fatigue is induced by the repeated stresses developed in the contacts between rolling elements and the bearing races. Fatigue can be classified into subsurface-initiated and surface-initiated.

Subsurface microcracks are initiated when the material undergoes structural changes under cyclic loading. Subsurface microcracks is often caused by inclusions (foreign particle) in bearing steel such as impurities or oxides. The propagation of these microcracks to the surface will result in the detachment of material which causes spalling. Sub-surface-initiated spalling is significantly influenced by the microstructure of the material which is inherently inhomogeneous and possesses a topological disorder. Topological disorder refers to the non-uniform arrangement of grains and grain boundaries, which give rise to regions of stress concentration (Raje and Sadeghi, 2009).

Fatigue can also be surface-initiated due to surface distress, which is the damage due to plastic deformation of the surface asperities (roughness). This leads to phenomenon such as smoothing, burnishing, and glazing. Contact between asperities is prompted by insufficient lubricant film thickness. Surface initiated fatigue can potentially lead to asperity microcracks and asperity microspalls as shown in Figure 2.1.

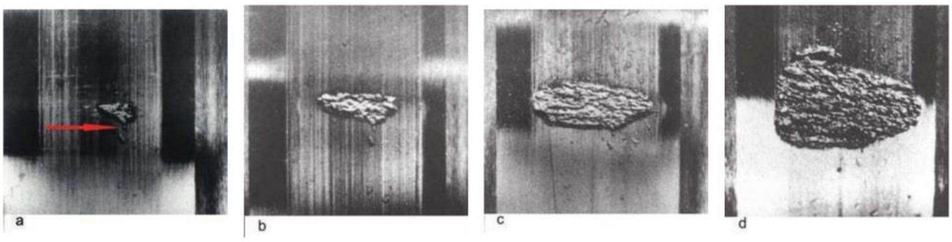

Figure 2.1: Progression of spall formation on bearing raceway (International Organization for Standardization, 2017).

2.3.2 Wear

Wear, which is the progressive removal of material from surface, can be classified into abrasive wear and adhesive wear. Abrasive wear is the result when a hard surface or particle is cutting or ploughing on another surface due to sliding action. The abrasive wear process is self-accelerating since the quantity of hard particles increases as the material is worn away. The worn surfaces typically take on a dull appearance, however polishing effect may occur if the abrasives are very fine.

Adhesive wear is identified by the transfer of material from one surface to another with frictional heat, while occasionally causes tempering or surface rehardening. Since this creates a localized stress concentration, the potential for cracking or spalling increases. Smearing (scuffing) occurs due to localized temperature spikes in poor lubrication conditions as shown in Figure 2.2.

Seizing occurs in severe cases of smearing. As opposed to wear, smearing is a sudden occurrence instead of an accumulated process.

In Figure 2.3, El-Thalji and Jantunen (2015) segmented the wear evolution of bearing faults into five distinct stages which are running-in stage, steady-state stage, defect initiation, defect propagation, and damage growth.

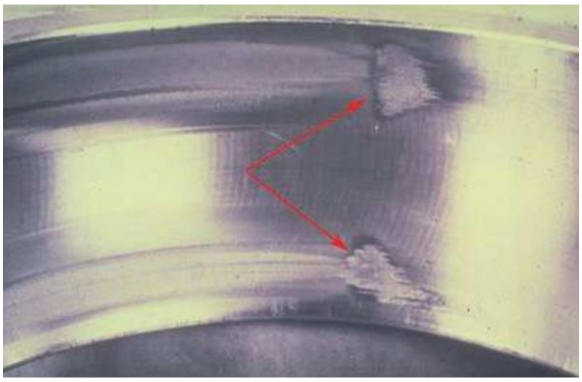

Figure 2.2: Smearing on the outer ring raceways of a spherical roller bearing (International Organization for Standardization, 2017).

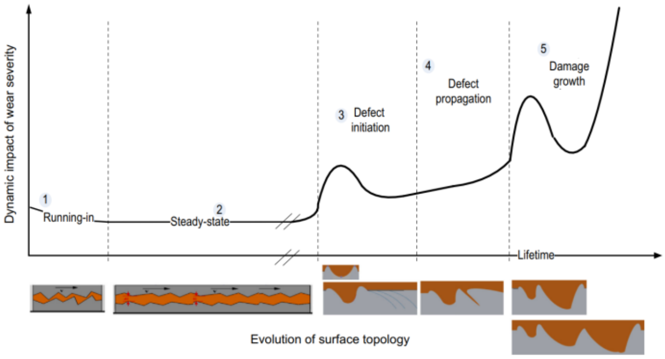

Figure 2.3: Evolution of surface topology in the wear evolution of bearing faults (El-Thalji and Jantunen, 2015).

2.3.3 Corrosion

Corrosion is a failure mode that takes place when bearing components come into contact with moisture, water, or acids. These aggressive media will cause oxidation or corrosion (rusting) and form corrosion pits. For instance, the water content in lubricant or degraded lubricant will react with the bearing elements and result in dark discolouration and corrosion pits. Rust can also develop in bearing via surface oxidation when the ambient humidity is high. Bearing will be at high risk of corrosion when its protective covers is substandard which results in precipitation and condensation under fluctuating temperatures conditions (Malla and Panigrahi, 2019).

On the other hand, frictional corrosion (tribo-oxidation) can be triggered by the relative micromovements between mating surfaces which leads to surface oxidation and material loss in the form of powdery rust. Frictional corrosion can happen via two mechanisms which are fretting corrosion and false brinelling.

Fretting corrosion happens in fit interfaces between components that transmits loads under oscillating micromovements. The surface becomes oxidized into discoloured blackish red. This type of corrosion is typically observed when the radial clamping by mounting fits is exceeded by the applied loads.

False brinelling (vibration corrosion) typically applies to stationary bearings which mostly provide support and stand-by equipments which are occasionally operated. The cause of corrosion are micromovements and the elastic resilience of the contact surfaces under cyclic vibration. Malla and Panigrahi (2019) describes false brinelling as bearing wear due to quick motion of bearing balls in the raceway when machine is idling. As the bearing is lacking rotation, fresh lubricant cannot be replenished to the contact area, which promotes false brinelling. In stationary bearing, depressions are observed at regular intervals where the bearing balls contact the raceways as illustrated in Figure 2.4. The depressions mark may be discoloured reddish or shiny. In stand-by equipment which receives vibrations from adjacent equipments, closely spaced flutes with bright or fretted bottoms will be developed.

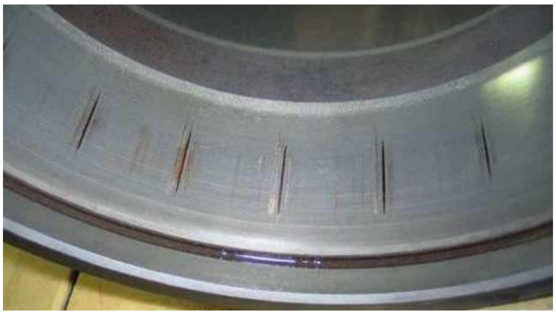

Figure 2.4: False brinelling on outer raceway of a tapered roller bearing (International Organization for Standardization, 2017).

2.3.4 Electrical Erosion

The electrical discharge results in extremely rapid localized heating, which melts and weld the contact areas together. Electrical pitting can manifest as a series of bead-like craters with diameter up to 500 µm as shown in Figure 2.5.

According to Prudhom et al. (2017), bearing currents pose a significant risk of damage to rotating machinery, especially in variable frequency drive (VFD) systems. These currents are present due to common mode voltage, which is the potential difference between the inverter output and earth. In smaller motors rated at less than 30 kW, common mode voltage induces a voltage drop between the inner and outer races of the bearing. Consequently, high frequency bearing current pulses flow through the bearing races. When the voltage difference equals the breakdown voltage of the bearing oil film, the currents will flow through the bearing itself. The currents may damage the contact surface on the bearing balls and races. Eventually, small craters appear on the surface in the form of arcing, pitting, and fluting. As illustrated in Figure 2.6, flutes may develop on the contact surfaces of roller and ring raceway if the damaging current continues to flow continuously. The lubricant that has been deteriorated by electrical current will also exhibit black discolouring and hardened consistency.

Figure 2.5: Craters formed by excessive current on rolling element (International Organization for Standardization, 2017).

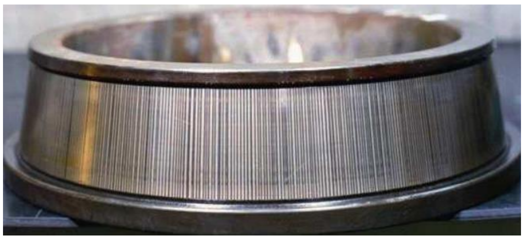

Figure 2.6: Fluting on the inner ring raceway of a tapered roller bearing (International Organization for Standardization, 2017).

2.3.5 Plastic Deformation

In this failure mode, permanent deformation is caused when the yield strength of material is exceeded. Plastic deformation is commonly a result of incorrect assembly methods and presence of foreign matter (Peng et al., 2022). Plastic deformation can occur on a macroscale or microscale, depending on the size of the contact footprint. For stationary bearing, the overloading by static load or shock load is known as true brinelling. Figure 2.7 shows that at the bottom of the depressions caused by overload, surface finish or residual machining marks are visible. Overloading can also be an aftermath of excessive preloading or incorrect handling during mounting. For rotating bearing, instantaneous overload can lead to fluting and depressions while permanent overload triggers the macroscopic deformation of the overloaded raceway circumference. Indentations of various sizes and shapes can also form on raceway as particles are over-rolled. The particles involved may include soft particles (fibres, plastics), hardened steel particles, or hard mineral particles (silica in oil).

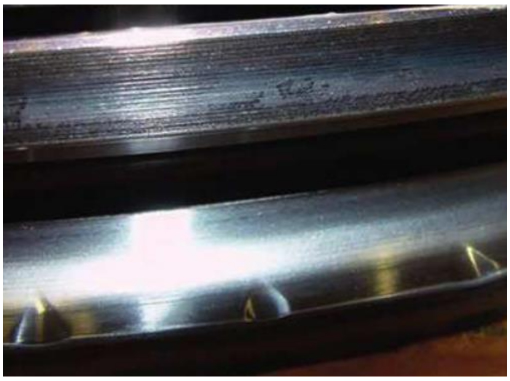

Figure 2.7: Overload on a stationary inner ring of an angular contact ball bearing (International Organization for Standardization, 2017).

2.3.6 Cracking and Fracture

Cracks propagate when the stresses experienced by a material surpass the ultimate tensile strength. This propagation leads to fracture, resulting in a complete separation of the material. Fracture can occur through various modes, including forced fracture, fatigue fracture, and thermal fracture. Forced fracture may be induced by impacts or excessive interference fits, while fatigue fracture arises when the fatigue strength limit is frequently exceeded under bending, tension, or torsion conditions. Lastly, thermal cracking occurs when sliding motion generates significant frictional heating. Components made of hardened steel are particularly susceptible to thermal cracking due to localized rehardening and high levels of residual tensile stress.

2.4 Review on Diagnostic Methods

This subsection discusses the bearing fault diagnostic methods explored in research. The theoretical foundations, practical applications, and experimental results is discussed for each diagnostic method.

2.4.1 Time Domain Techniques

Time domain analysis focuses on analyzing the time-series data directly to identify patterns and trends associated with faults. Typically, statistical measures are used to provide quantitative descriptions of the distribution and central tendency of the vibration signal. Calculations can be performed to attain basic statistical parameters such as peak, peak-to-peak, mean, root mean square (RMS), crest factor, skewness, and kurtosis. Among these parameters, RMS, crest factor, and kurtosis are most commonly used to diagnose the condition of machinery. Skewness is generally known to be a weak indicator of bearing fault as it only measures the asymmetry of the signal.

The assessment of peak value is the most intuitive method to detect any possible faults. When impacts occur due to defect such as spalling, the impulsive force generated by the damaged surface will cause acceleration to increase, resulting in a spike in the signal. Changes in peak amplitude of vibration in the frequency range of 10kHz is a good indicator of incipient damage (Sikora, 2015). However, the simplicity of this method means that it cannot detect subtle changes over time and it can be easily influenced by outlier data points.

2.4.1.1 Root Mean Square

One of the most widely used methods is to observe trend changes in the RMS level as calculated by Equation 2.1. Example of fault indicators include when RMS amplitude exhibit an increasing trend or when RMS increases relative to a healthy baseline. According to Sikora (2015), the RMS method can be refined by subdividing the sampling frequency into different octave or third-octave. As the frequency band becomes narrow, a targeted analysis of RMS level in different range of interest can be performed.

$$RMS = \sqrt{\frac{\sum_{i=1}^{N}(x_i)^2}{N}} \tag{2.1}$$

where
RMS = Root mean square of the signal
N = number of data points
x = amplitude of each data point
i = index of data point

The measurement of RMS is only useful when it is compared against predetermined threshold levels. For this purpose, standard such as ISO 10816-3 and ISO 20816-3 (revised version of ISO 10816-3) provides the threshold for vibration evaluation using the RMS value or peak value of velocity measurement. This standard is applicable for machinery such as electric motors, rotary compressor, turbines, and generators. Vibration measurement is obtained by taking RMS of velocity on non-rotating parts, or by measuring the peak-to-peak displacement on rotating parts. Ideally, the evaluation of the machine should often be performed based on measurements taken on both rotating parts and non-rotating parts. According to Figure 2.8, the determination of machine condition is dependent the machine type (classified by rated power and shaft height) and the flexibility of the machine support. By assessing the vibration against the machine type, the machine condition can be classified into newly commissioned (Zone A), acceptable for long-term operation (Zone B), unsatisfactory for long-term operation (Zone C), and sufficiently severe to cause machine damage (Zone D). (International Organization for Standardization, 2022)

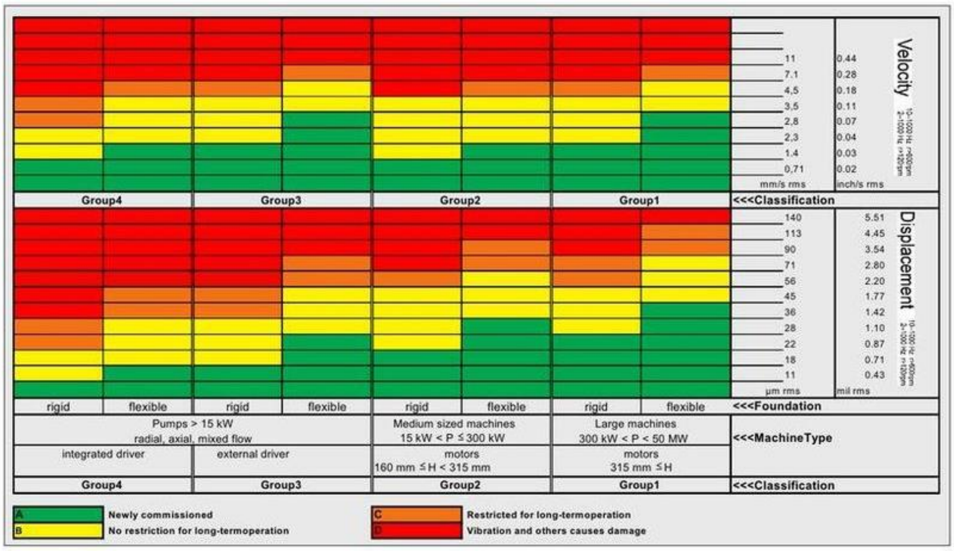

Figure 2.8: Threshold for vibration standard derived from ISO 10816-3 (Ahmadi et al., 2020).

2.4.1.2 K-factor

The K-factor is a parameter defined as the product of RMS and peak vibration in the time domain. It is highly dependent on the rotational speed of the bearing as both RMS and peak values increase with higher speeds. This means that the effect of speed on the K-factor is compounded, which makes it particularly sensitive to changes in operating conditions. K-factor will continue to increase for bearing with severe defects, making it a vibration indicator that is straightforward to interpret (Filippenko, Brown and Neal, 1999). According to Almeida and Almeida (2005), K-factor is effective in detecting changes in defect level in the bearing outer race. The indicator will not be influenced to decrease even as damage becomes more distributed. Moreover, K-factor is sensitive to detecting both small and large defect. This makes it more useful compared to other parameters such as RMS acceleration, peak acceleration, crest factor, and kurtosis. In short, K-factor has potential to be a sensitive vibration indicator for identifying both small and large defects, which contributes to the early detection of bearing failure.

2.4.1.3 Crest Factor

Crest factor is the ratio of the peak amplitude to the RMS amplitude of the signal. It is representative of the impulsiveness and spikiness of the vibration signal. A high crest factor means the bearing is experiencing increased impact during operation. As illustrated in Figure 2.9, localized defect creates transient bursts of high energy in the vibration signal which increase the peak value but has no effect on the RMS value, resulting in increased crest factor.

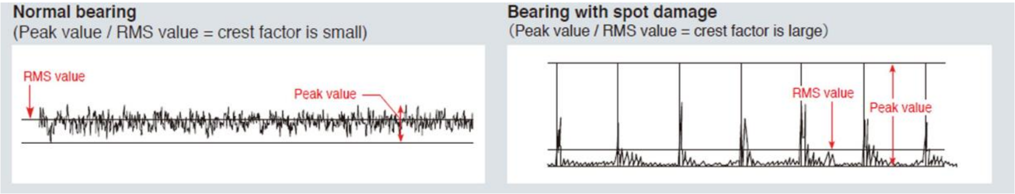

Figure 2.9: Comparison of crest factor between healthy and faulty bearing (Kondhalkar and Diwakar, 2019).

To establish a threshold level, Pachaud, Salvetat and Fray (1997) found that the crest factor value of a Gaussian signal falls between 3 and 5 while Dron, Bolaers and Rasolofondraibe (2004) reported a range between 3 and 6. On the other hand, Patidar and Soni (2013) indicates the value of the crest factor for a healthy bearing is approximately five. All in all, the value of crest factor for bearing without fault should be less than 5.

Crest factor is advantageous in actual operating conditions due to its simplicity and insensitivity to changes in bearing load and speed (Dyer and Stewart, 1978; Sikora, 2015). However, this method also comes with several drawbacks. First, the effectiveness of crest factor is dependent on the presence of significant impulsiveness (Aherwar and Khalid, 2012). For example, in the early stages of a bearing defect, the fault vibration is normally low compared with other vibration sources, thus making the detection difficult. At advanced stages where bearing damage is severe, crest factor will counterintuitively decrease because RMS of the vibration is very significant (Patidar and Soni, 2013).

2.4.1.4 Kurtosis

Kurtosis is the normalized fourth statistical moment of the signal given by Equation 2.2. It is a measure of the tailedness of a signal relative to the normal distribution (Aherwar and Khalid, 2012). Similar to crest factor, kurtosis is also proportional to the spikiness of the vibration signal. A bearing in good condition exhibits a Gaussian distribution of accelerations, characterized by the kurtosis value of 3. Kurtosis value greater than 3 indicates that the distribution is sharply peaked with heavy tails (Lord, Qin and Geedipally, 2021). According to Figure 2.10, these features indicate that extreme values occur more frequently in the data. When kurtosis value is greater than 3, it indicates failure without the need for prior vibration history. The indication of damage first occurs in the lower frequency bands of around 3 to 5 kHz (Mathew and Alfredson, 1984). On the other hand, Kim (2013) suggested the use of kurtosis value greater than 7 as reference value for detecting substantial non-normality in large sample data (n > 300). Kurtosis is found to be particularly effective in the detection of incipient faults in narrow bands at high frequencies. Kurtosis value is sensitive to rotational speed because the time interval between the occurrence of successive fault events reduces at high rotational speed. Hence, vibration signal becomes more impulsive and transient, thereby increasing the kurtosis (El-Thalji and Jantunen, 2015). In order for kurtosis to be effective, the frequency of shock repetition must be between 2.5 and 3 times of the shock relaxation time (Dron, Bolaers and Rasolofondraibe, 2004).

$$k = \sum_{n=1}^{N} \frac{[x(n)-\mu]^4}{N(\sigma^2)^2} \tag{2.2}$$

where

$x(n)$ = amplitude of time series

μ = mean value

N = total number of data points

σ = variance

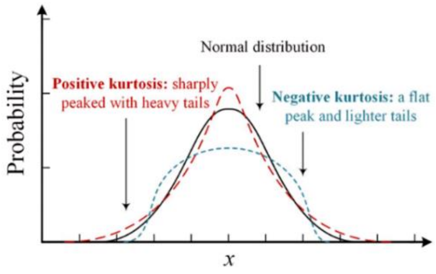

Figure 2.10: Comparison between different values of kurtosis (Xie et al., 2022).

2.4.2 Frequency Domain Analysis

Frequency-domain analysis is a signal processing technique which involves the transformation of time-domain signal into its frequency components. This decomposition of time waveform is commonly performed using Fast Fourier Transform (FFT). The result of the transform, referred to as spectrum, describes the magnitude and phase characteristics of a signal as a function of frequency.

2.4.2.1 Spectrum Analysis

In spectrum analysis, the main frequencies of interest are the four characteristics fault frequencies of bearing which are cage fault frequency, outer raceway fault frequency, inner raceway fault frequency, and rolling element fault frequency. The frequencies can be determined using Equation 2.3 to Equation 2.6. Cage fault frequency or FTF (fundamental train frequency) is the frequency generated by defective bearing cage. Outer raceway fault frequency or BPFO (ball pass frequency outer) is defined as the fundamental vibration frequency when the ball passes over the defect on the bearing outer race. Rolling element fault frequency is the pulse repetition rate due to the interaction between defective rolling element and adjacent surfaces. This fault frequency is twice the value of ball spin frequency (BSF), which is the angular frequency of the spinning rolling element (Malla and Panigrahi, 2019; Prudhom et al., 2017; Patidar and Soni, 2013). On the other hand, distributed faults produce more complicated vibration patterns. The response of distributed faults is characterized by two dominant impulse responses at the entry and exit of the faulty area, and a series of minor vibrations caused by the roughness in the faulty area (Dolenc, Boškoski and Juričić, 2016).

$$F_{cage} = \frac{1}{2}\left[1 - \frac{D_B}{D_P} cos\,\beta\right] F_R \tag{2.3}$$

$$F_{inner} = \frac{N_B}{2}\left[1 + \frac{D_B}{D_P} cos\,\beta\right] F_R \tag{2.4}$$

$$F_{outer} = \frac{N_B}{2}\left[1 - \frac{D_B}{D_P} cos\,\beta\right] F_R \tag{2.5}$$

$$F_{ball} = \frac{D_P}{D_B}\left[1 - \left(\frac{D_B}{D_P}\cos\beta\right)^2\right] F_R \tag{2.6}$$

where

N_B = Number of rolling elements

D_B = Ball or roller diameter

D_P = Pitch diameter

β = Contact angle

F_R = Shaft speed (Hz)

However, the characteristics fault frequencies are just a theoretical value as discrepancies arise especially when bearings carry significant thrust loads or when slippage exists (McInerny and Dai, 2003). The slip experienced by rolling elements can cause a constant or random deviations in kinematics frequency. Moreover, when the defect is experiencing variation in load distribution, the impacts will be modulated in amplitude. Due to load modulation, sideband effects are pronounced when the fault is located on rotating parts. This means spectral components are expected to appear around the main spectral lines (Renaudin et al., 2010).

The vibrations signal of bearing is dominated by high-level imbalance and misalignment components while also contains friction-induced random vibrations. Imbalance vibration occurs at the frequency of shaft revolution (known as the 1X), while misalignment appears at the fundamental (1X) and its harmonics. The spectral components associated with the ringing pulse sequence (bearing defects) are not integer harmonics of the fundamental, making them distinct compared to other vibrations. However, these components can easily be lost in the background vibration noise since their amplitude is relatively small. Hence, conventional spectral analysis has its limitations especially when the background vibration is large enough to bury the components of ringing pulse sequence (McInerny and Dai, 2003).

2.4.2.2 Cepstrum

Cepstrum is defined as the inverse Fourier transform of the log spectrum. It is obtained by applying FFT to the time-domain signal, subsequently determining its natural logarithm of magnitude, and lastly performing inverse FFT. According to (Randall and Sawalhi, 2011) it has been long established that editing in the cepstrum will lead to the removal of harmonics and sidebands from the spectrum. A new method is further proposed to achieve the separation of periodic components (bearing signal) from random components (gear signals) in a signal. The periodic primary signal is measured on a faulty bearing while the random reference signal is measured on a remote healthy bearing. The separation of these two components leads to the de-noising of bearing vibration data.

Based on Figure 2.11, after the real cepstrum is obtained, the rahmonics (uniformly spaced components in the cepstrum) associated with the harmonics and sidebands families are removed. The edited cepstrum then goes through FFT and combines with the original phase spectrum. This results in the creation of complex log spectrum which is then passed through IFFT to obtain the time signal. The time signal will no longer contain random vibrations induced by gear mesh, which increases the clarity in fault detection. All in all, cepstrum is a useful technique in de-noising and filtering applications in vibration analysis.

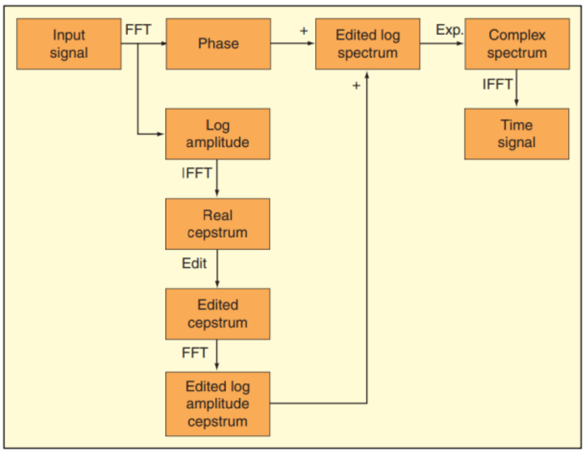

Figure 2.11: Schematic diagram of the cepstral method for the removal of harmonics and sidebands (Randall and Sawalhi, 2011).

2.4.3 Time-Frequency Analysis

Time-frequency analysis is a signal processing technique utilized to analyse non-stationary signals which have varying frequency content over time. Qualitatively, time-frequency transforms can be divided into discrete and continuous. According to Prudhom et al. (2017), time-frequency analysis is advantageous as the preservation of time information means it has the ability to visualize the progressive degradation of the bearing while discriminating against unrelated frequencies. Time-frequency map is capable of illustrating the amplitude evolution of fault-related frequencies in a single plot. Characteristic t-f patterns then can be observed to diagnose bearing faults. This method is said to be highly reliable and rarely yields false positives. However, the technique has a drawback whereby transient component in the TF plane has wider spread compared to the original time domain. Hence, this results in reduced accuracy in time locating for transient events.

2.4.3.1 Short-Time Fourier Transform

In Short-Time Fourier Transform (STFT), the concept of local frequency is utilized by applying the Fourier transform to the signal using a sliding window shown in Figure 2.12. This effectively treats the signal as stationary within each window (Boudinar et al., 2019). The frequency composition in each time fragment can be evaluated and the result will be represented as a two-dimensional time-frequency map. As shown in Equation 2.7, STFT is performed by multiplying the input signal with a window function, subsequently applying Fourier transform on the product. However, the major drawback of STFT is the inability to achieve good resolutions in time and frequency domains simultaneously due to the Heisenberg uncertainty principle (Lee, 2013).

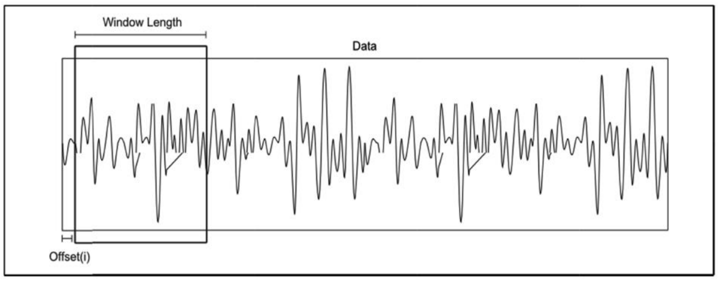

Figure 2.12: Sliding window concept in STFT (Boudinar et al., 2019).

$$\text{STFT}\,\{x(t)\}(\tau,\omega) \equiv X(\tau,\omega) = \int_{-\infty}^{\infty} x(t)\, w(t-\tau) e^{-i\omega t} dt \quad (2.7)$$

where

$X(\tau,\omega)$ = Fourier transform of $x(t)(t - \tau)$

$x(t)$ = Signal to be transformed

$w\,(t-\tau)$ = Sliding window function

τ = Window function centered to zero

ω = Frequency

In adaptive STFT, the window length changes dynamically in response with the variations in vibrations. The length of the local window is affected by change in the local instantaneous frequency (IF). This means if the variation of the IF happens rapidly, a short window length will be applied. This method yields a clearer resolution in both time and frequency when compared to standard STFT. The diagnostic capability of this technique is illustrated in Figure 2.13. There are five prominent peaks appearing within a 0.1-second period, which suggests that chattering is occurring every 0.02 seconds (Lee, 2013).

It is also possible to performing windowing in the frequency domain as demonstrated by Mateo and Talavera (2018). The window size is defined as a fixed number of cycles of each frequency. This approach does not need band-pass filter banks which is required in multi-resolution STFT to capture signal components at multiple scales. Moreover, there will be no evaluation of local signal characteristics such as instantaneous frequency or amplitude variations, unlike in adaptive STFT. This technique can deliver good resolution in time and frequency domain simultaneously; however, it requires significant computation time.

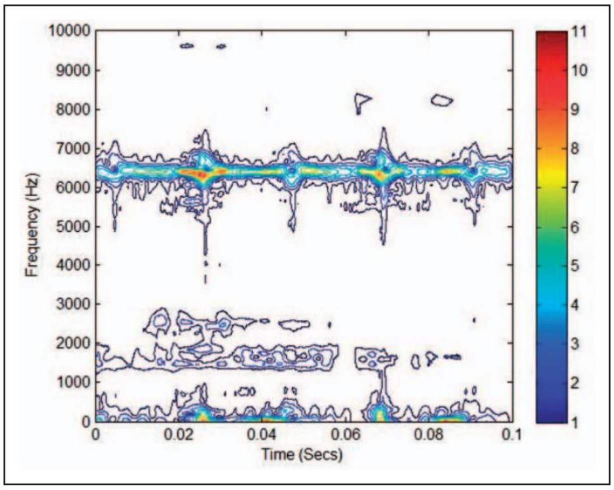

Figure 2.13: Time-frequency contour plots using adaptive STFT scheme (Lee, 2013).

2.4.3.2 Spectral Kurtosis

Spectral kurtosis (SK) is a statistical parameter indicating how the impulsiveness of a signal varies with frequency. Typically, SK is applied as a band-pass filter to retain the impulsive components while significantly reducing the background noise. This is because SK is effective in identifying the frequency bands dominated by the bearing fault signals, which usually included fault-excited resonance frequencies. At frequencies where the signals are predominantly stationary, the SK is effectively zero. The determination of these optimum frequency bands along with the center frequency is crucial for the accuracy of envelope analysis technique.

According to Figure 2.14, the spectra obtained from each time window are arranged in a three-dimensional diagram with a time axis and a frequency axis. This makes the intensity of each frequency component to be observable over a period of time. Subsequently, SK is calculated for each frequency line in the time direction (Randall and Sawalhi, 2011). Peaks in the spectral kurtosis spectrum means impulsive activity is significant in the particular frequency bands, which is an indication of bearing abnormality. However, SK can be easily influenced by background noise. Hence, proper preprocessing methods such as denoising and filtering on the raw signal is important to increase the reliability of SK (Xiang, Zhong and Gao, 2015).

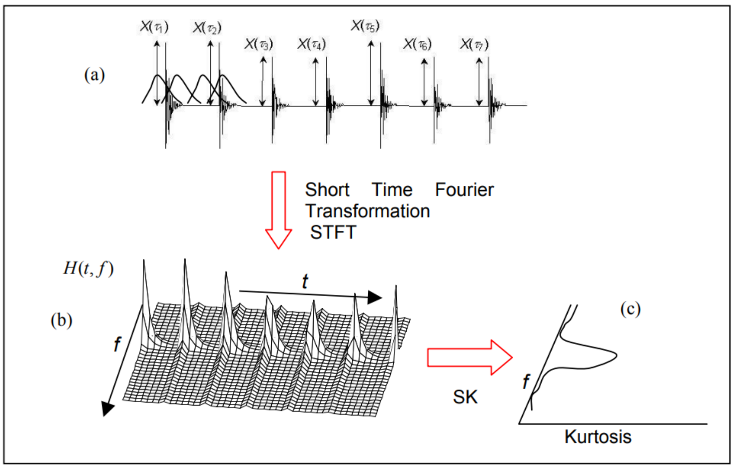

Figure 2.14: Calculation of SK for a simulated bearing fault signal (Sawalhi and Randall, 2011).

2.4.3.3 Wavelet Analysis

Wavelet transform is a technique for the simultaneous analysis in both domains using the concept of wavelets. Wavelet analysis is useful in providing a signal representation with multi-resolution in time and frequency, which facilitates fault detection. Wavelet tools are powerful due to its ability to zoom in on any time intervals without sacrificing spectral information (Al-Badour, Sunar and Cheded, 2011). In order to focus on the low frequency components, longer time interval is applied, and vice versa.

Tse, Peng and Yam (2001) defines wavelet analysis as a scale-time decomposition of a temporal signal, x(t), into components $\psi\left(\frac{t-b}{a}\right)$ which are localized in time. The transformation of basis wavelet and the wavelet transform of input signal is computed using Equation 2.8 and Equation 2.9 respectively. Wavelet analysis is initiated by the selection of mother wavelet (basis wavelet), which is a waveform with average value of zero, and is only effective in a limited duration. The selection of basis wavelets is crucial as it significantly affect the analysis outcome. Examples of basis wavelets include Haar wavelet, Daubechies wavelets, Morlet wavelet, Mexican hat wavelet, and Gaussian wavelet as partially shown in Figure 2.15. Morlet and Gaussian wavelets to be the best at representing vibration signal as they consist of harmonic oscillation with singularity (Al-Badour, Sunar and Cheded, 2011). This effectively imitates the background noise and the bearing fault.

Using the basis wavelet, operations such as stretching and shifting is performed on the basis wavelet to generate wavelets family for analysis. The scaling parameter will apply stretching or compression on the basis wavelet, while the time shifting parameter moves the wavelet along the time axis. The result of wavelet transform will be obtained by determining the product of the complex conjugate of the modified wavelet and the input signal.

$$\psi_{a,b}(t) = \frac{1}{\sqrt{a}}\psi\left(\frac{t-b}{a}\right) \tag{2.8}$$

where

$\psi\left(\frac{t-b}{a}\right)$ = scaled and shifted version of basis wavelet

a = scaling parameter

b = time shifting parameter

$$W_x(a,b) = \int_{-\infty}^{+\infty} x(t)\, \psi_{a,b}^{*}(t)\, dt \tag{2.9}$$

where

W_x = Wavelet transform of the signal

$x(t)$ = Input signal

$\psi_{a,b}^{*}(t)$ = Complex conjugate of the modified wavelet

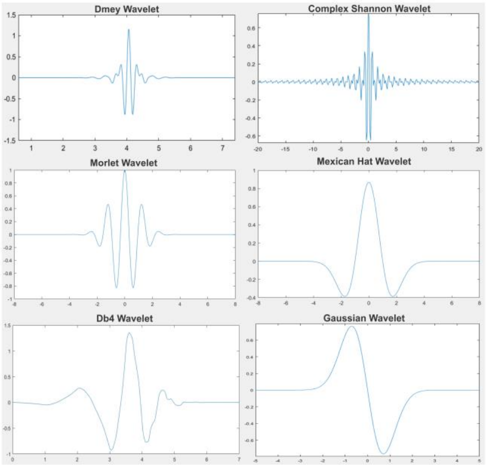

Figure 2.15: Examples of different types of mother wavelets (Salles et al., 2020).

The diagnosis capability of wavelet analysis is demonstrated by Tse, Peng and Yam (2001). Healthy bearing is found to have low energy level in the low frequency range under 2 kHz, where the majority of the macrostructural vibrations are located. For a bearing with race fault, the presence of dark coloured contours indicates that the energy levels in the low frequency range is high, with an increase of up to 20 dB. The time interval between impact occurrence can be measured based on difference between dark coloured strips. In Figure 2.16, the interval is estimated to be 4.5 ms, which validates the theoretical outer race fault frequency of 222 Hz.

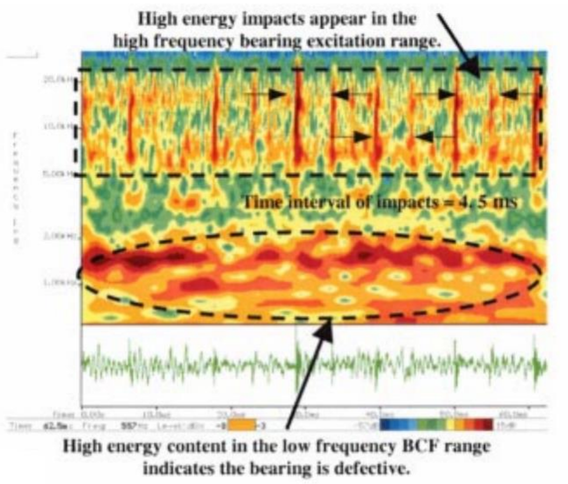

Figure 2.16: Time-frequency map of outer-race defect using wavelet analysis (Tse, Peng and Yam, 2001).

2.4.4 Envelope Analysis

Envelope analysis involves the extraction of envelope of a modulated signal to highlight its low-frequency variation. The envelope is the curve that tracks the maximum amplitude of a signal, which represents the smoothed version of the vibration signal When a localized defect is created on the bearing, it generates a characteristic fault frequency, which causes amplitude modulation on the resonance frequency of the bearing housing (Feng et al., 2015). Amplitude modulation here refers to the multiplication of the high-frequency resonance signal by a low-frequency fault frequency signal. When a signal is modulated, its spectrum will have a peak at the carrier frequency, while having sidebands spaced at intervals determined by modulation frequency. The modulating frequency is important to be determined as it corresponds to the fault frequency. However, it is practically impossible to resolve the sidebands from the conventional spectrum due to the limited spectral resolution. Hence, techniques such as bandpass and demodulation is utilized. Generally, the procedure of envelope analysis consists of bandpass filtering, rectification, and lastly Fourier transform (McInerny and Dai, 2003).

Bandpass filtering is used to allow signals within the passband while attenuating signal outside of the range. The passband is established to remove random noise and attenuate signal components related to imbalance and misalignment, which are typically low-frequency and high amplitude

(McInerny and Dai, 2003). The centre frequency of the passband should be selected to coincide with the resonance frequency of the structure. Next, the bandwidth should be a minimum of two times the highest bearing characteristic defect frequency. The technique of spectral kurtosis can also be applied to select the appropriate centre frequency and bandwidth (Patel, Tandon and Pandey, 2012).

In rectification, the bipolar filtered signal is converted into a unipolar signal. This rectification is often performed using Hilbert transform (HT), which mathematically shifts the phase of the input signal by 90°. To achieve Hilbert transform, the input signal (x_{in}) is first passed through the FFT to produce X_{in}. X_a is calculated using Equation 2.10 before it is processed via IFFT to obtain the analytic signal (x_a). The analytic signal is a complex signal where the real part represents the original signal and the imaginary part is the Hilbert transform of that signal (Feng et al., 2015).

Since, the product of a complex conjugate pair is positive and real, Equation 2.11 essentially computes the square of complex magnitude and subsequently takes its square root to obtain the envelope signal. After removing the envelope mean value from the envelope signal, FFT is applied to obtain the envelope spectrum as shown in Equation 2.12. Hanning window functions are included to reduce the spectral leakage.

$$X_a(n) = \begin{cases} X_{in}(n), if\ n = 0, N/2 \\ 2[X_{in}(n)], if\ 0 < n < N/2 \\ 0,\ if\ N/2 < n < N \end{cases} \tag{2.10}$$

where

X_a = FFT of analytic signal, x_a

X_{in} = FFT of input signal, x_{in}

n = Index of data sequence with the length of N

$$x_{env} = \sqrt{(x_a) * conj(x_a)} \tag{2.11}$$

$$X_{env} = |\ \mathrm{FFT}(x_{env} - \overline{x_{env}}) * hann(N)\ | \tag{2.12}$$

where

X_{env} = Envelope spectrum

$\overline{x_{env}}$ = mean value of the envelope

$hann(N)$ = Hanning window

The square of the absolute value of envelope spectrum, or squared envelope spectrum (SES) is utilized with computed order tracking (COT) to minimize the impact of speed fluctuations. Computed order tracking is a method which is based on multiples of the rotational speed called orders, instead of absolute frequencies. The vibration data is first sampled at constant rate and resampled to constant angular increments using the computed order tracking software. The analysis of angular-resampled signal is more invariant towards speed variations (Borghesani et al., 2013).

The analysis result of envelope spectrum are presented by Feng et al. (2015), which carried out vibration monitoring using wireless sensor network. As depicted in Figure 2.17 (b), the spectral components outside of the passband is attenuated which provides focus on the bearing defect frequencies. As anticipated, the envelope signal shown in Figure 2.18 (a) closely matches with the filtered signal in Figure 2.17 (a). From Figure 2.18 (b), three distinct peaks are observed in the low frequency region while components above 500 Hz are suppressed. The peaks registered frequencies of 87.9 Hz, 170.9 Hz and 258.8 Hz respectively, which match the first three harmonics of outer race fault frequency shown in Figure 2.19. Moreover, when the results of envelope spectrum from four different nodes are averaged, the spectral peaks become more pronounced, which leads to a reliable diagnostic result.

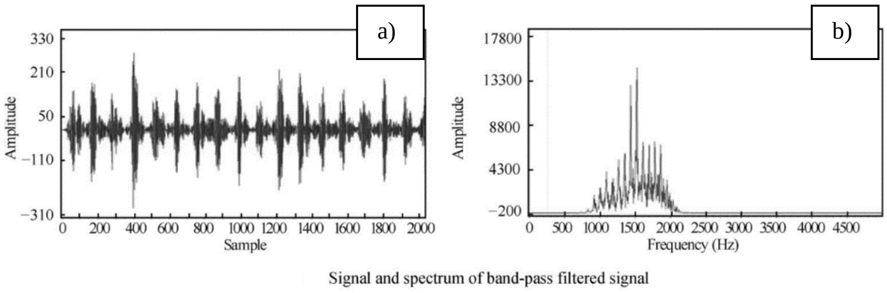

Figure 2.17: Band-pass filtered signal: (a) Signal waveform; (b) frequency spectrum (Feng et al., 2015).

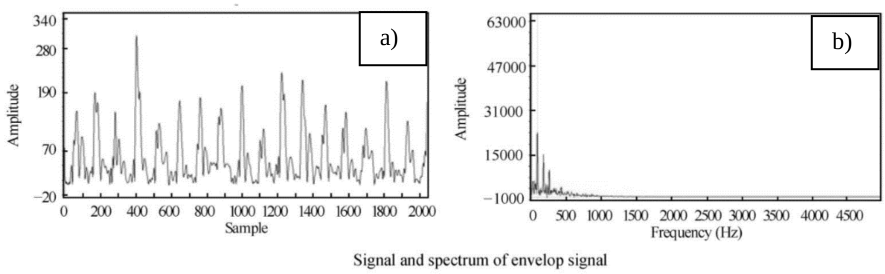

Signal and spectrum of envelop signal

Figure 2.18: Envelope signal: (a) Signal waveform; (b) frequency spectrum (Feng et al., 2015).

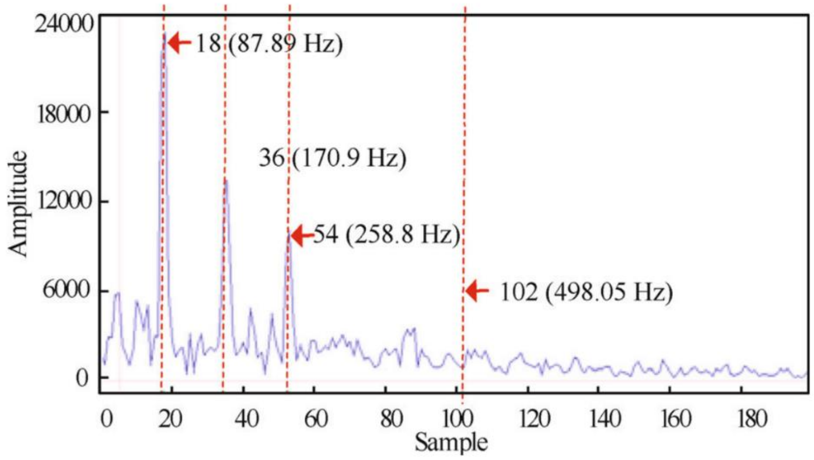

Figure 2.19: Envelope spectrum magnified in low frequency range for the faulty roller bearing (Feng et al., 2015).

2.4.5 Statistical Process Control

Statistical process control (SPC) is the application of statistical methods to monitor process and analyse trend, commonly in manufacturing settings. In bearing fault detection, SPC can be employed to detect any abnormal variations or trends in the vibration data, which serves as indication for potential degradation. In SPC, a core concept called Shewhart theory states that all processes exhibit variation, which is either caused by common cause or special cause. When a process is statistically controlled, it is operating in a steady state without presence of special cause variation. Control charts such as mean chart and range chart are used to monitor the process data by comparing it to the predetermined control limits. The signal is considered out of control if there is data point located beyond the limits, if there is a series of rising or falling trend, or if there is a run above or below the mean value (Oakland, 2007, pp.105–112).

In the practical application of SPC, historical data is crucial for the understanding of the monitored process and effectiveness of the method. Wang and Zhang (2008) demonstrated that the failure evolution of bearing is a two-stage process. Conventional SPC theory can be used to determine the initiation point of the defect. For the determination of initiation point, data from normal operation is used to establish the mean and the control limits. The vibration level, where all test bearings behaves similarly, is selected to be the threshold level. Variations from the control limits shown by Equation 2.13 and 2.14 indicates that the defect has been initiated. As shown in Figure 2.20, the bearing vibration starts to surpass the action line at around 900 hours of operation, indicating fault formation.

$$\text{Action limit} = \mu + 3\sigma \tag{2.13}$$

$$\text{Warning limit} = \mu + 2\sigma \tag{2.14}$$

where

μ = mean value

σ = standard deviation

Saidy et al. (2020) demonstrated the use of cumulative sum (CUSUM) control chart to improve detection on small process shifts. First, the target mean of μ_0 is determined using data from in-control process to serve as the baseline. If a process is operating within control at μ_0, the cumulative sum will be a random walk (sequence) with a mean of zero. However, when the mean become greater than μ_0, the cumulative sum will increase, indicating a upward shift in the overall process mean. Figure 2.21 shows the application of the CUSUM chart in the bearing monitoring of aircraft gearbox. The gray points indicate data points within control while points in red represents possible fault modes.

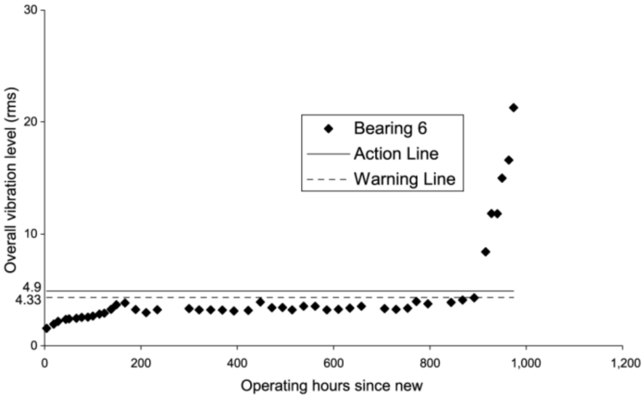

Figure 2.20: Shewhart mean chart for bearing monitoring method (Wang and Zhang, 2008).

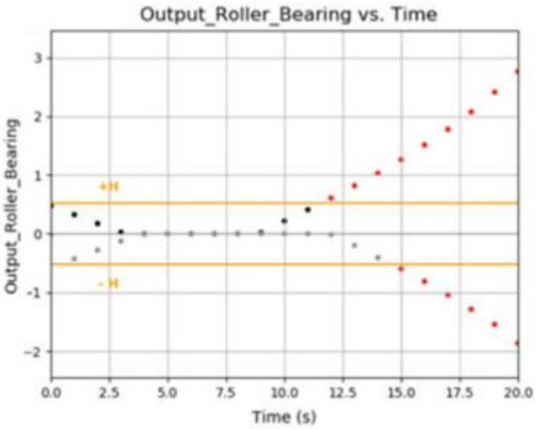

Figure 2.21: Fault detection on roller bearing in an aircraft gearbox (Saidy et al., 2020).

2.5 Review on Prognostics Methods

This subsection examines several prognostic methods used for the estimation of remaining useful life. Example of prediction methods include support vector machine and recursive least square.

2.5.1 Prognosis in Predictive Maintenance

Predictive maintenance is a maintenance strategy that uses data analytics to predict the failure point of equipment, which allows the component to undergo maintenance before it critically fails. The prediction of machine condition leads to prolonged usage of the machinery and reduced down time. When effective prognostic methods are in place, sufficient lead time is available to acquire replacement parts and schedule maintenance work.

Prognosis refers to the ability to predict the future health and degradation of the machinery based on existing data. Typically, prognosis focuses on estimating the remaining useful life and the progress of deterioration. Remaining useful life (RUL) is defined as length from current condition to the end of use of an asset (Liu et al., 2018). The accurate prediction of RUL is crucial for optimizing the operational lifespan of equipment.

There are two types of methods in prognosis, namely physics model-based and data-driven (statistical and machine learning) (El-Thalji and Jantunen, 2015; Kim et al., 2012). In this study, the focus will only be on the data-driven methods. The data-driven approaches are based on the past historical data obtained from the monitoring system. The main assumption taken is that the statistical characteristics of the dataset is relatively constant, unless if abnormality happens to the system. For the prediction to be effective, the degradation model, assessment of the current state (diagnostic) and knowledge of failure pattern needed to be optimized. After feature extraction (feature selection), the dataset are trained using classification algorithms. The estimation of health states is performed using classification algorithms such as Support Vector Machines, Linear Regression, and Artificial Neural Networks (Kim et al., 2012). However, due to the complexity of neural networks, they fall outside the scope of this study and will not be discussed.

2.5.2 Support Vector Machines

Support Vector Machines (SVM) is a supervised machine learning algorithm which predicts the target value (class labels) of the data points when provided with the attributes (features) (Hsu, Chang and Lin, 2016). The training vectors (input-output pairs) are mapped into higher dimensional space. As shown in Figure 2.22, SVM model determines a linear separating hyperplane which maximizes the margin between different classes. The larger the margin between the hyperplane and the nearest vector from each class, the better the performance of the model against new data.

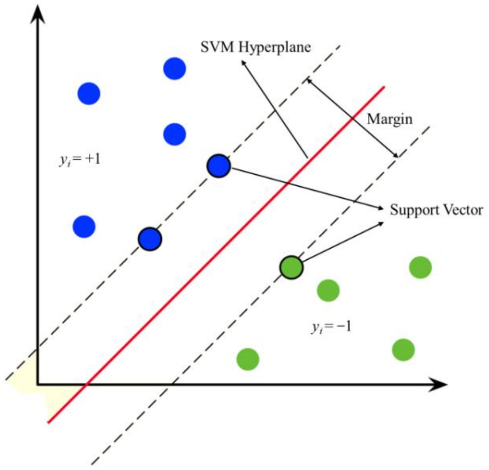

Figure 2.22: The separation of two classes performed by SVM (Yang and Prayogo, 2022).

Kim et al. (2012) demonstrated the usage of SVM for multi-classification of health stages using the ‘‘one-against-one’’ method. First, diagnostic is performed to obtain relevant time domain parameters and frequency domain parameters as shown in Table 2.1. These parameters serve as features for the classification of health states with SVM. In Figure 2.23, the bearing degradation is assumed to follow a series of discrete health states, taking into account the nonlinear nature of failure and the presence of dynamic processes. The probability distribution of each health state with respect to time also naturally overlaps. After finding the probability of each health states from multi-classification, the prediction of RUL is performed using Equation 2.15. The prediction model is affected by the health state probabilities at a particular time, and the historical remaining life of each health state.

$$\mathrm{RUL}(T_t) = \sum_{i=1}^{m} \Pr(S_t = i|\overrightarrow{x_t}, \dots, \vec{x}_{t+u-1}) \cdot \tau_i \qquad (2.15)$$

where

T_t = specific point in time

$\Sigma\, Pr$ = sum of probabilities

$\overrightarrow{x_t}$ = observed features at time (t)

S_t = probabilities of each health state at time (t)

τ_i = historical remaining life for each trained health state (i)

m = number of health state

From Figure 2.24, the probability of first state is observed to begin at 100% and decreases gradually. When the first state probability is declining, the second state probability will increase at the same rate. The overlaps between the health states and the non-uniformity of the distribution is due to dynamic processes, uncertainty in machine health, and possible inappropriate acquisition of data. As illustrated in Figure 2.25, the overall trend of the predicted RUL matches the gradient of the actual RUL. The average prediction accuracy was also high, standing at 94.4% across the whole dataset.

Table 2.1: Selection of feature parameters and its attributed feature number in square bracket (Kim et al., 2012).

Position	Time domain parameters	Frequency domain parameters
Acc. (A)	Mean [1], RMS [2], Shape factor [3], Skewness [4], Kurtosis [5], Crest factor [6]	RMS frequency value [11], Frequency centre value [12]
Acc. (B)	Entropy estimation value [7], Entropy estimation error [8], Histogram upper [9] and Histogram lower [10]	Root variance frequency [13] and Peak value [14]

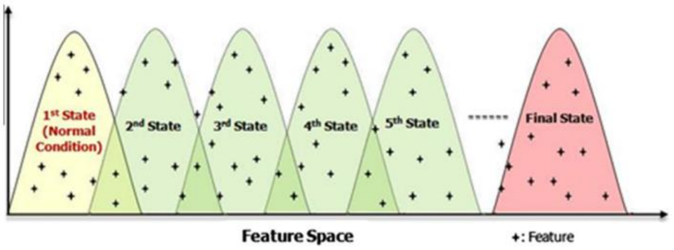

Figure 2.23: Discrete health states in the machine degradation (Kim et al., 2012).

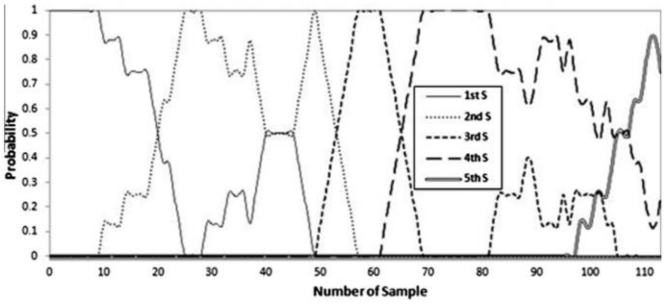

Figure 2.24: Probability distribution of each health state obtained from open test (Kim et al., 2012).

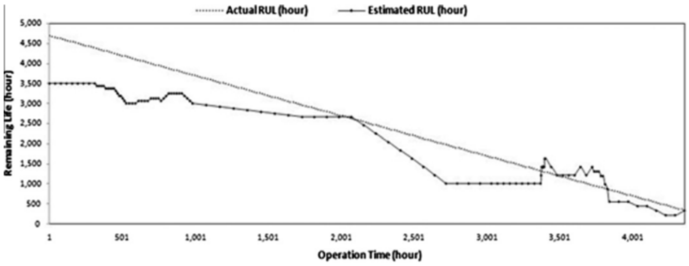

Figure 2.25: Comparison between actual RUL and predicted RUL for open test (Kim et al., 2012).

2.5.3 Recursive Least Square

Recursive Least Squares (RLS) is a technique used to estimate the parameters of a linear regression model recursively over time as data is sequentially available. Rocchi et al. (2014) demonstrated a prognosis algorithm based on the prediction of the deterioration with vibration acceleration as input. The system is modeled so that the trend of deterioration follows an exponential pattern as shown in Equation 2.16. The model parameters are important in representing the characteristics of the system. Hence, they will be determined and updated using a Recursive Least Square algorithm with a Forgetting Factor (RLSFF) as shown in Equation 2.17. Forgetting Factor allows the algorithm to assign less weight to older data points while providing more importance to new data entries. RLS updates the model parameters based on the error between predicted and actual acceleration signals, assuming that wear is proportional to vibration. Finally, the prediction of acceleration signal is computed based on the actual measured signal and the model parameters as shown in Equation 2.18. The algorithm can successfully predict the eventual rise of the acceleration signal for actual faults. In Figure 2.26, the red line represents the threshold value. As the predicted signal exceeds the threshold value, it indicates that the equipment will experience failure in the near future.

$$y(t_k) = w_1 \cdot e^{w_2 \cdot t_k} \qquad (2.16)$$

where

$y(t_k)$ = predicted acceleration at time t_k

t_k = time instances between consecutive samples in data

w_1 = model parameters representing scale factor

w_2 = model parameters representing decay rate

$$\boldsymbol{w}(t_{k+1}) = \boldsymbol{w}(t_k) + \boldsymbol{K}(t_k) \cdot e(t_k) \qquad (2.17)$$

where

$\boldsymbol{w}(t_k)$ = parameters vector

$\boldsymbol{K}(t_k)$ = gain vector

$e(t_k)$ = error signal

$$y(t_{k+i}) = d(t_k) + w_1(t_k) \cdot e^{w_2(t_k)(t_{k+i})} - y(t_k) \qquad (2.18)$$

where

$y(t_{k+i})$ = predicted acceleration at time t_{k+i}

$d(t_k)$ = actual measured acceleration signal at time t_k

$y(t_k)$ = predicted acceleration at time t_k

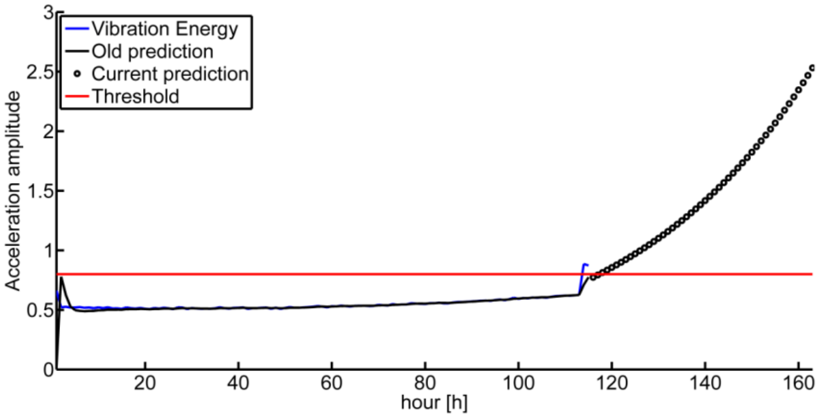

Figure 2.26: Prediction of vibration acceleration signal in an event of actual fault (Rocchi et al, 2014).

2.6 Summary

In summary, a comprehensive review of literature has been conducted for the understanding of bearing fault detection. First, the defect types and failure modes of bearing have been explored to provide an insight on the underlying mechanisms. Next, the signal processing techniques used to diagnose bearing faults are discussed in detail. The diagnostic of fault can be performed in either time domain, frequency domain, or time-frequency domain. Lastly, the review covers the prediction of RUL through the use of SVM and RLS.

A significant research gap in the current study is the absence of standardized thresholds for key vibration indicators such as the k-factor, crest factor, and kurtosis. Additionally, the research lacks a comprehensive analysis of the vibration indicators that offer the highest effectiveness, which limits the detection of bearing failures. There is also a notable lack of comparison with commercial vibration monitoring systems, which makes the practical performance of the proposed monitoring methods unclear. Lastly, some of the techniques explored may be too computationally intensive for real-time monitoring and predictive maintenance applications in industrial settings.

CHAPTER 3

METHODOLOGY AND WORK PLAN

3.1 Introduction

This chapter outlines the overall work plan for the study and provides a detailed explanation of the methodology used in setting up the experiment. The process of preparing defective bearings will be stated in detail. Following this, the procedures for setting up the experimental test rig and collecting data will be outlined. Finally, the development of the vibration monitoring algorithm will be explored.

3.2 Work Plan

Figure 3.1 illustrates the work plan followed in this study, which was employed to develop an effective vibration monitoring algorithm and prepare defective bearings for experimental use. The algorithm was then evaluated through experiments to test its effectiveness and reliability.

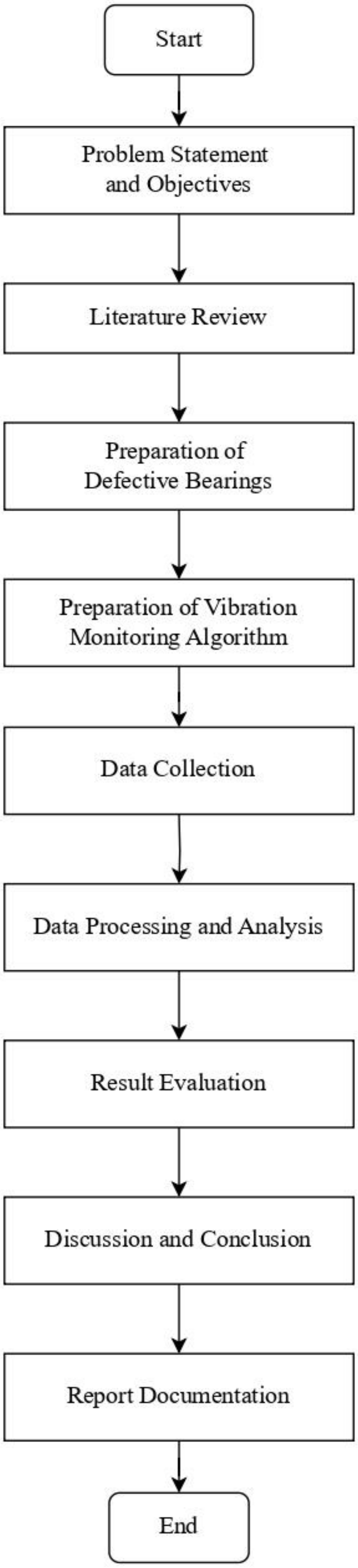

Figure 3.1: Flowchart of work plan.

3.3 Experimental Setup

3.3.1 Component Specification

The main components used in this setup are a data acquisition system, accelerometer, AC motor, variable frequency drive, and ball bearings. The technical specifications of these components are summarized in Table 3.1.

The NI-9234 data acquisition system, as shown in Figure 3.2, was selected due to its high sampling rate. This data acquisition system (DAQ) has the capability to obtain 51200 samples per second which is equivalent to 51.2 kHz when utilizing only one channel. Since it has a total of 4 channels, it is capable to support inputs from multiple accelerometers if required. With a resolution of 24 bits, the digital signal can be represented with a high accuracy (National Instruments, 2024).

In Figure 3.3, Kistler 8704B50T accelerometer was selected to measure acceleration experienced by the bearing as representation of vibration. This piezoelectric accelerometer has a wide measuring range which is suitable for the experiment. Most importantly, it can effectively capture frequencies in the range of 0.35 kHz to 10 kHz. This is because it is able to detect the bearing fault frequencies which are typically in the medium to high frequency range. Lastly, it has a low transverse sensitivity which means it is less likely to detect acceleration in different axes from the main sensing direction (Kistler Instrument Corporation, 2008).

For the ball bearings, the Asahi UC201 and SKF 6002 were selected for the experiment, as illustrated in Figure 3.4. The Asahi UC201 was chosen because its pillow block housing can be easily mounted on the test rig. Additionally, it features a set-screw locking mechanism that prevents rotational slip between the shaft and the bearing. The SKF 6002 was selected to provide analysis results for bearings of different diameters. To assemble the 6002 bearing on the same test rig, a steel housing and shaft were designed and fabricated, as shown in Figures 3.5 and 3.6, respectively. The 6002 bearing was secured in the housing with a housing shoulder and an acrylic cover. The housing and shaft were fabricated with a 0–5 μm interference fit with the bearing to ensure a tight, slip-free assembly.

The AC motor used in the setup is a Siemens D-91056, it was connected to a Delta Electronics VFD007L21A variable frequency drive. The

AC motor and VFD are displayed in Figure 3.7 and Figure 3.8 respectively. This enables the flexible adjustment of the rotational speed of the motor. Equation 3.1 is used to correlate the VFD frequency to the actual motor speed. Since the motor has 4 poles, the motor will be operating at 1500 RPM when it is supplied with 50 Hz frequency.

$$N_s = \frac{120f}{p} \tag{3.1}$$

where

N_S = synchronous speed (RPM)

f = frequency of supply (Hz)

p = number of poles

Table 3.1: Model name and technical specifications for each component.

Description	**Model Name**	**Technical Specifications**
Data acquisition system (DAQ)	NI-9234	Sampling rate = 51.2 kS/s Number of channels = 4 (analogue) ADC resolution = 24 bits Input measurement range = ± 5 V
Accelerometer	Kistler 8704B50T	Measuring range = ± 50g Sensitivity = 100 mV/g Transverse sensitivity < 1.5% Supply voltage = 18 V to 30 V Frequency response = 0.35 kHz to 10 kHz Minimum threshold = 0.005 g_{rms}
AC Motor	Siemens D-91056	Number of Pole = 4 Frequency = 50 / 60 Hz Rated Power = 0.37 / 0.45 kW Rated Speed = 1370 RPM / 1670 RPM
Variable Frequency Drive	Delta Electronics VFD007L21A	Input = 3-phase 5.1A 200-240V 50/60Hz Output = 3-phase 0-240V 4.2A 1HP Frequency range = 1-400 Hz
Ball Bearings	Asahi UC201	Bore diameter = 12 mm

		Outer diameter = 47 mm Width = 17 mm
	SKF 6002	Bore diameter = 15 mm Outer diameter = 32 mm Width = 9 mm

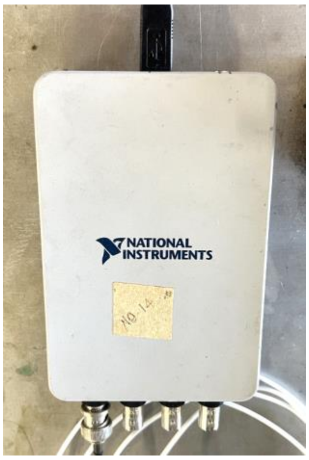

Figure 3.2: NI-9234 data acquisition system.

Figure 3.3: Kistler 8704B50T Accelerometer.

Figure 3.4: UC201 bearing (left) and SKF 6002 bearing (right).

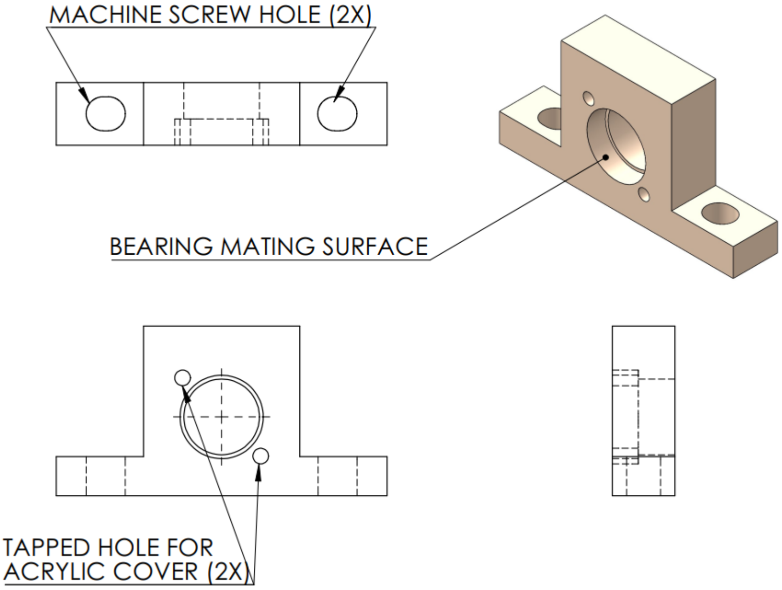

Figure 3.5: Engineering drawing of housing designed for 6002 bearing.

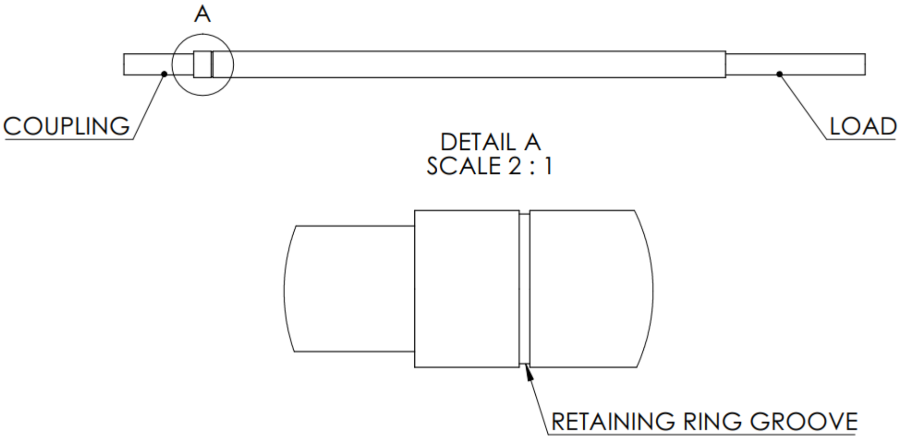

Figure 3.6: Engineering drawing of shaft designed for 6002 bearing.

Figure 3.7: Siemens D-91056 AC motor.

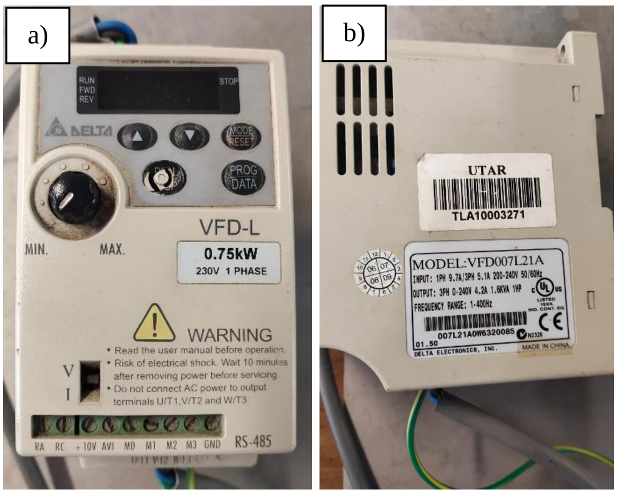

Figure 3.8: Delta Electronics VFD007L21A variable frequency drive: (a) Top view; (b) Side view.

3.3.2 Preparation of Defective Bearings

To create bearings without lubrication, as shown in Figure 3.9, the process began by removing the factory-packed bearing grease using pressurized air. Afterwards, the bearing was degreased with brake cleaner fluid, as shown in Figure 3.10. Brake cleaner fluid typically contains compounds such as acetone, methyl acetate, and hydrocarbons, making it highly effective at dissolving grease without leaving residue (Gatzke and Sobon, 2000). The aerosol was used in a well-ventilated area to disperse hazardous fumes. Since the aerosol is flammable, it was kept away from any ignition sources, such as sparks or open flames.

Figure 3.9: UC201 bearing without lubrication.

Figure 3.10: Toyo-G Brake Cleaner.

The next defect involved the contamination of bearing grease with particles, specifically sand and metal particles. The sand was passed through a 600 µm sieve before being mixed with the bearing grease. The metal chips were collected from bandsaw scrap and consisted of chips from various materials, including mild steel, aluminium, and stainless steel. The metal chip particles were then combined with the bearing grease to simulate the condition of lubricant contamination. The bearings contaminated with metal and sand are shown in Figures 3.11 and 3.12, respectively.

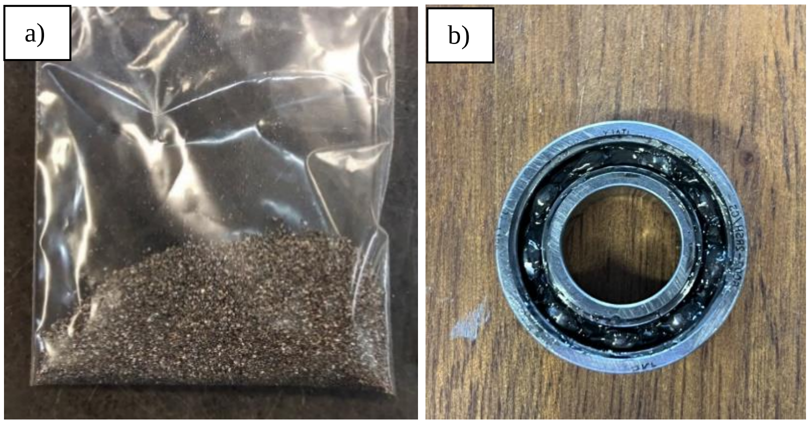

Figure 3.11: Metal-contaminated bearing: (a) Metal chip collected from bandsaw; (b) Bearing contaminated with metal particles.

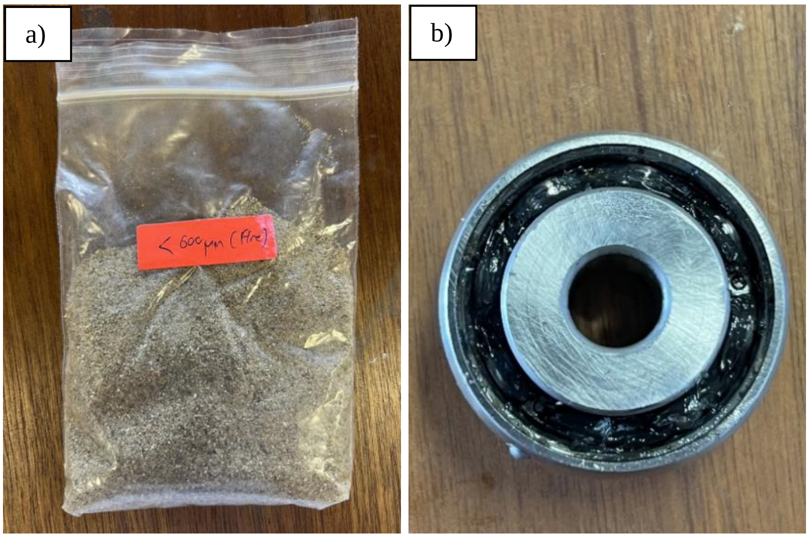

Figure 3.12: Sand-contaminated bearing: (a) Sand after passing through 600 μm sieve; (b) Bearing contaminated with sand particles.

To create a defect on the outer race of the bearing, a hole was drilled to form an abnormality where the ball bearing would repeatedly collide as it rotated around the race. The process began by clamping the outer race securely on a machining centre. The bearing was positioned so that the drill bit did not come into contact with any of the bearing balls when penetrating the outer race. Using a 3.5 mm carbide drill bit, the hole was carefully drilled. Initially, the drill bit was slowly brought into contact with the outer race to create a small dent, similar to the function of a centre punch. The drill was then slowly advanced and retracted to remove chips. This process continued until the outer race was fully penetrated, as shown in Figure 3.13. Proper lubrication was maintained throughout the procedure to prevent the drill bit from overheating, which could have affected the precision of the hole or damaged the bearing material.

Figure 3.13: UC201 bearing with outer race damage.

Next, the bearings were treated with acid to induce corrosion. Two concentrations of hydrochloric acid (HCl) were prepared, namely 1 mol/L or 1M (3.65 wt%) and 6 mol/L or 6M (21.88 wt%). The diluted acid solution was made by adding concentrated HCl to a volume of distilled water and thoroughly mixing the solution. The bearings were submerged in the acidic solution for 15 minutes, then rinsed with distilled water to halt further reaction. The end product of the reaction is shown in Figure 3.14.

Figure 3.14: Bearing after corrosive reaction with acid: (a) HCl 1M; (b) HCl 6M.

3.3.3 Procedure for Test Rig Setup and Data Collection

The setup for the experimental test rig and the procedure for data collection are elaborated in this subsection. An overview of the test rig is displayed in Figure 3.15. To set up the experimental test rig, the bearings were first assembled into their respective housings. For the UC201 bearing, the locking notch on the bearing was aligned with the housing groove. Then, the bearing was pivoted with a tool such as an Allen key to properly rotate it into position. Next, the bearing units were mounted onto the test rig block using 3/8" screws. Once the screws were tightened, the shaft was inserted through the bearings' bore. Lastly, the set screws on the coupling and bearings were tightened, and the rotating load was attached.

For the 6002 bearing, it was inserted into the housing by being tapped with a hammer and a piece of soft metal. The bearing was knocked with moderate force until contact was made with the bearing shoulder. Next, the acrylic cover was tightened to secure the bearing in place. At this point, the assembly process became similar to that of the UC201 bearing. However, since the 6002 bearing does not feature set-screw locking, the shaft had to be tapped into position during assembly.

After assembly, the signal acquisition module was connected to a computer using a USB cable (Type A Plug to Type B Plug). The accelerometer was then connected to channel 0 of the DAQ using a BNC cable. It was mounted in the radial direction of the bearing housing to maximize effectiveness. The accelerometer could be mounted using either adhesive or stud-based methods. Once connected, LabView software was activated to begin acquiring vibration signals from the accelerometer. To initiate data logging, the VFD was set to the desired frequency before being activated. The accelerometer sent a voltage signal to the DAQ, proportional to the acceleration. The recording of vibration data began after the test rig operated at the specified speed for at least 30 seconds. Vibration monitoring was performed for at least 90 to 120 seconds at each speed. The motor was operated at speeds ranging from 600 RPM to 1800 RPM, in intervals of 300 RPM.

For the Remaining Useful Life (RUL) experiment, the test rig was operated continuously while data for the vibration indicators were collected at 1-minute intervals. Based on preliminary testing, the metal-contaminated bearing was identified as the most suitable damage type for the RUL test. Preliminary testing also identified RMS acceleration as a prominent indicator for tracking bearing degradation. In this setup, the metal-contaminated bearing was placed on the motor side, while a healthy bearing was installed on the driven side. The rig operated at a constant speed of 1500 RPM under load throughout the experiment.

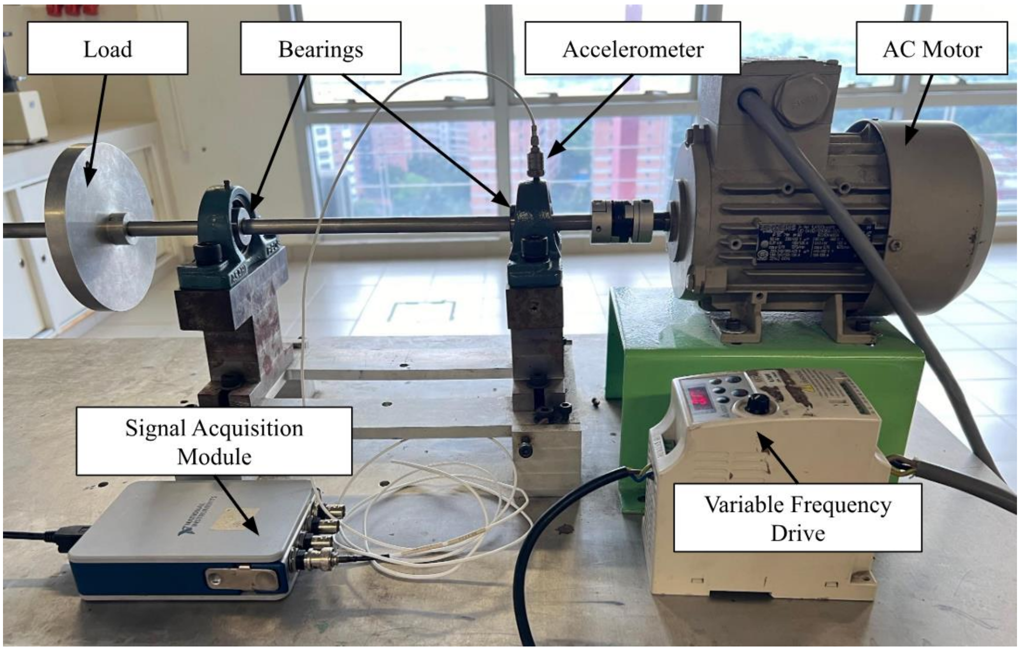

Figure 3.15: Labelled diagram of the experimental test rig.

3.3.4 Vibration Monitoring Algorithm

The summary of the vibration monitoring algorithm is shown in Figure 3.16. In short, the low frequency acceleration wave is used to derive velocity and displacement, along with their respective spectrum. On the other hand, high frequency acceleration is used to obtain high-frequency acceleration spectrum, envelope spectrum, and vibration indicators.

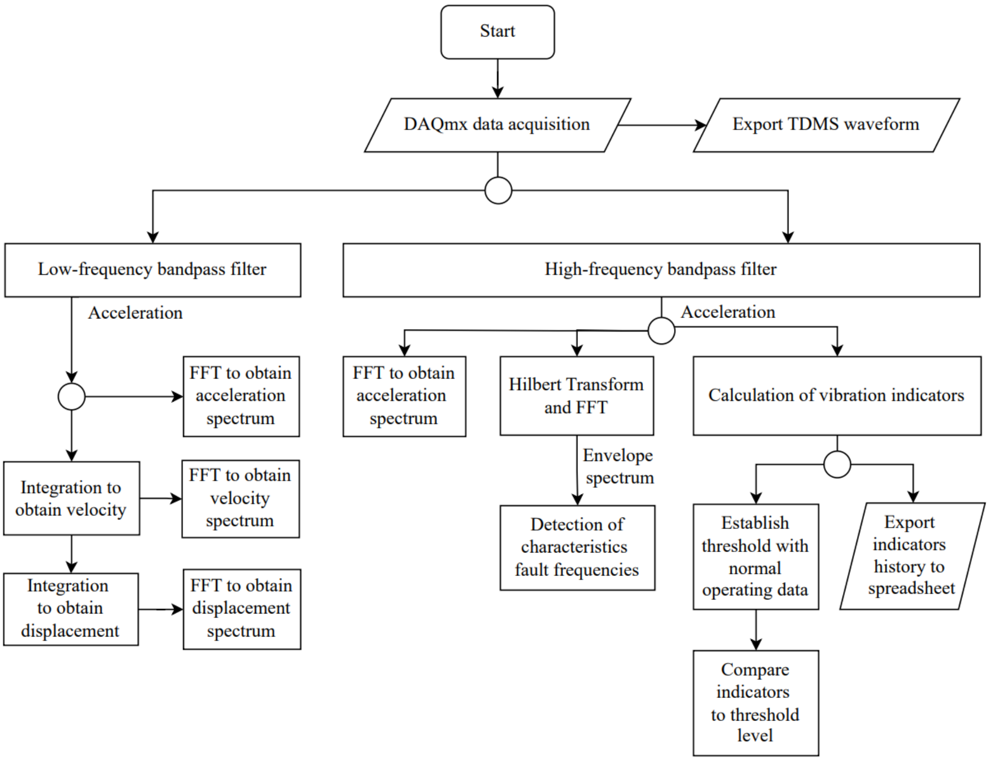

Figure 3.16: Flowchart of the vibration monitoring algorithm.

The data acquisition process was carried out using the DAQmx Data Acquisition Palette. The palette contained many data acquisition VIs (Virtual Instruments), which are the fundamental building blocks of LabVIEW programs. As shown in Figure 3.17, the first step involved creating a virtual channel and assigning it to the physical channel connected to the accelerometer. The input type was set to Analog Input Acceleration. The minimum and maximum values for the channel were set to ±5, matching the input range of the NI-9234 (National Instruments, 2024). The sampling rate was then used to determine the acquisition rate for the virtual channel.

Next, the DAQmx Read VI was configured to receive an analogue single-channel waveform with multiple samples. For instance, if the number of samples per channel was set to 25,600, the VI waited until the previous task had acquired 25,600 samples before reading them. This ensured accurate synchronization and data collection from the accelerometer.

The original waveform was filtered with a bandpass filter to obtain the acceleration waveform for high frequencies, as shown in Figure 3.18. In this experiment, the low cutoff frequency was set to 1 kHz, while the high cutoff frequency was set to 10 kHz. For the acceleration graph, the x-axis was scaled based on the reciprocal of the number of samples. Since 25,600 samples were collected per second, the axis was adjusted to accurately represent time.

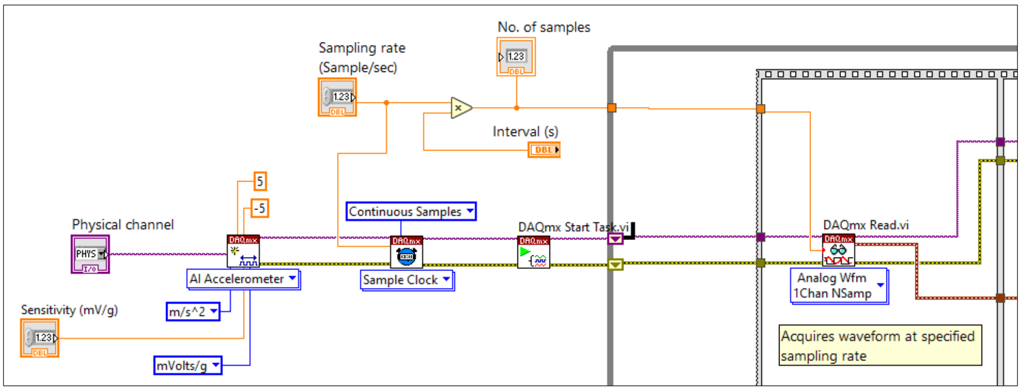

Acquires waveform at specified sampling rate

Figure 3.17: LabVIEW code for waveform acquisition.

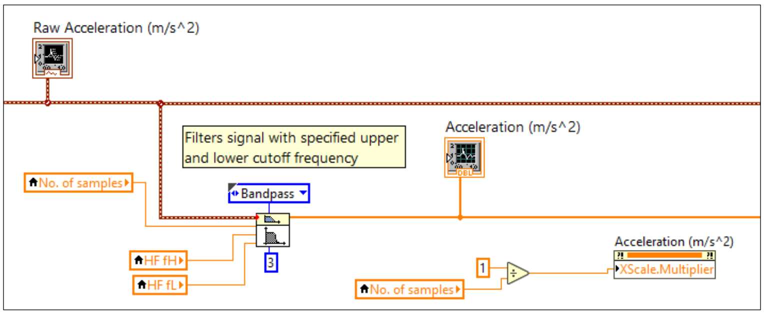

Filters signal with specified upper and lower cutoff frequency

Figure 3.18: LabVIEW code to obtain high frequency acceleration.

To obtain velocity, the low-frequency acceleration was first integrated to produce a velocity waveform, as shown in Figure 3.19. However, this initial waveform often included unwanted trends or distortions, which were undesirable. To correct this, the velocity waveform underwent curve fitting to obtain the line of best fit. The final velocity waveform was obtained after removing the trend. The velocity waveform was then scaled by a factor of 1,000 to convert the units to mm/s. Next, the root mean square (RMS) value of the velocity waveform was calculated. To derive displacement, the velocity waveform was integrated and corrected using curve fitting. The resulting displacement waveform was multiplied by 1,000,000 to convert it into micrometers (µm). The peak-to-peak displacement was determined by calculating the difference between the maximum and minimum displacement values.

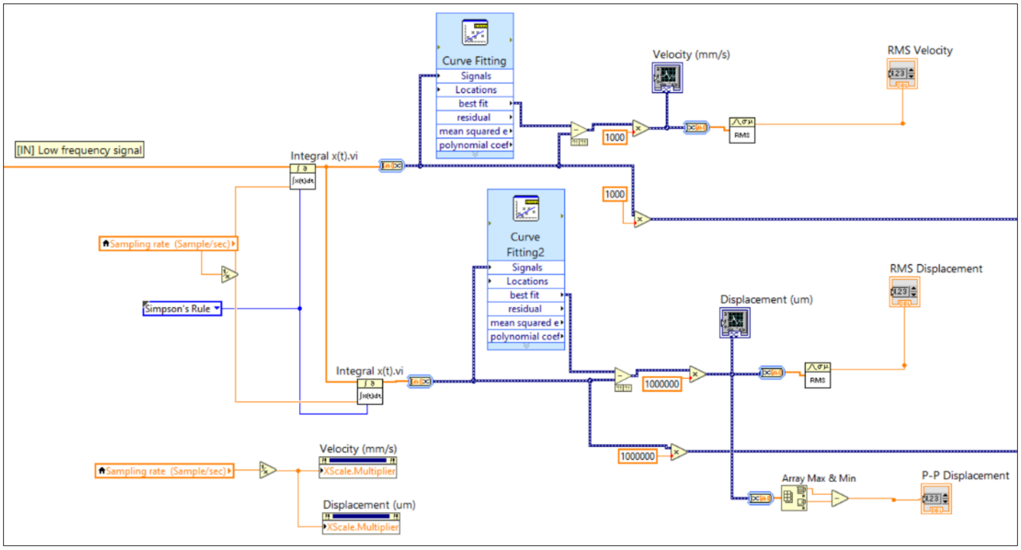

Figure 3.19: LabVIEW code for the integration and curve fitting of velocity and displacement.

Before the Fast Fourier Transform (FFT) was applied, a Hanning window was used to reduce spectral leakage by attenuating the signal at the edges, as shown in Figure 3.20. This process reduced abrupt discontinuities and prevented spectral energy from spreading across frequency bins, which leads to improved frequency measurements. After windowing, the FFT was performed on the signal, as illustrated in Figure 3.21. The resulting output was divided by the number of samples. This normalization is required because the amplitude in the FFT output is proportional to the total number of samples collected over a time window. While the FFT produces an array of complex numbers, only the magnitude was extracted for analysis. The FFT output array was extracted up to the Nyquist frequency only, which is half the sampling rate, as frequencies beyond this point are aliased and do not provide an accurate representation. Finally, the FFT output was multiplied by a factor of two, as the FFT represents both positive and negative frequency components symmetrically. This means the energy of each frequency is distributed between the positive and negative halves of the spectrum. Since only the positive frequencies are considered here, the output was scaled to reflect the true amplitude of the signal (Fahy and Pérez, 1993).

In Figure 3.22, the Hilbert transform was applied to the vibration signal to obtain its envelope signal. To construct the envelope waveform, the magnitude of the Hilbert transform corresponded to the Y values, while the reciprocal of the sampling rate represented the small changes in time along the X axis. The envelope signal was then passed through a Hanning window before the FFT converted it into the envelope spectrum.

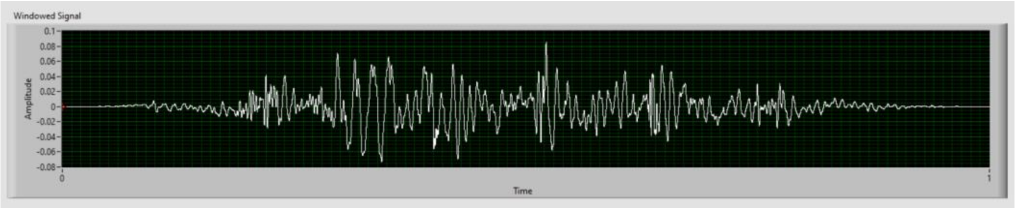

Figure 3.20: Scaled time domain window using Hanning window.

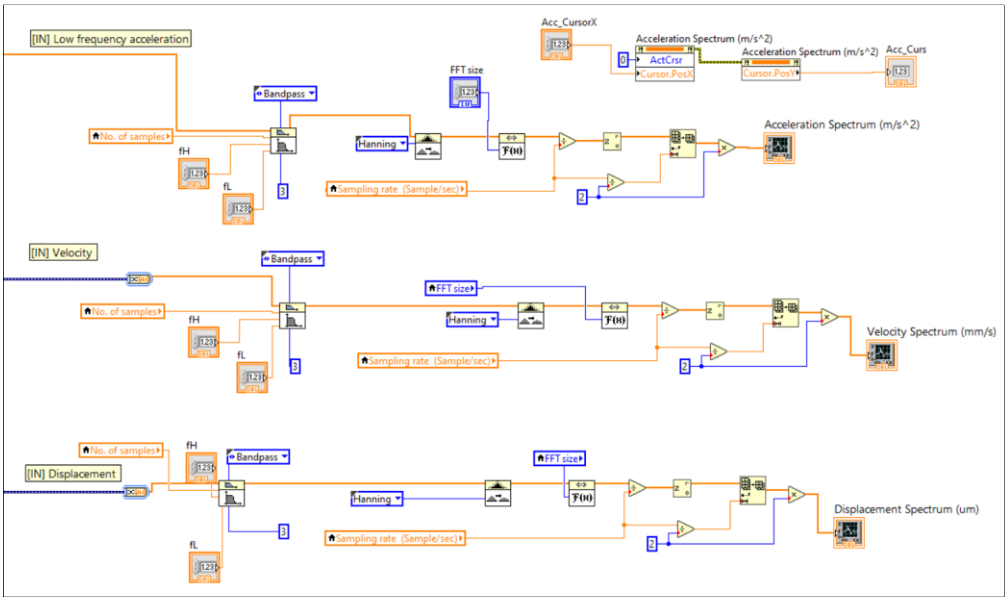

Figure 3.21: Frequency spectrum for acceleration, velocity, and displacement at low frequency.

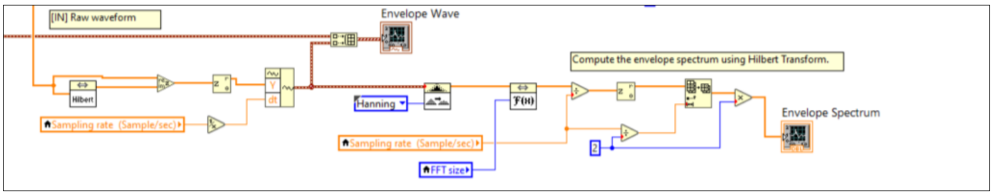

Figure 3.22: LabVIEW code for envelope spectrum.

Figure 3.23 shows the graphical code for creating a new TDMS file. The file name consists of user-defined text, which is automatically appended with the current date and time. When the "Save to TDMS" button is activated, the TDMS Write VI begins recording the waveform acquired from the physical channel. Additionally, the time elapsed since the start of waveform logging is displayed. Figure 3.24 shows an example of the recorded TDMS waveform for a duration of about 53 seconds. Figure 3.25 shows the code used to build the graph for the vibration indicators. The process begins by initializing an empty array. Each new value for the vibration indicator is appended to this array, and the array is fed back into itself to retain previous values. This allows for a continuous update of the graph. If the "Refresh" button is activated, the “Select” function is triggered, which returns an empty array. This effectively resets the graph by clearing all previous values in the array.

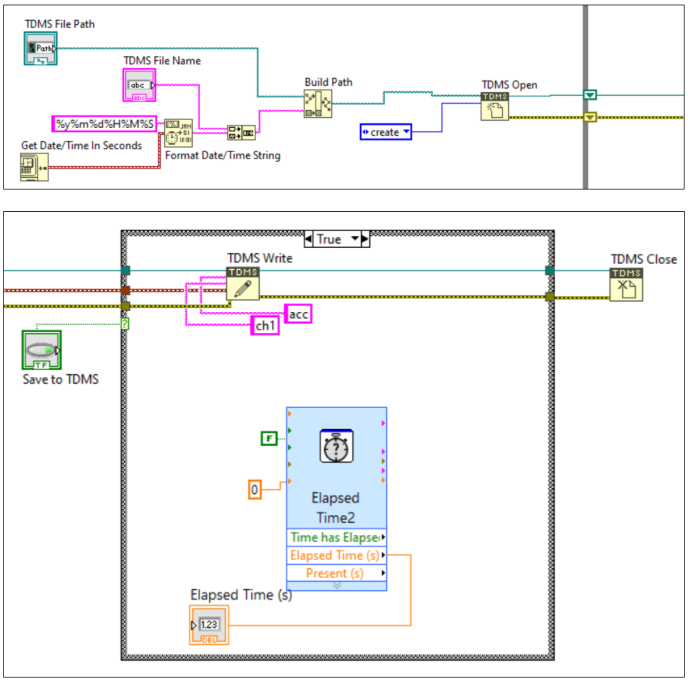

Figure 3.23: LabVIEW code for to open and read TDMS file.

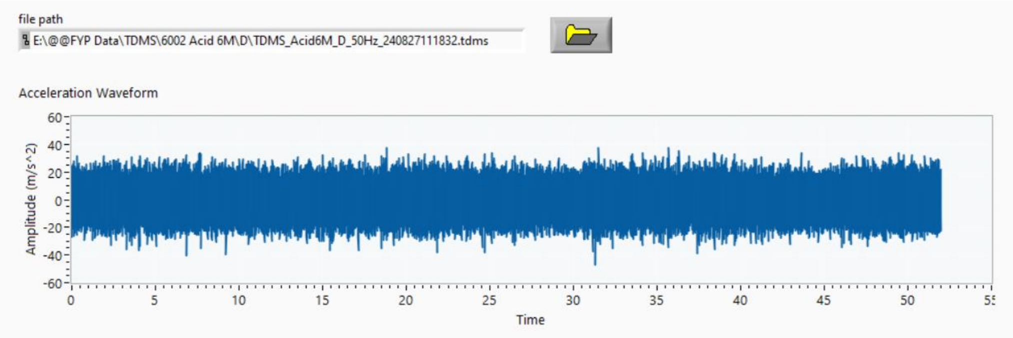
file path: E:\@@FYP Data\TDMS\6002 Acid 6M\D\TDMS_Acid6M_D_50Hz_240827111832.tdms

Figure 3.24: Example of TDMS waveform exported by the program.

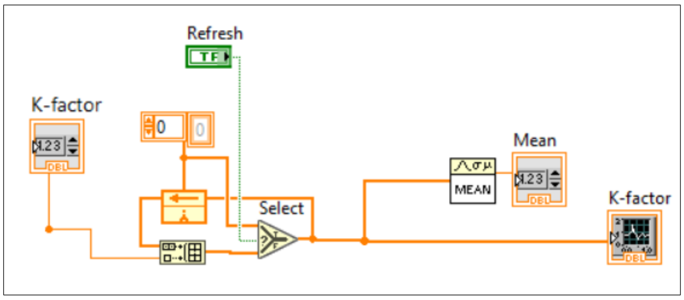

Figure 3.25: LabVIEW code to build and refresh graph.

The characteristic fault frequencies were calculated using equations from the literature. In Figure 3.26, the dimensions of UC201 will be used for calculations by default. By activating the "Switch Bearing" option, the program will instead use the dimensions of 6002 bearing. The specific parameters used in the calculations are provided in Table 3.2. Once the fault frequencies were computed, they were displayed on the graph as cursors. This allows for easier visual tracking and analysis. In Figure 3.27, the harmonics were calculated and displayed on the envelope spectrum based on the rotor speed. This helped to differentiate fault frequencies from the fundamental frequency and its harmonics. Additionally, threshold levels can be set to evaluate the vibration indicator. Two levels of warning are established, namely Caution and Danger. Caution level serves as an early warning, while Danger level indicates critical issue.

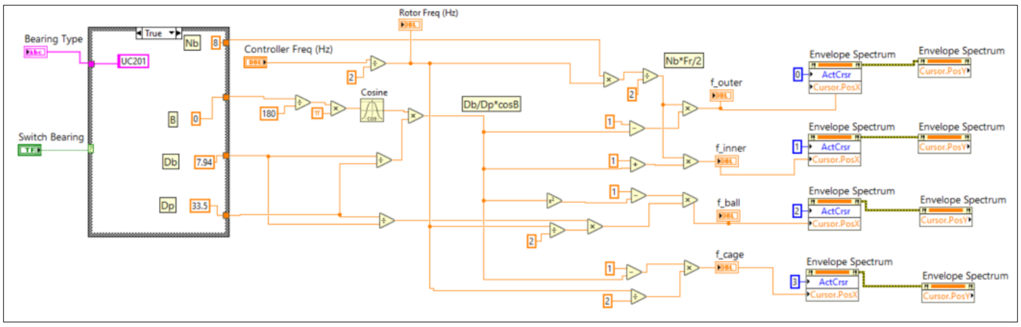

Figure 3.26: LabVIEW code for the calculation of characteristics fault frequency and the display of cursor.

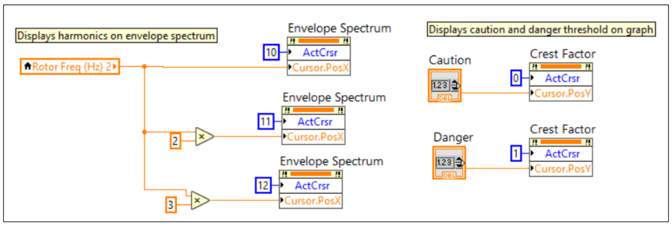

Figure 3.27: LabVIEW code for the display of harmonics and threshold level.

Table 3.2: Parameters used for calculation of characteristic fault frequencies.

Bearing model	**UC201**	**6002**
Number of balls, N_B	8	9
Ball diameter, D_B	7.94 mm	4.76
Pitch diameter, D_P	33.5 mm	23.5
Contact angle, β	0°	0°

The code used for the computation of vibration indicators are presented in Figure 3.28. After the indicators are calculated, they can be exported to a spreadsheet. Figure 3.29 shows the code used to write the indicators to an Excel spreadsheet. Initially, all of the signals were merged into a single output signal. The indicators were then recorded in different spreadsheet columns which corresponds to different signal index. Additionally, a timestamp was included for each data point to track when the measurements were taken. Figure 3.30 displays the spreadsheet exported by the program.

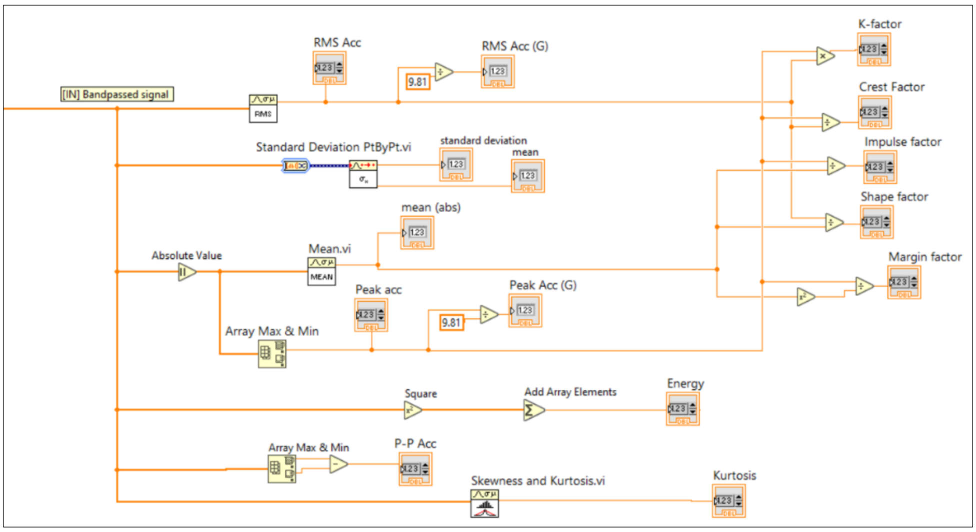

Figure 3.28: LabVIEW code for the computation of vibration indicators.

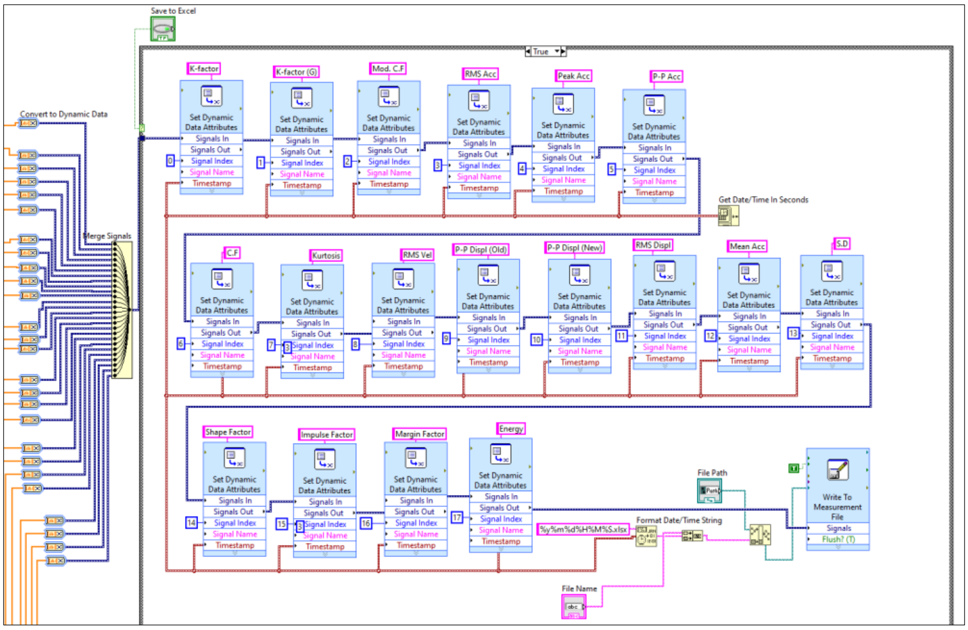

Figure 3.29: LabVIEW code to write indicators into delimited spreadsheet.

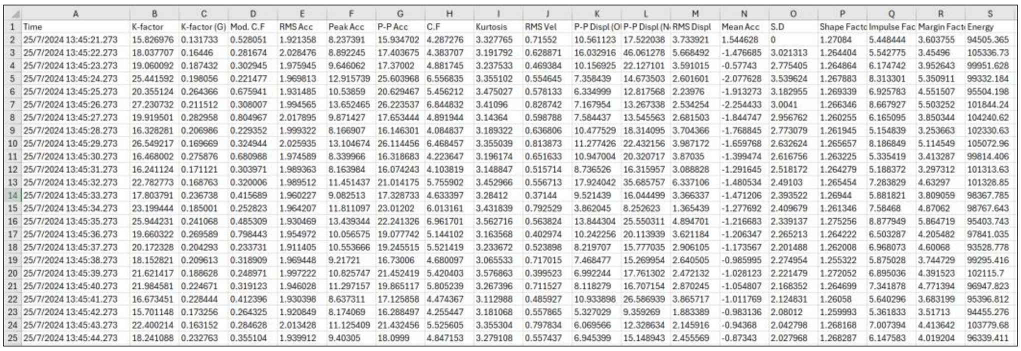

	A	B	C	D	E	F	G	H	I	J	K	L	M	N	O	P	Q	R	S
1	Time	K-factor	K-factor (G)	Mod. C.F	RMS Acc	Peak Acc	P-P Acc	C.F	Kurtosis	RMS Vel	P-P Displ (O	P-P Displ (N	RMS Displ	Mean Acc	S.D	Shape Facto	Impulse Fac	Margin Fact	Energy
2	25/7/2024 13:45:21.273	15.826976	0.131733	0.528051	1.921358	8.237391	15.934702	4.287276	3.327765	0.71552	10.561123	17.522038	3.733921	1.544628	0	1.27084	5.448444	3.603755	94505.365
3	25/7/2024 13:45:22.273	18.037707	0.16446	0.281674	2.028476	8.892245	17.403675	4.383707	3.191792	0.628871	16.032916	46.061278	5.668492	-1.476685	3.021313	1.264404	5.542775	3.45496	105336.73
4	25/7/2024 13:45:23.273	19.060092	0.187432	0.302945	1.975945	9.646062	17.37002	4.881745	3.237533	0.469384	10.156925	22.127101	3.591015	-0.57743	2.775405	1.264864	6.174742	3.952643	99951.628
5	25/7/2024 13:45:24.273	25.441592	0.198056	0.221477	1.969813	12.915739	25.603968	6.556835	3.355102	0.554645	7.358439	14.673503	2.601601	-2.077628	3.539624	1.267883	8.313301	5.350911	99332.184
6	25/7/2024 13:45:25.273	20.355124	0.264366	0.675941	1.931485	10.53859	20.629467	5.456212	3.475027	0.578133	6.334999	12.817568	2.23976	-1.913273	3.182955	1.269339	6.925783	4.551507	95504.198
7	25/7/2024 13:45:26.273	27.230732	0.211512	0.308007	1.994565	13.652465	26.223537	6.844832	3.41096	0.828742	7.167954	13.267338	2.534254	-2.254433	3.0041	1.266346	8.667927	5.503252	101844.24
8	25/7/2024 13:45:27.273	19.919501	0.282958	0.804967	2.017895	9.871427	17.653444	4.891944	3.14364	0.598788	7.584437	13.545563	2.681503	-1.844747	2.956762	1.260255	6.165095	3.850344	104240.62
9	25/7/2024 13:45:28.273	16.328281	0.206986	0.229352	1.999322	8.166907	16.146301	4.084837	3.189322	0.636806	10.477529	18.314095	3.704366	-1.768845	2.773079	1.261945	5.154839	3.253663	102330.63
10	25/7/2024 13:45:29.273	26.549217	0.169669	0.324944	2.025935	13.104674	26.114456	6.468457	3.355039	0.813873	11.277426	22.432156	3.987172	-1.659768	2.632624	1.265657	8.186849	5.114549	105072.96
11	25/7/2024 13:45:30.273	16.468002	0.275876	0.680988	1.974589	8.339966	16.318683	4.223647	3.196174	0.651633	10.947004	20.320717	3.87035	-1.399474	2.616756	1.263225	5.335419	3.413287	99814.406
12	25/7/2024 13:45:31.273	16.241124	0.171121	0.303971	1.989363	8.163984	16.074243	4.103819	3.148847	0.515714	8.736526	16.315957	3.088828	-1.291645	2.518172	1.264279	5.188372	3.297312	101313.63
13	25/7/2024 13:45:32.273	22.782773	0.168763	0.320006	1.989512	11.451437	21.014175	5.755902	3.452966	0.556713	17.924042	35.685757	6.337106	-1.480534	2.49103	1.265454	7.283829	4.63297	101328.85
14	25/7/2024 13:45:33.273	17.803791	0.236738	0.415689	1.960227	9.082513	17.328733	4.633397	3.28412	0.37144	9.521439	16.044499	3.366337	-1.471206	2.393522	1.26944	5.881821	3.809059	98367.785
15	25/7/2024 13:45:34.273	23.199444	0.185001	0.252823	1.964207	11.811097	23.01202	6.013161	3.431839	0.792529	3.862045	8.252623	1.365439	-1.277692	2.409679	1.261346	7.58468	4.87062	98767.643
16	25/7/2024 13:45:35.273	25.944231	0.241068	0.485309	1.930469	13.439344	22.241326	6.961701	3.562716	0.563824	13.844304	25.550311	4.894701	-1.216683	2.339137	1.275256	8.877949	5.864719	95403.743
17	25/7/2024 13:45:36.273	19.660322	0.269589	0.798443	1.954972	10.056575	19.077742	5.144102	3.163568	0.402974	10.242256	20.113939	3.621184	-1.206347	2.265213	1.264222	6.503287	4.205482	97841.035
18	25/7/2024 13:45:37.273	20.172328	0.204293	0.233731	1.911405	10.553666	19.245515	5.521419	3.233672	0.523898	8.219707	15.777035	2.906105	-1.173567	2.201488	1.262008	6.968073	4.60068	93528.778
19	25/7/2024 13:45:38.273	18.152821	0.209613	0.318909	1.969448	9.21721	16.73006	4.680097	3.065533	0.717015	7.468477	15.269954	2.640505	-0.985995	2.274954	1.255322	5.875028	3.744729	99295.416
20	25/7/2024 13:45:39.273	21.621417	0.188628	0.248971	1.997222	10.825747	21.452419	5.420403	3.576863	0.399523	6.992244	17.761302	2.472132	-1.028123	2.221479	1.272052	6.895036	4.391523	102115.7
21	25/7/2024 13:45:40.273	21.984581	0.224671	0.319123	1.946028	11.297157	19.865117	5.805239	3.267396	0.711527	8.118279	16.707154	2.870245	-1.054807	2.168352	1.264699	7.341878	4.771394	96947.823
22	25/7/2024 13:45:41.273	16.673451	0.228444	0.412396	1.930398	8.637311	17.125858	4.474367	3.112988	0.485927	10.933898	26.586939	3.865717	-1.011769	2.124831	1.26058	5.640296	3.683199	95396.812
23	25/7/2024 13:45:42.273	15.701148	0.173256	0.264325	1.920849	8.174069	16.288497	4.255447	3.181068	0.557865	5.327029	9.359269	1.883389	-0.983136	2.08012	1.259993	5.361833	3.51713	94455.276
24	25/7/2024 13:45:43.273	22.400214	0.163152	0.284628	2.013428	11.125409	21.432456	5.525605	3.355304	0.797834	6.069566	12.328634	2.145916	-0.94368	2.042798	1.268168	7.007394	4.413642	103779.68
25	25/7/2024 13:45:44.273	18.241088	0.232763	0.355104	1.939912	9.40305	18.0999	4.847153	3.279108	0.557437	6.945399	15.148943	2.455569	-0.87343	2.027968	1.268287	6.147583	4.019204	96339.411

Figure 3.30: The output spreadsheet of vibration indicators.

Figure 3.31 illustrates the main controls of the program. For configuration, the physical channel is assigned to the channel that is physically connected to the accelerometer, typically designated as channel 0. Next, the sensitivity of the accelerometer and the type of bearing are selected accordingly. In this study, the sampling rate is fixed at 25.6 kS/s (kilo-samples per second), with the processing interval set to 1 second. As a result, the program performs real-time monitoring by processing data every 25,600 samples. Before collecting vibration data, the program requires the input of the VFD frequency to calculate the bearing's characteristic frequency. The recorded indicators can be exported as an Excel spreadsheet, while the original waveform can be saved in TDMS file format.

Figure 3.32 displays the low-frequency monitoring panel. The first graph shows the acceleration spectrum for low-frequency vibration, which is filtered between 5 Hz and 300 Hz. The waveforms for velocity and displacement are also displayed, with a high cutoff frequency of 1,200 Hz. Lastly, the frequency spectrum for both velocity and displacement can be obtained from these waveforms, with a high cutoff frequency of 300 Hz.

Figure 3.33 shows the monitoring panel for high-frequency vibration. For the experiments, the cutoff frequencies were set to allow only signals between 1 kHz and 10 kHz to pass through without attenuation. Besides displaying the waveform and spectrum, the envelope spectrum of the high-frequency signal is also shown. The calculated characteristic fault frequencies are also displayed, based on rotor speed and bearing type.

Figure 3.34 presents graphs of various vibration indicators, such as the K-factor, kurtosis, and crest factor. These graphs are updated every second, and the mean value over the entire measurement duration is also displayed. A "Refresh" button allows users to reset the graphs. Additionally, threshold levels can be input and displayed on the graphs for easier comparison. All indicators are computed using high-frequency signals, except for RMS velocity, peak-to-peak displacement, and RMS displacement.

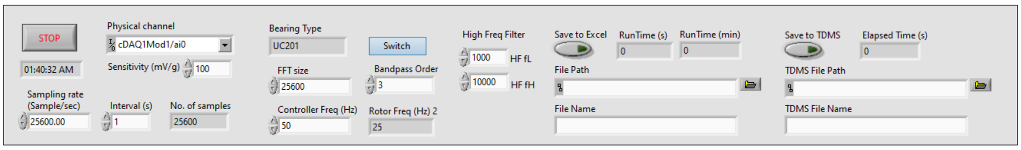

01:40:32 AM

Physical channel: cDAQ1Mod1/ai0

Sensitivity (mV/g): 100

Sampling rate (Sample/sec): 25600.00

Interval (s): 1

No. of samples: 25600

Bearing Type: UC201

FFT size: 25600

Bandpass Order: 3

Controller Freq (Hz): 50

Rotor Freq (Hz) 2: 25

High Freq Filter: 1000 HF fL; 10000 HF fH

Save to Excel

RunTime (s): 0

RunTime (min): 0

File Path

File Name

Save to TDMS

Elapsed Time (s): 0

TDMS File Path

TDMS File Name

Figure 3.31: Main control panel of the monitoring program.

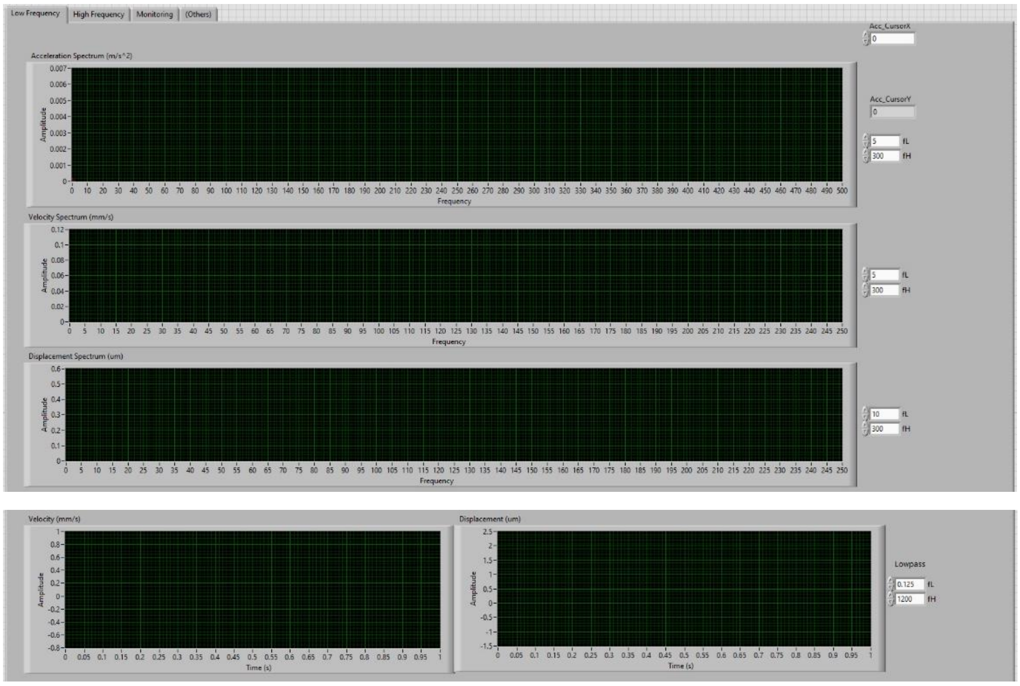

Acc_CursorX: 0

Acc_CursorY: 0

5 fL; 300 fH

5 fL; 300 fH

10 fL; 300 fH

Lowpass: 0.125 fL; 1200 fH

Figure 3.32: Low frequency monitoring panel.

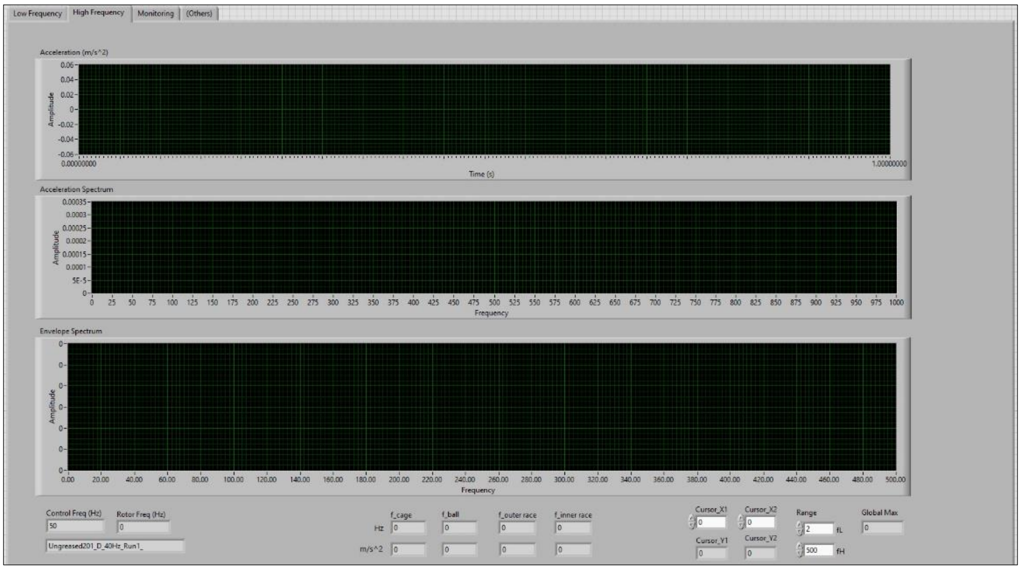

Control Freq (Hz): 50

Rotor Freq (Hz): 0

Ungreased201_D_40Hz_Run1_

	f_cage	f_ball	f_outer race	f_inner race
Hz	0	0	0	0
m/s^2	0	0	0	0

Cursor_X1: 0

Cursor_X2: 0

Cursor_Y1: 0

Cursor_Y2: 0

Range: 2 fL; 500 fH

Global Max: 0

Figure 3.33: High frequency monitoring panel.

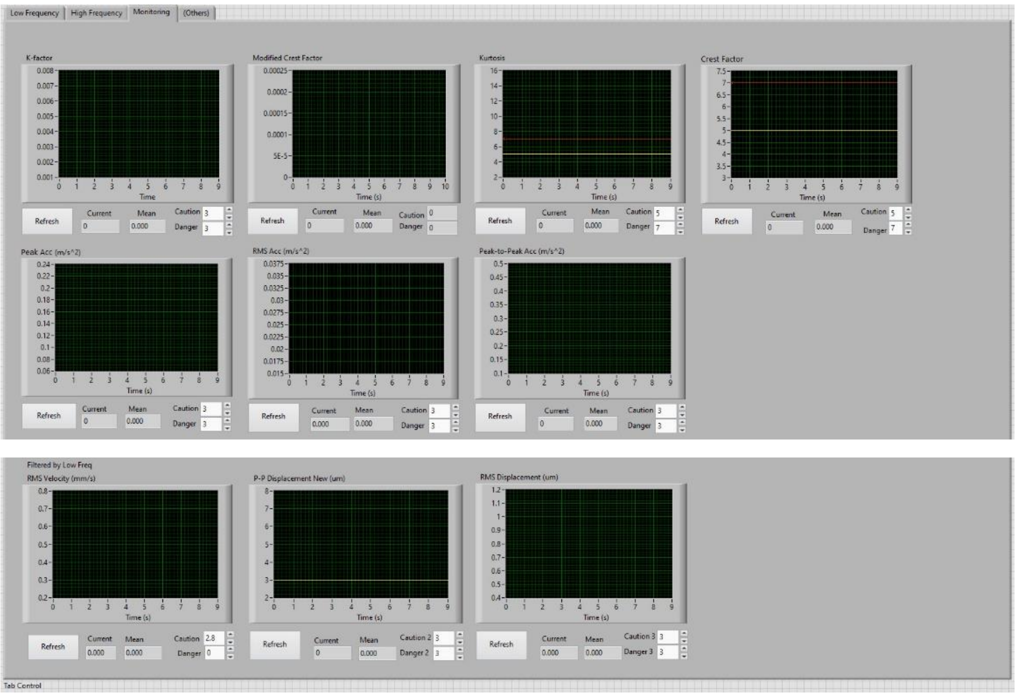

K-factor: Current 0 Mean 0.000 Caution 3 Danger 3

Modified Crest Factor: Current 0 Mean 0.000 Caution 0 Danger 0

Kurtosis: Current 0 Mean 0.000 Caution 5 Danger 7

Crest Factor: Current 0 Mean 0.000 Caution 5 Danger 7

Peak Acc (m/s^2): Current 0 Mean 0.000 Caution 3 Danger 3

RMS Acc (m/s^2): Current 0.000 Mean 0.000 Caution 3 Danger 3

Peak-to-Peak Acc (m/s^2): Current 0 Mean 0.000 Caution 3 Danger 3

Filtered by Low Freq

RMS Velocity (mm/s): Current 0.000 Mean 0.000 Caution 2.8 Danger 0

P-P Displacement New (um): Current 0 Mean 0.000 Caution 2 3 Danger 2 3

RMS Displacement (um): Current 0.000 Mean 0.000 Caution 3 3 Danger 3 3

Figure 3.34: Vibration indicators monitoring panel.

3.4 Summary

In summary, this chapter outlined the components used in the experiment and the general procedure for preparing defective bearings. The fault detection algorithm is based on deriving velocity and displacement, utilizing the envelope spectrum, and calculating vibration indicators. The validation of the algorithm primarily relies on experimental work, though cross-validation using a commercial system is also possible.

CHAPTER 4

RESULTS AND DISCUSSION

4.1 Introduction

This chapter explores various vibration characteristics, such as acceleration waveform, envelope waveform, and vibration indicators in different types of bearing defect. The vibration indicators include K-factor, RMS acceleration, crest factor, and kurtosis, among others. Additionally, the prediction of RUL will be investigated. The validation of the algorithms will be conducted through physical inspection and comparison of results with a commercial system.

4.2 Acceleration Waveform

Acceleration waveform is a simple and effective tool in diagnosing the bearing condition as it directly visualises the vibration behaviour of bearings. In this study, a 1-second acceleration waveform was captured for UC201 at 1500 RPM to analyse the vibration pattern and determine whether the bearing is defective. In Figure 4.1, the waveform of a healthy bearing is observed to have low vibration amplitude of around 5 m/s^2 and minimal sudden spikes in the signal. This serves as the baseline for comparison with other types of defects. The same observation is found in the study by Muniyappa and Praveen Krishna (2019), which indicates that healthy bearings also exhibit lower amplitude compared to their defective counterparts. Figure 4.2 shows the waveform of bearing without lubrication. The average vibration amplitude has increased to around 10 m/s^2 while the spikes in the signal also increased. Lubricating grease possesses properties such as wear protection and corrosion resistance. The grease will ensure that bearing raceways and rolling elements are separated by a thin film of lubricating oil. When bearings are not lubricated with bearing grease, it causes direct contact between the rough metal surfaces which significantly increasing friction and vibration (Zheng et al., 2021).

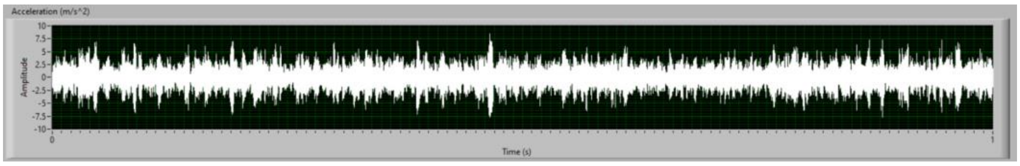

Figure 4.1: Waveform of healthy UC201 bearing.

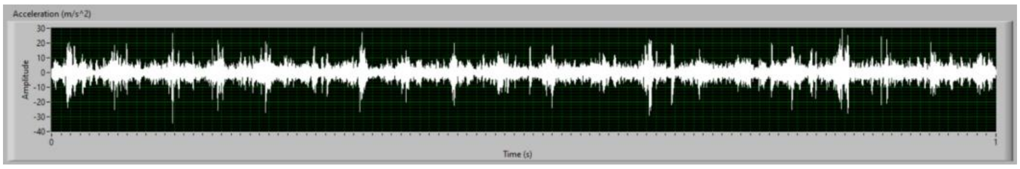

Figure 4.2: Waveform of UC201 bearing without lubrication.

Figure 4.3 shows the waveform of a metal-contaminated bearing. The vibration profile of the bearing exhibits an average amplitude of 5 m/s^2 with a generally noisy signal. Occasionally, there are sudden spikes with amplitudes around 15 m/s^2. These spikes are irregular and non-periodic, as the movements and collisions of metal particles inside the bearing are random. These metal particles cause impacts and rubbing as they become trapped between the bearing balls and the raceway, contributing to the erratic vibration patterns observed. Sand particles inside the bearing can also cause abrasion, which increases vibration levels. In Figure 4.4, the average vibration level of the sand-contaminated bearing is not particularly significant. However, when sand particles become trapped between the rolling elements and the raceway, they generate impulses that can reach magnitudes of up to 100 m/s^2. These sudden spikes in vibration can lead to the accelerated formation of spalls on the surfaces of the bearing components, further worsening the damage over time.

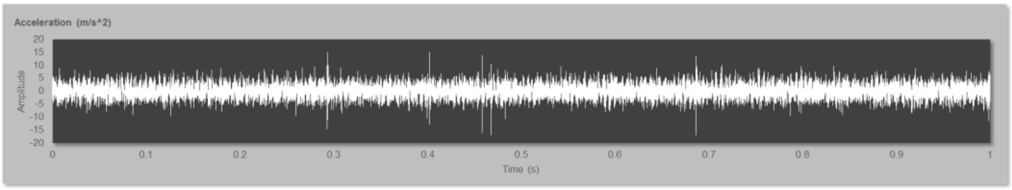

Figure 4.3: Waveform of UC201 bearing contaminated with metal particle.

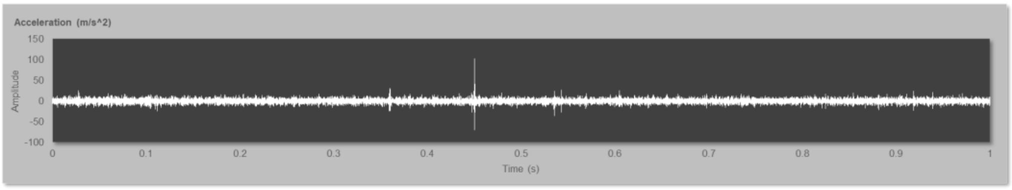

Figure 4.4: Waveform of UC201 bearing contaminated with sand particle.

Figure 4.5 shows the effect of damage on the bearing outer race which creates distinct spikes at regular intervals. The localized defect causes repeated impacts between bearing balls and raceway with each revolution. The spikes in vibration are consistently observed at a magnitude of around 50 m/s^2. The same waveform pattern for outer race damage was identified in the study by Wang et al. (2013).

Besides mechanical damage, damage can also occur in a bearing chemically. Figures 4.6 and 4.7 show the effect of an acidic medium on the vibration of bearings. After the bearing reacted with 1M HCl, the average vibration magnitude increased to around 5 m/s^2 while exhibiting some transient spikes in the signal, as shown in Figure 4.6. When the bearing reacted with 6M HCl, the spikes in the signal were much more significant, with magnitudes approaching 40 m/s^2. In Figure 4.7, the recurrence of the same spikes at constant intervals in the signal indicates that faults have locally developed at specific points in the bearing. Every time the bearing balls pass over the damaged area, a vibration spike is generated. With higher acid concentration, the corrosion rate is higher, resulting in severe degradation of bearing components. This leads to deep pitting and irregularity on the steel surface, causing a significant increase in vibrations.

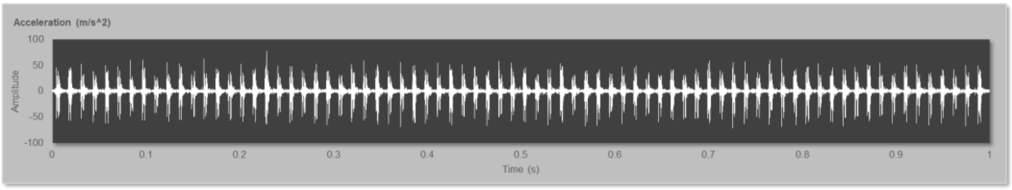

Figure 4.5: Waveform of UC201 bearing with outer race damage.

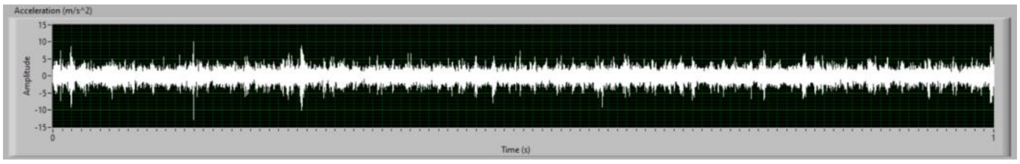

Figure 4.6: Waveform of UC201 bearing after corrosion with 1M HCl.

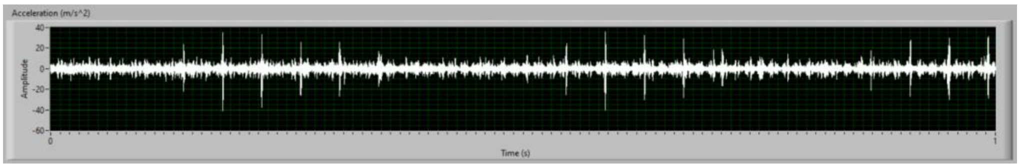

Figure 4.7: Waveform of UC201 bearing after corrosion with 6M HCl.

4.3 Envelope Spectrum

The envelope spectrum of 6002 bearing at the motor side is compared for speeds between 1500 RPM (25 Hz) and 1800 RPM (30 Hz). Table 4.1 and Table 4.2 shows the theoretical characteristics fault frequencies for UC201 and 6002, respectively.

Table 4.1: Characteristics fault frequencies for UC201 at various speeds.

Speed (RPM)	600	900	1200	1500	1800
FTF (Hz)	3.81	5.72	7.63	9.54	11.44
BSF (Hz)	19.91	29.87	39.82	49.78	59.73
BPFO (Hz)	30.52	45.78	61.04	76.30	91.56
BPFI (Hz)	49.48	74.22	98.96	123.70	148.44

Table 4.2: Characteristics fault frequencies for 6002 at various speeds.

Speed (RPM)	600	900	1200	1500	1800
FTF (Hz)	3.99	5.98	7.97	9.97	11.96
BSF (Hz)	23.67	35.51	47.34	59.18	71.02
BPFO (Hz)	35.89	53.83	71.77	89.71	107.66
BPFI (Hz)	54.11	81.17	108.23	135.29	162.34

In Figure 4.8, no peaks were observed in the envelope spectrum for the healthy bearing. The amplitude of the envelope spectrum was below 0.05 m/s^2, which is low and considered noise. Overall, this indicates that the bearing is not defective. Figure 4.9 shows the envelope spectrum of a bearing without lubrication. The spectrum is nearly identical to that of a healthy bearing, with only a slight increase in noise levels. Since there are no observable peaks, this indicates that no localized damage has formed at the targeted locations.

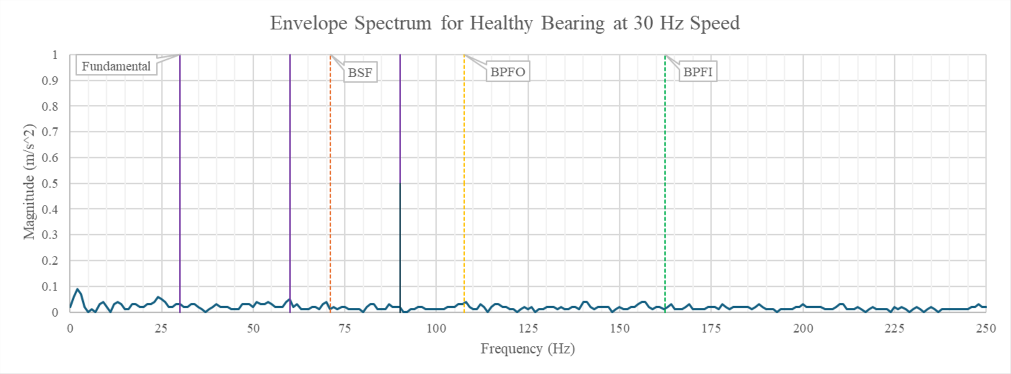

Figure 4.8: Envelope spectrum of 6002 bearing with healthy condition at 30 Hz speed.

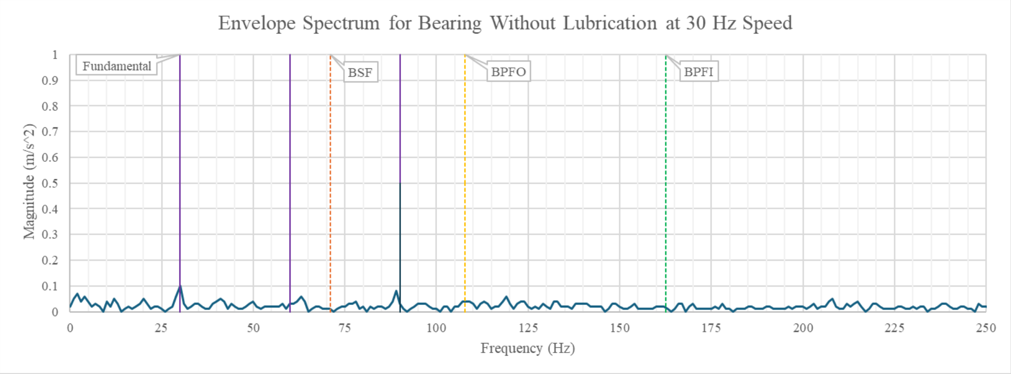

Figure 4.9: Envelope spectrum of 6002 bearing without lubrication at 30 Hz speed.

At the motor speed of 20 Hz, the algorithm successfully detected a peak at BPFO of 72 Hz, as illustrated in Figure 4.10 (a). The magnitude of the peak is 0.31 m/s^2, which is significantly higher than the noise level. At the motor speed of 30 Hz, the algorithm also detected a peak at 109 Hz, as shown in Figure 4.10 (b). This is close to the BPFO of 107.66 Hz, albeit with a slight error. There are also peaks at the harmonics of the BPFO, namely at 144 Hz (2X BPFO) and 217 Hz (3X BPFO).

As the speed increased, the magnitude of the peak also increased to 1.2 m/s^2, while the amplitude of the 2X harmonic rose to 1.68 m/s^2. This indicates that there is direct and severe damage to the outer race surface. The discrepancy in the BPFO detected may be due to the presence of slippage at higher speeds. Slip can occur between the bearing balls and the races. It is also possible that slippage occurred between the shaft and the bearing inner ring. The error analysis for BPFO is presented in Table 4.3. The percentage error observed in the experiment ranged from 0.31% to 1.24%. This variation is primarily due to the resolution of the envelope spectrum, which is limited to 1 Hz. Despite this limitation, the overall measurement of BPFO by the envelope spectrum remains accurate.

Figure 4.10: Envelope spectrum for 6002 bearing with outer race damage: (a) at 20 Hz speed; (b) at 30 Hz speed.

Table 4.3: Percentage error of BPFO observed in 6002 bearing with outer race damage.

Operating Speed (Hz)	BPFO (Hz)		Percentage Error (%)
	Theoretical	Experimental	

10	35.89	36	0.31
15	53.83	54	0.32
20	71.59	72	0.57
25	89.53	90	0.52
30	107.66	109	1.24

Figure 4.11 shows the envelope spectrum for a bearing after exposure to 1M HCl. A consistent peak is observed at the outer race fault frequency (BPFO), reaching a magnitude of 1.5 m/s^2. This serves as a significant indication for the fault formation on the outer race. Additional peaks are visible at the fundamental frequency of 30 Hz and its 2X harmonic at 60 Hz. Compared to the spectrum for healthy bearing conditions, the noise level has significantly increased, reaching up to 0.3 m/s^2. Figure 4.12 shows the envelope spectrum for a bearing that reacted with 6M HCl. A peak is observed at the BPFO, with magnitudes ranging from 0.4 m/s^2 to 0.6 m/s^2. There is also a strong peak of 0.6 m/s^2 at approximately 218 Hz, which likely corresponds to the 2X harmonic of the BPFO. The high noise level seen in both of these envelope spectrums can be attributed to the effects of acidic corrosion. Corrosion causes the bearing surfaces to become rough and uneven. This leads to the occurrence of continuous small impacts and increased friction as the bearing balls move over the damaged areas. These random impacts raise the overall noise level in the envelope spectrum, which masks the amplitude of specific fault frequencies.

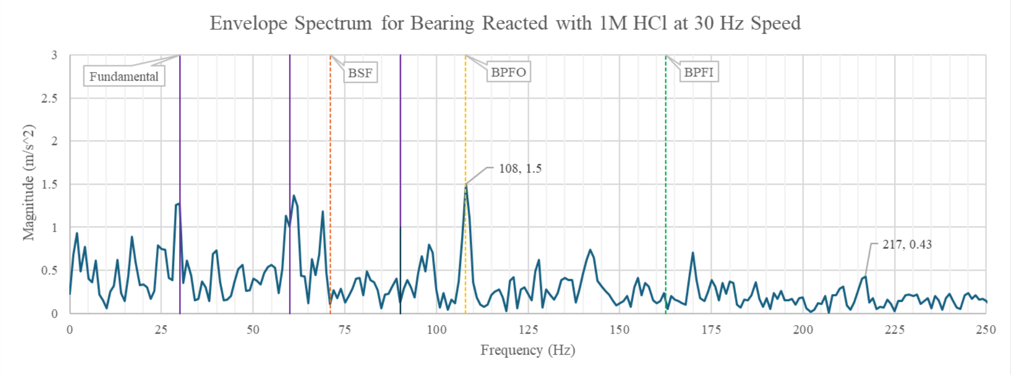

Figure 4.11: Envelope spectrum of 6002 bearing after reaction with 1M HCl at 30 Hz speed.

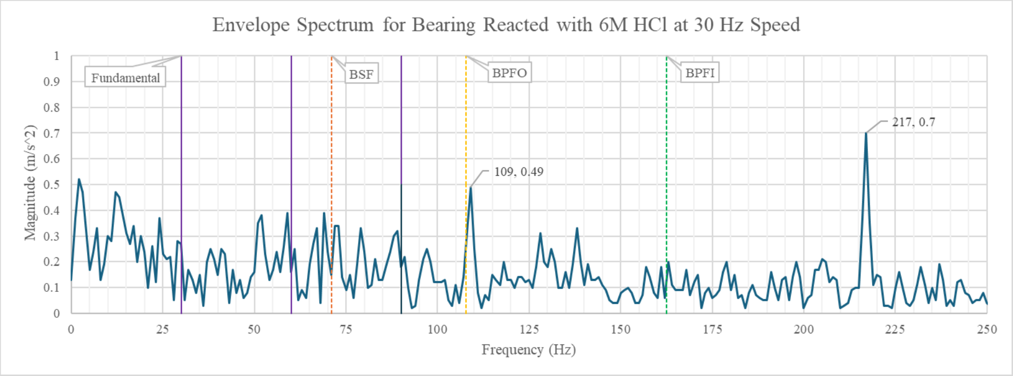

Figure 4.12: Envelope spectrum of 6002 bearing after reaction with 6M HCl at 30 Hz speed.

Figure 4.13 presents the envelope spectrum of a bearing contaminated with metal particles. Overall, no discernable peaks are observed compared to the noise level. The minor peaks present are not significant enough to indicate any fault. This is possibly because the bearing has not operated long enough for faults to develop due to the interaction between metal particles and the raceways. The occasional spikes in the acceleration waveform are caused by brief impacts when metal particles become trapped between the rolling elements and the raceways. However, since these collisions are inconsistent, they do not register as peaks in the envelope spectrum. Similarly, Figure 4.14 shows the envelope spectrum for a bearing contaminated with sand, which also does not contain any observable peaks. In summary, the envelope spectrum for particle-contaminated bearings shows no significant peaks, indicating no signs of fault formation.

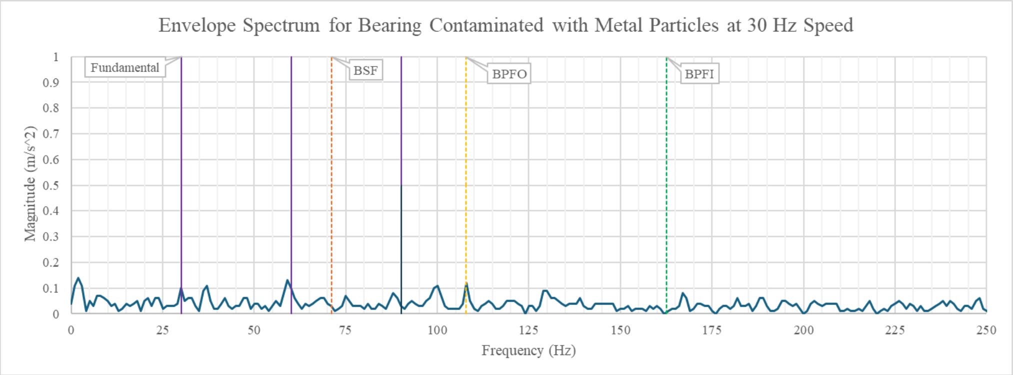

Figure 4.13: Envelope spectrum of 6002 bearing contaminated with metal particles at 30 Hz speed.

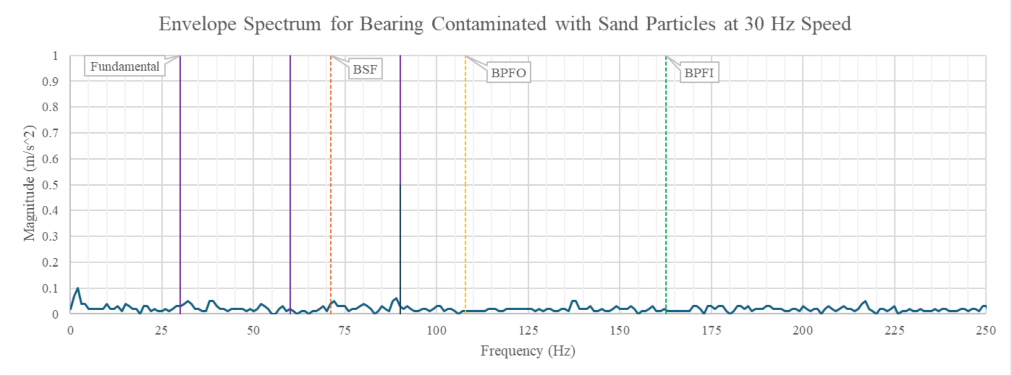

Figure 4.14: Envelope spectrum of 6002 bearing contaminated with sand particles at 30 Hz speed.

4.4 Vibration Indicators

In this subsection, the results for various vibration indicators will be presented and discussed. The respective formulas and units for each indicator are summarized in Table 4.4. Additionally, threshold levels will be defined for selected vibration indicators.

Table 4.4: Summary of vibration indicators with their respective formula and units.

Indicators	Formula	Units
K-factor	$a_{peak} \cdot a_{RMS}$	$(m/s^2)^2$
RMS acceleration	$\sqrt{\frac{\sum_{i=1}^{N}(a_i)^2}{N}}$	m/s^2
Peak acceleration	$\max(a_i)$	m/s^2
Peak-to-peak acceleration	$\max(a_i) - \min(a_i)$	m/s^2
Crest factor	$\frac{a_{peak}}{a_{RMS}}$	(dimensionless)
Kurtosis	$\sum_{n=1}^{N}\frac{[a(n)-\mu]^4}{N(\sigma^2)^2}$	(dimensionless)
RMS velocity	$\sqrt{\frac{\sum_{i=1}^{N}(v_i)^2}{N}}$	mm/s
P-P displacement	$\max(s_i) - \min(s_i)$	µm

RMS displacement	$\sqrt{\frac{\sum_{i=1}^{N}(s_i)^2}{N}}$	µm

4.4.1 K-factor

Based on Table 4.5, the K-factor for a healthy bearing ranges from 3.5 to 38.3, with the K-factor increasing proportionally with speed. With bearing is lacking lubrication, the metal-to-metal contact leads to a significant rise in the RMS vibration level, which causes a substantial increase in the average K-factor. For metal particle contamination at 30 Hz, the maximum K-factor reaches 1153, which is much higher than its relatively low average of 127.8. In comparison, sand-contaminated bearings exhibit an average K-factor of 901.6 at 30 Hz, which is significantly greater than that of metal contamination. A characteristic of contamination is that the maximum K-factor is often much higher than the average, which is true up to a factor of 10. All in all, at 30 Hz, the highest average K-factor is seen in bearing with outer race damage with magnitude of 1690.7. Meanwhile, the greatest maximum K-factor is observed in sand-contaminated bearing at a value of 8194.4.

To establish the threshold for the K-factor, the average amplitude and maximum amplitude are plotted to obtain an exponential curve fit, as shown in Figure 4.15. If a vibration measurement exceeds the average K-factor, it will be deemed “Caution.” If the maximum K-factor is exceeded, the bearing is considered in “Danger.” Based on this threshold, all of the defective bearings are categorized as faulty. Overall, the K-factor effectively combines the effects of RMS acceleration and peak acceleration. However, it is sensitive to speed, so the threshold needs to be continuously adapted to account for speed variations.

Table 4.5: K-factor for UC201 at motor side.

Bearing Condition	Speed	10 Hz	15 Hz	20 Hz	25 Hz	30 Hz
Healthy	Average	3.5	4.3	10.9	19.3	38.3
	Maximum	6.2	7.1	19.9	33.3	59.4
	Minimum	2.3	2.9	6.5	14.4	29.1
No Lubrication	Average	43.6	77.4	186.5	462.5	648.7
	Maximum	113.5	147.7	334.4	913.4	1154.7
	Minimum	22.5	53.5	111.4	242.8	462.4

Contamination (Metal)	Average	5.9	14.6	15.8	40.0	127.8
	Maximum	25.1	34.0	105.4	705.5	1153.0
	Minimum	3.8	10.0	10.8	16.3	32.0
Contamination (Sand)	Average	11.7	27.0	46.7	158.9	901.6
	Maximum	48.3	58.0	306.4	1508.6	8194.4
	Minimum	7.9	21.7	35.2	58.3	127.1
Outer Race Damage	Average	37.1	120.9	366.8	886.3	1690.7
	Maximum	58.7	348.2	429.9	1063.7	2219.1
	Minimum	28.3	86.0	321.2	751.5	1242.4
Corrosion (1M HCl)	Average	5.1	10.5	19.8	38.0	76.4
	Maximum	17.2	24.2	53.2	103.8	228.0
	Minimum	3.6	5.2	8.2	15.1	27.8
Corrosion (6M HCl)	Average	14.5	16.3	42.3	142.9	315.4
	Maximum	19.3	29.8	61.8	210.4	484.6
	Minimum	10.1	11.4	33.0	119.9	259.8

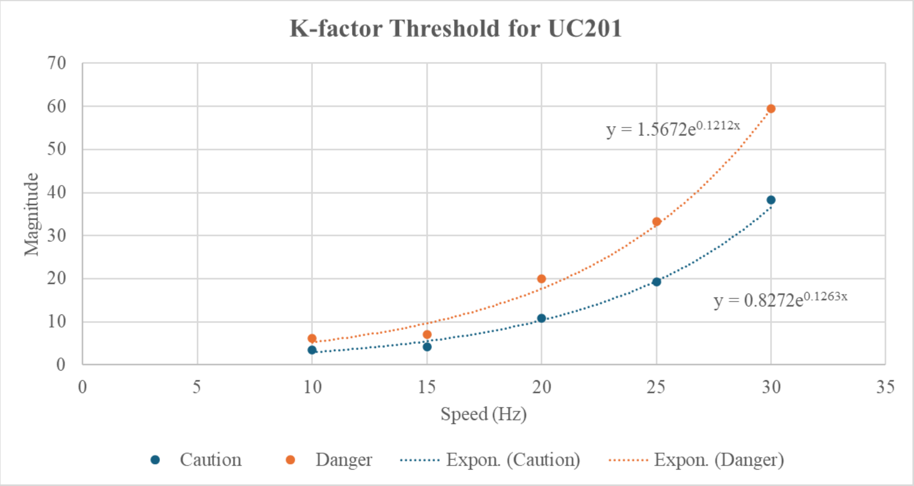

Figure 4.15: Threshold of K-factor for UC201.

4.4.2 RMS Acceleration

Similar to the K-factor, root mean square (RMS) acceleration is dependent on rotor speed. Figure 4.16 shows that bearings without lubrication experience higher RMS acceleration compared to corroded or contaminated bearings. This is possibly because degraded or contaminated grease still remains in those bearings, which provides a limited lubrication effect. In the case of sand contamination, the maximum RMS acceleration of 19.5 m/s^2 far exceeds the average of 7.5 m/s^2, indicating more variability in vibration levels. In contrast for outer race damage, while the average RMS acceleration is the highest at 14.3 m/s², the maximum value of 15.8 m/s² shows less deviation due to consistent impacts. For acid corrosion, higher concentrations lead to increased RMS acceleration levels. However, the RMS acceleration for the bearing exposed to 1M HCl is almost the same as that of a healthy bearing. This suggests that RMS acceleration alone may not be sufficient to diagnose faults effectively. Since the maximum RMS acceleration does not deviate significantly from the average, the threshold set using the maximum value is preferred in order to ensure a more conservative approach. The relationship between RMS acceleration and speed is illustrated by the equation in Figure 4.17.

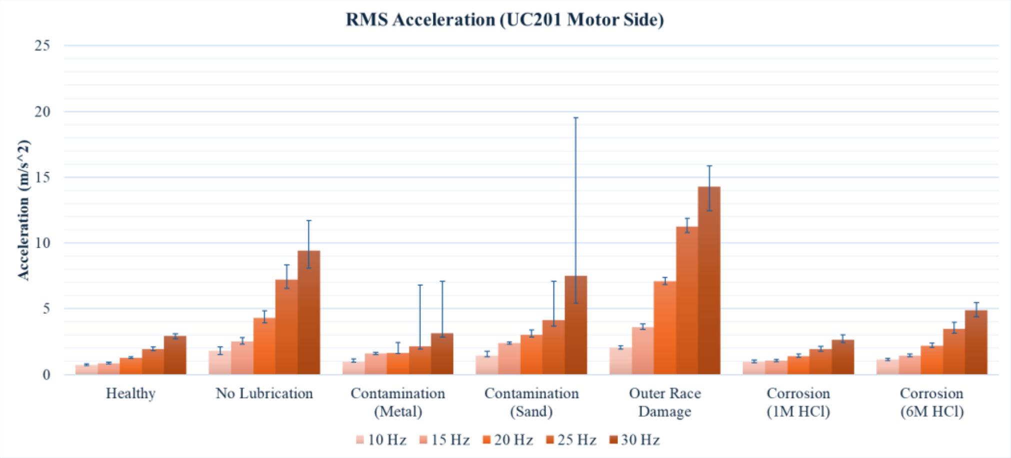

Figure 4.16: RMS acceleration for UC201 at motor side.

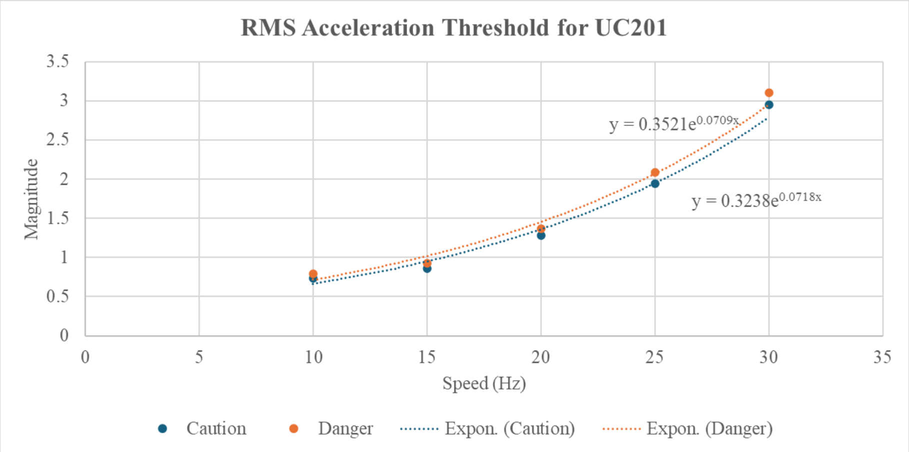

Figure 4.17: Threshold of RMS acceleration for UC201.

4.4.3 Peak Acceleration

For a healthy bearing, peak acceleration ranges from 4.7 m/s² to 13.0 m/s² as illustrated in Figure 4.18. In the case of no lubrication, peak acceleration increases up to 76.2 m/s² at a speed of 30 Hz, while having large variations in the data. Metal contamination exhibits relatively low peak acceleration values, but the maximum value spikes to 179.41 m/s² at 30 Hz. Sand contamination shows the largest variation among all defect types, with a maximum peak acceleration of 499.06 m/s² at 30 Hz. Bearings with outer race damage demonstrate the highest average peak acceleration at 118.08 m/s². However, the variation is not as large compared to contaminated bearings. For corrosion, the result is similar to RMS acceleration as bearings exposed to higher concentration of acid will exhibit greater peak acceleration. The threshold for peak acceleration is shown in Figure 4.19.

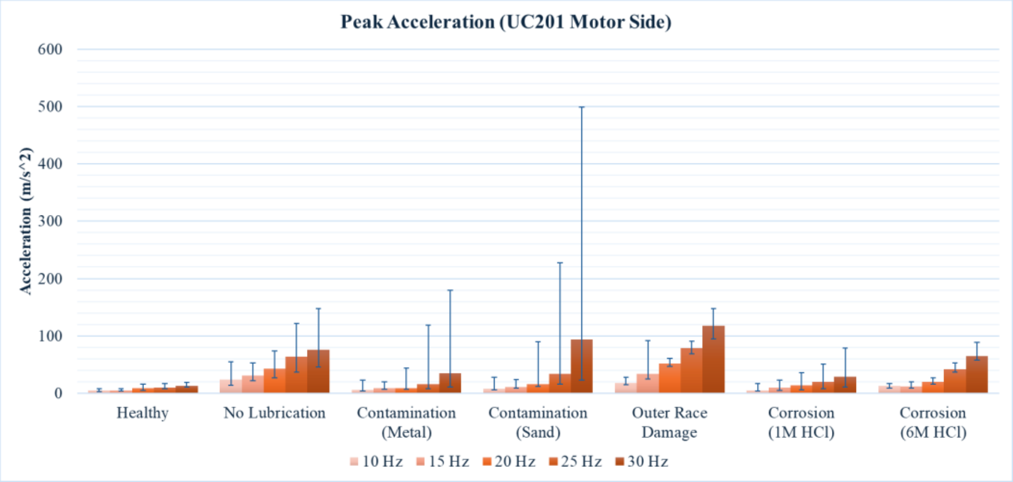

Figure 4.18: Peak acceleration for UC201 at motor side.

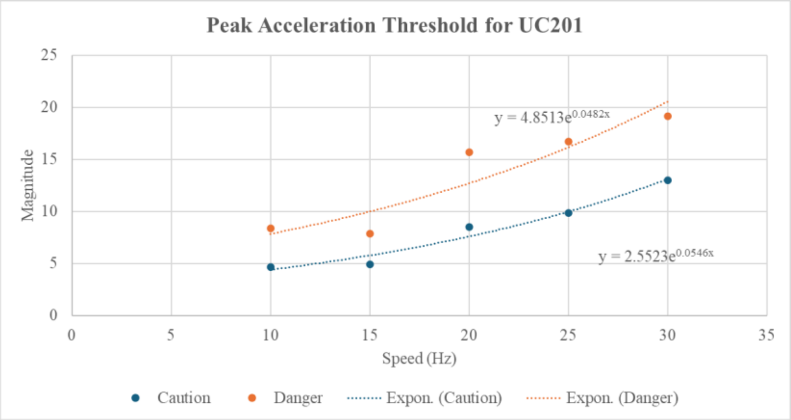

Figure 4.19: Threshold of peak acceleration for UC201.

4.4.4 Crest Factor

In literature, it was established that crest factor (CF) of less than 5 indicates the bearing is under normal operating conditions. In Figure 4.20, healthy bearings show a slight decreasing trend in crest factor as speed increases, ranging from 4.41 to 6.64, with an average of 5.65. In the study conducted by Kondhalkar and Diwakar (2019), it is reported that the crest factor in the radial direction is 4.55 for healthy ball bearing. The discrepancy may be due to differences in testing conditions such as bearing model, operating load, and speed.

For crest factor, the threshold is set at two standard deviations (2σ) above the mean, resulting in a threshold value of 7.49. Under no lubrication conditions, the crest factor is observed to decrease as speed increases. In non-lubricated bearing, the friction between components increases with speed. This results in a consistent and widespread increase in vibration level, which explains the significant rise in RMS levels. Since there is fewer transient impacts, the peak acceleration does not increase as much as the RMS level. This leads to a waveform with a high RMS level but less pronounced peaks, which causes the crest factor to decrease.

When comparing the average crest factors for each type of damage to the threshold, only particle-contaminated bearings do not exceed the threshold, mainly due to their relatively low crest factor at lower speeds. In particle-contaminated bearings, the crest factor increases slightly as speed rises. This is because peak acceleration rises more than the RMS value at higher speeds. As bearing speed increases, the energy of impacts between contaminants and bearing components rises. This causes the peak accelerations to be larger in the signal. Moreover, since the duration of each impact is shorter at high speeds, the impulses delivered by each impact significantly increase. This results in a more impulsive signal with sharper peaks. Lastly for bearings with outer race damage (average CF of 8.11) and 6M HCl corrosion (average CF of 10.7), the crest factor fluctuates around their respective means. Meanwhile, the 1M HCl shows an increasing trend in crest factor as speed increases.

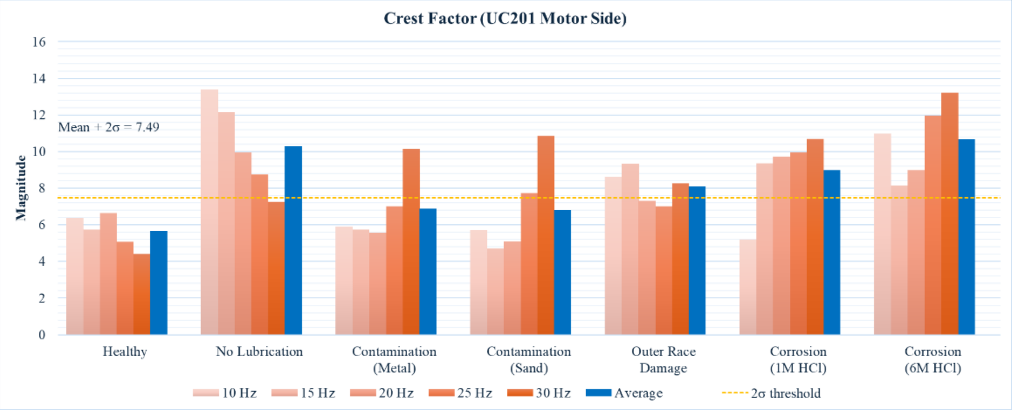

Figure 4.20: Crest factor for UC201 at motor side.

4.4.5 Kurtosis

Kurtosis is a measure of the tailedness of a signal relative to a normal distribution. Similar to the crest factor, it is proportional to the spikiness or impulsiveness of the vibration signal. In healthy bearings, the mean kurtosis is found to be 3.48, with a threshold level of 4.11 when using a 2σ criterion. The spread of kurtosis in healthy bearings is much smaller compared to damaged bearings. Similar to predictions in the literature, kurtosis measured in the experiment increases with speed for most damage types, except in the case of lack of lubrication. The kurtosis values for contaminated bearings exhibit significant variation due to the potential for vibration spikes caused by trapped particles. In Figure 4.21, the bearing exposed to 6M HCl shows the highest mean kurtosis at 20.50, while the sand-contaminated bearing records the highest maximum kurtosis at 145.5. For outer race damage, the kurtosis remains more consistent with an average of 11.6. However, for bearings without lubrication, kurtosis decreases from 14.22 to 5.45 as speed increases. At lower speeds, impacts due to friction are more irregular, resulting in more spikiness and higher kurtosis. As speed increases, vibrations become more consistent and less impulsive, which results in higher RMS values with relatively low peak magnitudes. Overall, the use of a 2σ threshold at 4.11 is acceptable for kurtosis. However, for a more conservative approach, the threshold could be set at 1σ or at the mean kurtosis value. According to study by Kulkarni and Bewoor (2016), the kurtosis value for a healthy bearing is close to 4. On the other hand, the kurtosis value ranges between 5 and 25 when defects are present on the inner or outer race. In summary, the findings regarding kurtosis are consistent with the existing research.

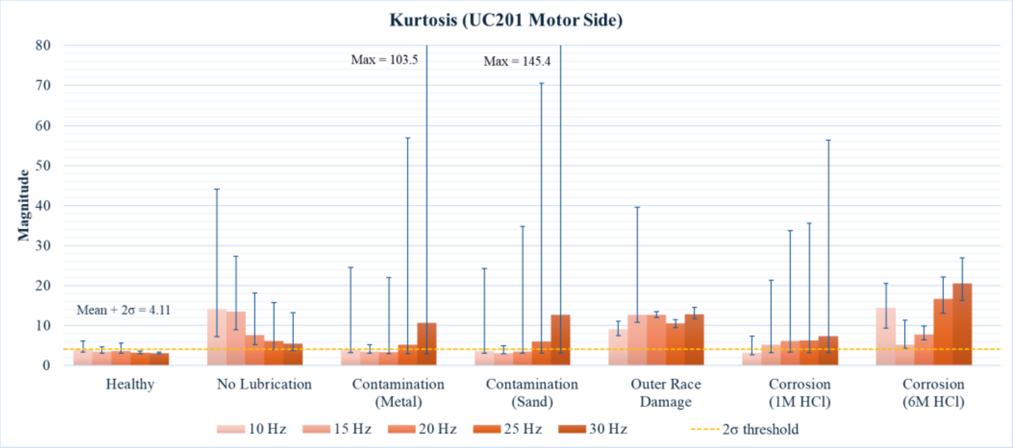

Figure 4.21: Kurtosis for UC201 at motor side.

4.4.6 Low-frequency Indicators

The analysis of RMS velocity, shown in Figure 4.22, reveals that the average RMS velocity for healthy bearings is 0.77 mm/s. However, defective bearings show little difference from this value. By using the 2σ threshold, it would result in misdiagnosis. This means it is an ineffective indicator for bearing diagnosis in this operating condition. Figure 4.23 displays RMS displacement which has an average value of 3.59 µm under healthy conditions. However, the values for other damage types do not deviate significantly from this mean, which also proves its ineffectiveness in detecting bearing faults. Peak-to-peak displacement has the average value of 19.35 µm for healthy bearings as shown in Figure 4.24. While outer race damage slightly exceeds this value, other damage types still remain below the mean.

The ineffectiveness of RMS velocity, RMS displacement, and peak-to-peak displacement as indicators can be attributed to several factors. First, low-frequency filtering may cause the DAQ to capture machinery faults rather than targeting bearing failures. This causes a lack of ability to differentiate between healthy and defective bearings. Additionally, mathematical integration is used to derive velocity and displacement from acceleration signal. This may introduce inaccuracies and error in the data. Instead, it may be more accurate to use sensors specifically designed to directly measure velocity and displacement.

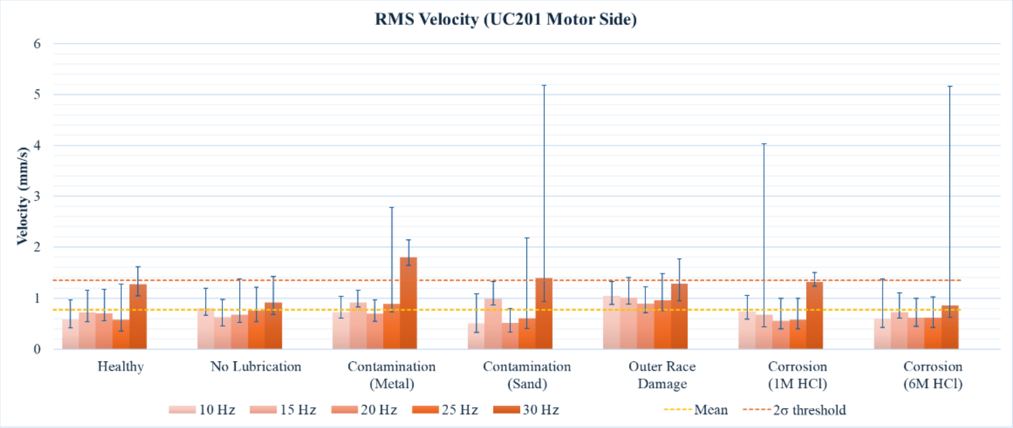

Figure 4.22: RMS velocity for UC201 at motor side.

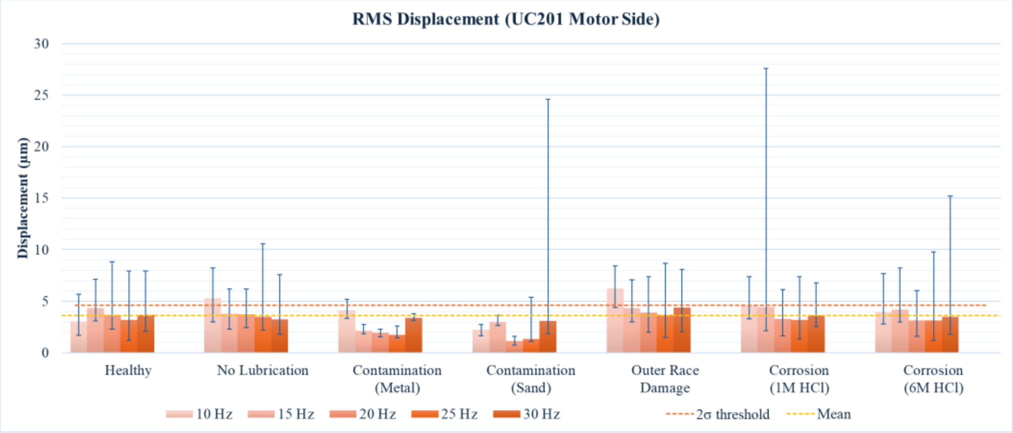

Figure 4.23: RMS displacement for UC201 at motor side.

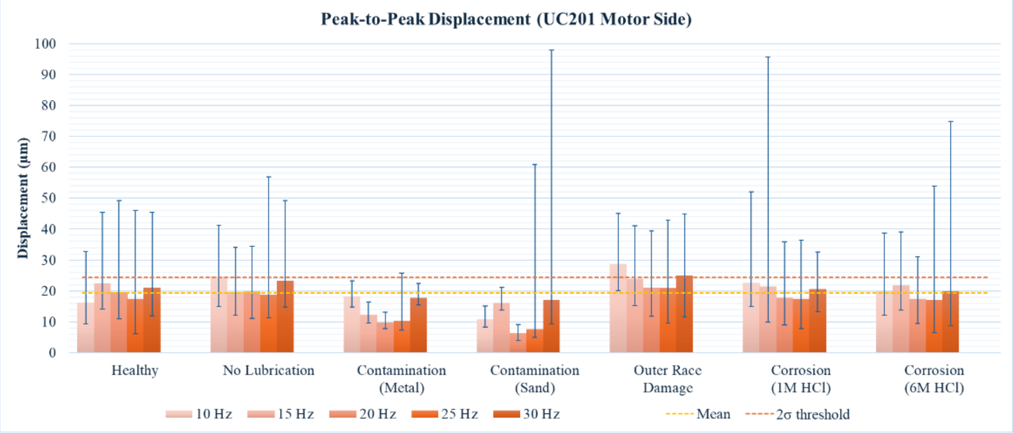

Figure 4.24: Peak-to-peak displacement for UC201 at motor side.

4.5 RUL Prediction

The RMS acceleration of a metal-contaminated UC201 bearing was monitored over an extended period, with the duration of each run presented in Table 4.6. The runs ranged from 39 to 384 minutes, with a cumulative duration of 1,323 minutes. Theoretically, the vibration level of a degrading bearing should follow an exponential curve, as illustrated in Figure 2.20. However, the experimental data followed a trend resembling a Power Law, with the equation of fit shown in Figure 4.25. In the first 100 minutes, the RMS acceleration increased rapidly from 2.8 m/s^2 to 7.5 m/s^2. After 100 minutes, the vibration level began to stabilize, exhibiting a gradual increase over time. The sudden drops in vibration level were observed due to the resting effect of the test rig. During extended operation, the components experienced increased temperatures and thermal stress, which reduced the performance of the bearing lubricant. Once the rig rested, the vibration levels decreased as the components returned to ambient temperature. To smooth transient deviations, a 60-minute moving average was applied to the RMS signal, as shown in Figure 4.26. To estimate the remaining useful life (RUL) of the bearing, the data points during the steady state were fitted with a linear trend. At the end of the experiment, the RMS acceleration hovered around 10 m/s^2. The linear fit equation predicted that, in order to reach a vibration level of 12 m/s^2, it would take approximately 5,867 minutes of cumulative run time.

Table 4.6: Duration of data collection for each run.

Run	**Duration (minutes)**
1	39
2	217
3	168
4	384
5	227
6	289
Total	1323

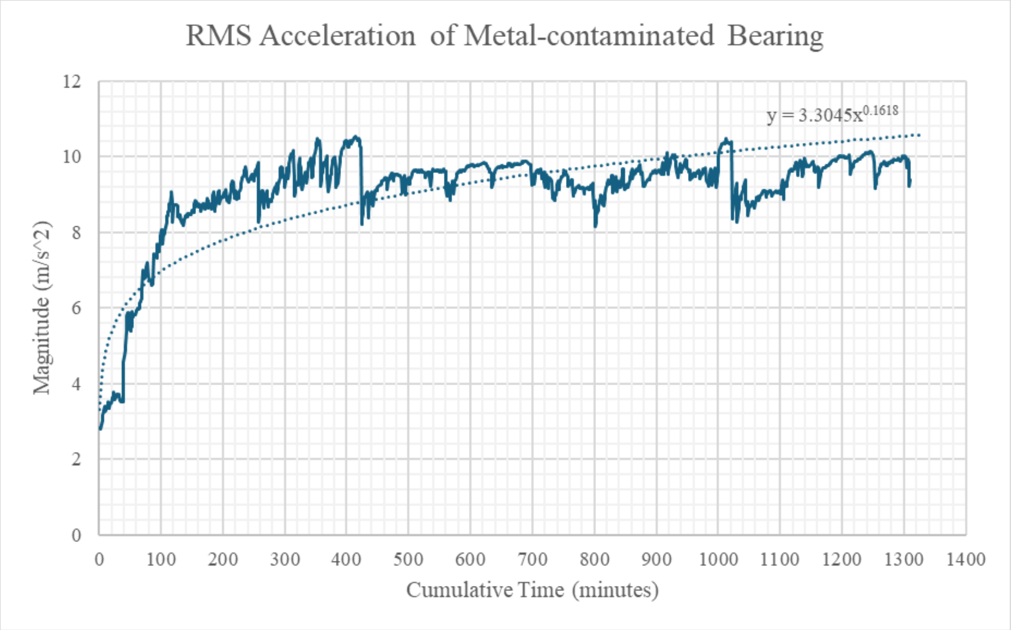

Figure 4.25: RMS acceleration of metal-contaminated bearing for cumulative duration of approximately 1300 minutes.

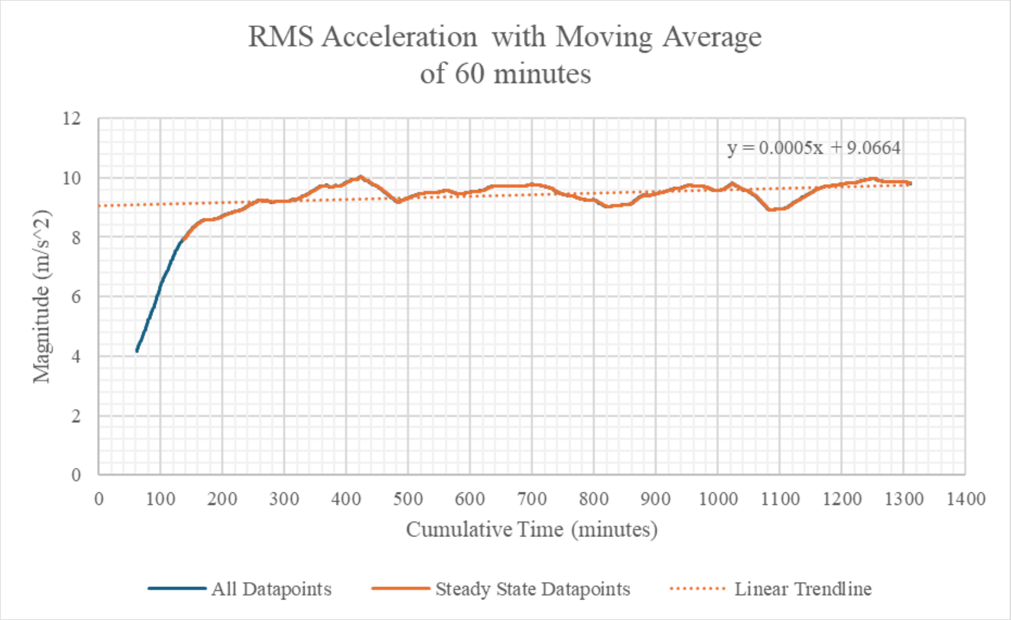

Figure 4.26: RMS acceleration with moving average period of 60 minutes.

4.6 Validation of Algorithm

Validation of the algorithm performed by disassembling bearings that exhibit significant peaks in the envelope spectrum to confirm the presence of any failures. Additionally, the validation process involves comparing the results of the algorithm with analysis data from the Dynamox IoT monitoring system by MITS Solution Asia.

4.6.1 Bearing Disassembly

Based on the analysis in Section 4.3, significant peaks were observed in the envelope spectrum of 6002 bearings treated with 1M and 6M HCl. According to the literature, when bearing steel reacts with acid, corrosion pits accompanied by dark discoloration develop. This is evident in Figure 4.27 (a), where a large patch of corrosion is seen on the outer race. As the bearing balls come into contact with these pits, vibrations at the BPFO frequency are generated. In Figure 4.27 (b), corrosion on the inner race is also observed. However, the envelope spectrum in Figure 4.11 does not show a significant peak at the BPFI frequency. Figure 4.28 illustrates the outer race of a bearing exposed to 6M HCl. The location of pitting seems to correspond with the spacing of the bearing balls. Notably, the inner race of this bearing showed minimal pitting.

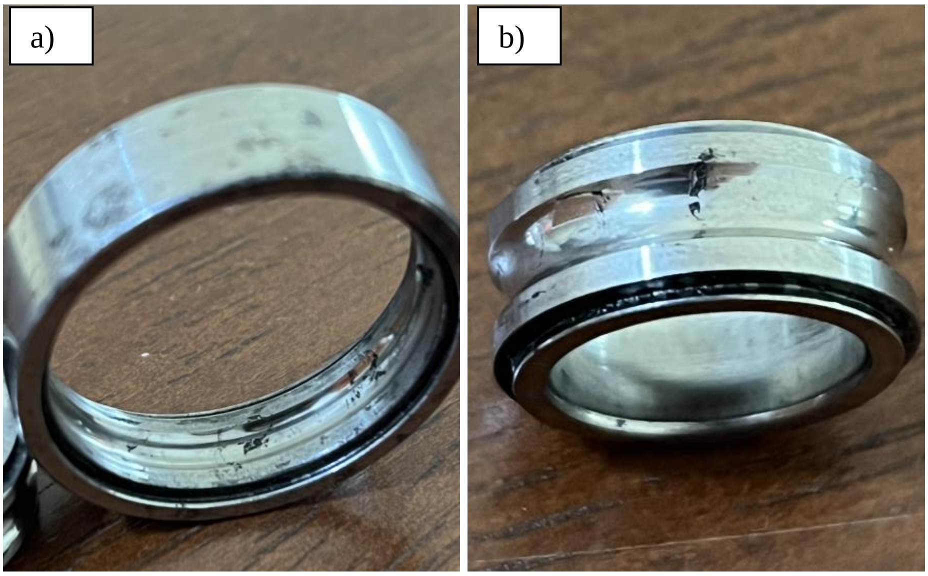

Figure 4.27: Photo of 6002 bearing exposed to 1M HCl: (a) outer race; (b) inner race.

Figure 4.28: Photo of outer race of 6002 bearing exposed to 6M HCl.

4.6.2 Comparison with Commercial System

MITS Solution Asia possesses a dedicated bearing vibration learning rig equipped with bearings that represent various fault conditions, as shown in Figure A-1. These include faults in the outer race, inner race, and bearing balls. Vibration data are collected using Dynamox wireless DynaLogger sensors, illustrated in Figure A-2. The sensors are MEMS-based and capable of capturing triaxial vibrations at a sampling rate of up to 13 kHz. The rig is also equipped with a digital tachometer, which allows for precise speed control during experiments. For validation, the same bearing was operated, and its vibrations were monitored using the algorithm developed in this study, followed by verification through the Dynamox system.

Overall, for detection of envelope spectrum, the algorithm is considered to be on par with the commercial system. Figure 4.29 shows the acceleration recorded for healthy condition bearing. The waveform is within expectation as it has a relatively low magnitude of 2 m/s^2 and limited spikes in the signal. In Figure 4.30, the algorithm detected a magnitude of around 0.1 m/s^2, which is approximately equivalent to 0.010 g (G-force). This is almost same to the envelope spectrum from Dynamox system shown in Figure 4.31, which detected a magnitude of around 0.005 g to 0.015 g. The peaks between these monitoring systems also overlap slightly, especially for peak at 16 Hz, 50 Hz and 125 Hz.

Figure 4.32 shows the acceleration recorded for a bearing with inner race damage. The waveform exhibits an increased magnitude of approximately 8 m/s², with periodic spikes in the signal reaching up to 30 m/s². The envelope spectra for the bearing with inner race damage are presented in Figures 4.33 4.34 for the algorithm and its benchmark, respectively. The algorithm detects a noise level of around 0.01 g, which is consistent with the observations from the Dynamox system. Both monitoring systems observed peaks at intervals of 25 Hz, which may correspond to the bearing’s BPFI and its harmonics. For the algorithm, the peak magnitude ranges from 0.04 to 0.08 m/s², while for Dynamox, the magnitude ranges from 0.05 to 0.10 m/s². This demonstrates that the algorithm's detection is fairly accurate in terms of both magnitude and spectral frequency.

In Figure 4.35 (a), it is observed that the RMS acceleration values are closest for inner race damage, with 3.35 m/s² detected by the algorithm and 4.16 m/s² by Dynamox. However, there is a significant discrepancy in detection for other types of damage. A similar observation is made for peak-to-peak acceleration shown in Figure 4.35 (b). For inner race damage, the algorithm detected 80.08 m/s², while Dynamox detected 69.26 m/s², which is relatively close. Figure 4.35 (c) shows crest factor which is able to produce similar indicator values for all damage types. The smallest discrepancy is found for healthy bearings (7.53 by the algorithm and 7.34 by Dynamox) and for bearing ball defects (4.42 by the algorithm and 4.31 by Dynamox). In terms of kurtosis shown in Figure 4.35 (d), the algorithm remains quite consistent with the benchmark. However, there is a large difference observed for inner cage damage, with a value of 13.5 by the algorithm compared to 5.76 by Dynamox. Lastly, Figure 4.35 (e) illustrates RMS velocity. The algorithm produced close results to the benchmark for most damage types, albeit for outer race damage. There is a significant difference for outer race damage as the algorithm measured a RMS velocity of 21.4 mm/s while Dynamox only measured 0.4 mm/s.

Table 4.7 presents error analysis by comparing the percentage difference between the vibration measurements obtained from the algorithm and the Dynamox system. A negative percentage indicates that the algorithm produced a lower magnitude than Dynamox, and a positive percentage means the algorithm's measurement was higher. Among the vibration indicators, crest factor is the most consistent with percentage difference between 2.63% and 65.19%. Among different bearing conditions, the percentage difference is smallest for the healthy bearing, ranging from 2.63% to 57.86%. For healthy bearings and bearings with inner faults, the results from both systems are relatively similar. However, for bearings with outer and ball faults, there is a notable inconsistency between the algorithm and Dynamox, resulting in large percentage differences.

The discrepancy in vibration measurements between the algorithm and the Dynamox system can be attributed to several factors. First, piezoelectric accelerometers are more sensitive to minor motions compared to MEMS accelerometers, as noted by Huang, Hsu, and Ahn (2022). This could explain why the majority of measurements from the algorithm are greater than those from the Dynamox system. Next, the piezoelectric accelerometer used in the algorithm has a higher acceleration limit of ±50 g, compared to ±16 g for MEMS-based systems like Dynamox. This allows the piezoelectric sensor to handle larger vibrations without saturation, resulting in more reliable measurements, especially for high-impact events. Furthermore, the acceleration impact limit of the Dynamox accelerometer may be a contributing factor. As the Dynamox system approaches its 10 g limit (98.1 m/s²) over 0.2 ms, it may produce inaccurate readings, particularly when measuring peak accelerations, as shown in Figure 4.35(b). Lastly, the number of samples taken by each system differs significantly. The algorithm captures data for 60 seconds, whereas the Dynamox system only records for 2.5 seconds before processing. This difference in sampling duration may also contribute to discrepancies in the data (Kistler Instrument Corporation, 2008; Dynamox, 2024).

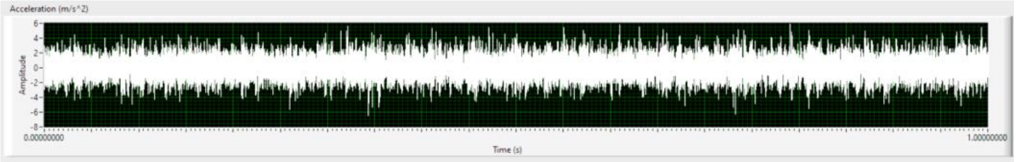

Figure 4.29: Acceleration waveform of healthy condition bearing, monitored by algorithm.

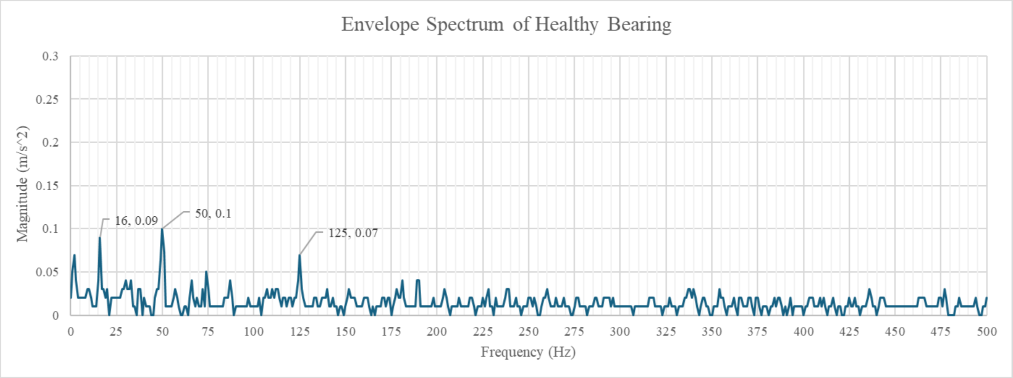

Figure 4.30: Envelope spectrum of healthy condition bearing, monitored by algorithm.

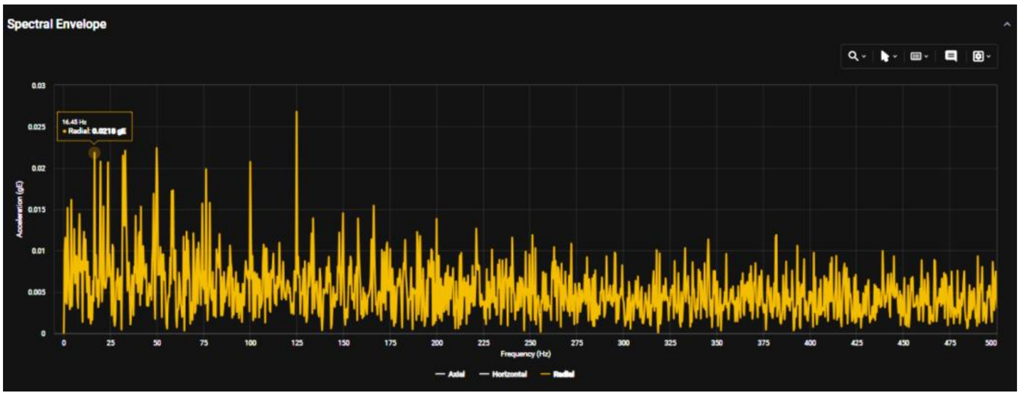

Figure 4.31: Envelope spectrum of healthy condition bearing, monitored by Dynamox system.

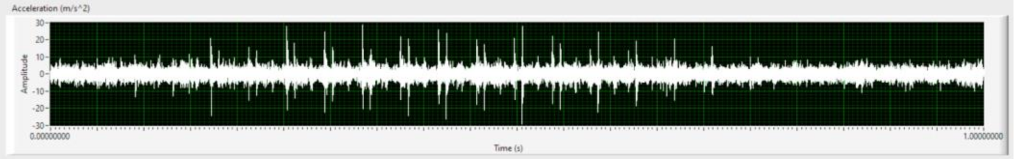

Figure 4.32: Acceleration waveform of bearing with inner race damage, monitored by algorithm.

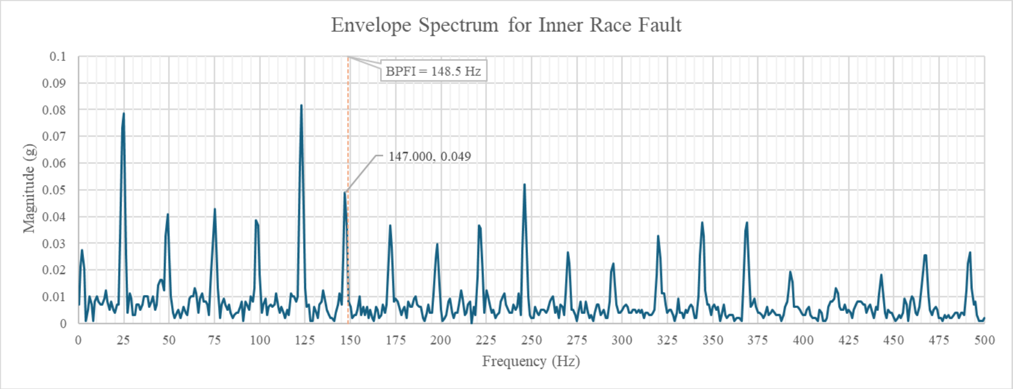

Figure 4.33: Envelope spectrum of bearing with inner race damage, monitored by algorithm.

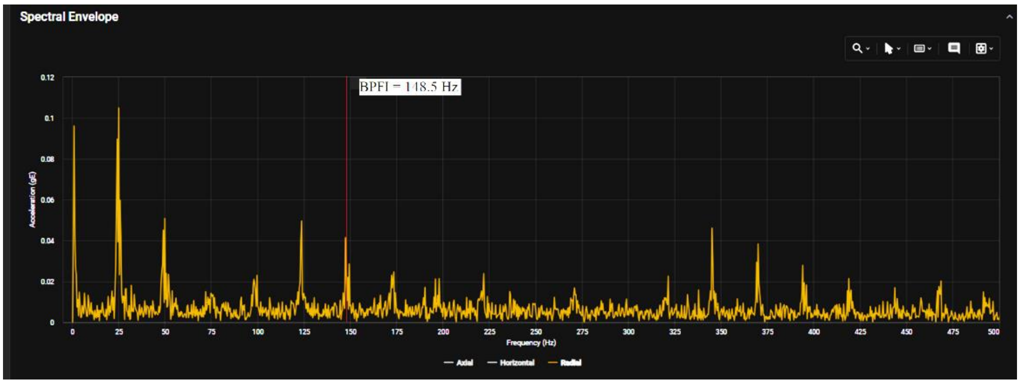

Figure 4.34: Envelope spectrum of bearing with inner race damage, monitored by Dynamox system.

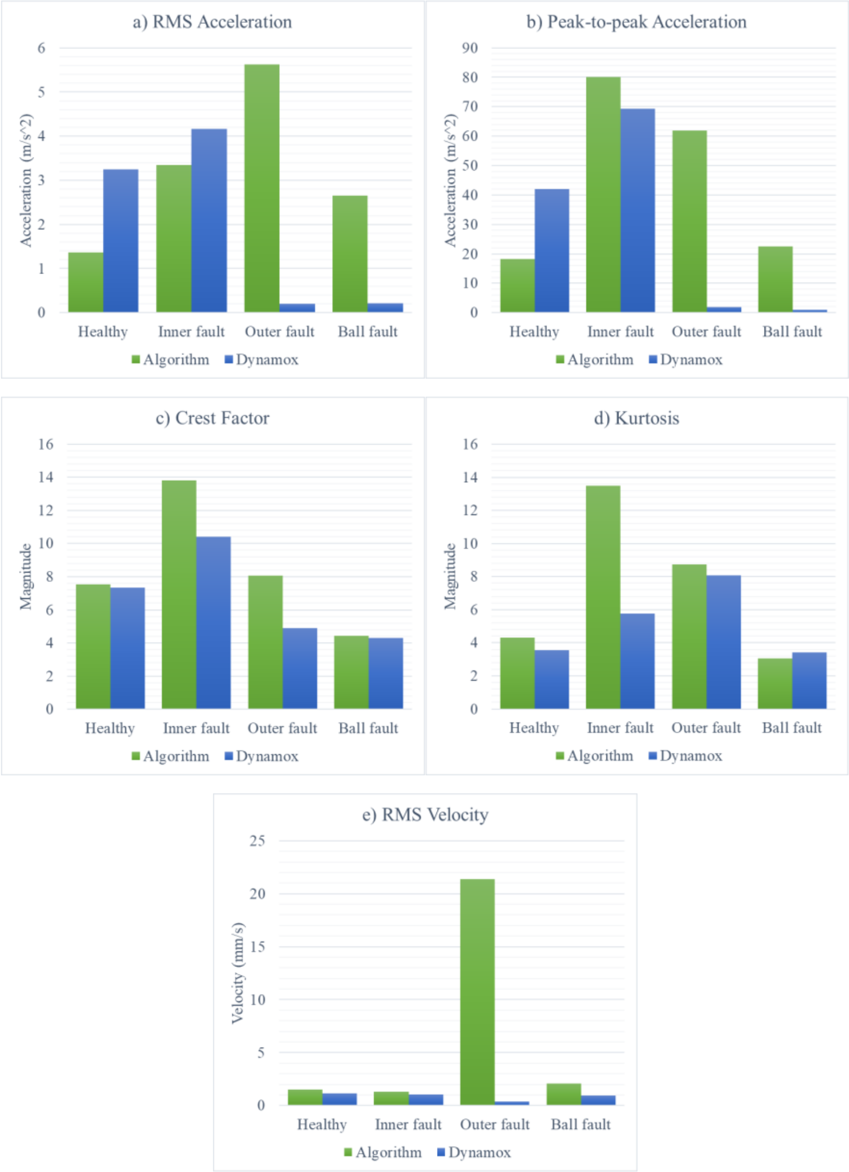

Figure 4.35: Graphical comparison of vibration indicators between algorithm and Dynamox monitoring system.

Table 4.7: Percentage difference of vibration indicators between algorithm and Dynamox monitoring system.

	Percentage Difference (%)			
Vibration Indicator	Healthy	Inner Fault	Outer Fault	Ball Fault
RMS Acceleration	-57.86	-19.52	2764.35	1136.26
Peak-to-peak Acceleration	-56.38	15.62	3228.00	2339.24
Crest Factor	2.63	32.66	65.19	2.66
Kurtosis	20.44	134.56	7.87	-10.62
RMS Velocity	28.83	25.33	5247.71	123.76

4.7 Summary

In summary, the acceleration waveform provides a direct visualization of vibration levels and can help identify periodic spikes and indicate localized defects. However, it is not practical for handling large amounts of vibration data. To address this, vibration indicators are more effective. The K-factor is sensitive to defects but requires constant adjustment on thresholds due to its sensitivity to speed. This limits its practical use. RMS acceleration is less sensitive to defects because the impact of sharp peaks is averaged out. This is evident by the misdiagnosis of the 1M HCl bearing, which indicates that RMS alone may not be sufficient for accurate fault detection. Crest factor is less affected by speed variations but it can be counterintuitive to interpret. This is because it tends to decrease in the presence of severe faults. Kurtosis, on the other hand, is a reliable indicator of signal spikiness and remains consistent across different damage types. Lastly, low-frequency indicators were found to be ineffective, as bearing resonance typically occurs at higher frequencies. All in all, the results produced by the algorithm were accurately confirmed through physical inspection of the disassembled bearings, along with validation from a commercial system. However, the results for RUL prediction were not ideal as the expected exponential trend was not fully achieved.

CHAPTER 5

CONCLUSIONS AND RECOMMENDATIONS

5.1 Conclusions

In this study, a signal processing algorithm had successfully been developed and tested under various operating conditions in real-time. The vibration patterns for different failure modes are also identified in the form of acceleration waveform and envelope spectrum. The accuracy of the algorithm was evaluated by comparing it to a commercial monitoring system. Among the vibration indicators, crest factor is identified as the most consistent with percentage difference between 2.63% and 65.19%. Additionally, the detection results were confirmed through physical inspection of the bearings which reveals pitting in bearing exposed to acidic solution. All in all, the objectives of the study were achieved.

It was observed that different failure modes exhibited distinct detection patterns in the vibration signals. For instance, outer race damage produced periodic spikes in the waveform and peaks at the BPFO frequency, while contamination resulted in occasional spikes in the indicator values but did not show any clear peak in the envelope spectrum. Bearings with lubrication issues showed high RMS values without localized faults in the envelope spectrum, while corrosion by acid produced a noisy envelope spectrum with peaks at fault frequencies and increased magnitude across indicators.

This study proved that envelope spectrum is a powerful tool for identifying bearing-specific frequencies. The study revealed that the percentage error for the BPFO varied between 0.31% and 1.24%, with magnitude ranging from 0.3 m/s^2 to 1.2 m/s^2 for bearings with outer race damage. On the other hand, corroded bearings exhibited a magnitude range of 0.4 m/s^2 to 1.5 m/s^2, which demonstrates the impact of corrosion on vibration levels.

In terms of vibration indicators, danger thresholds were established to evaluate bearing health. Specifically, a crest factor threshold of 7.49 and a kurtosis threshold of 4.11 were defined to indicate defective bearings. Other vibration indicators will be evaluated using equations that are dependent on rotational speed. Among the indicators, K-factor is most straightforward to interpret. However, it is highly sensitive to speed and difficult to threshold in variable-speed operations. RMS acceleration, on the other hand, only shows significant changes when the damage is severe. Next, crest factor cannot be solely relied on as it tends to decrease at severe fault stages. Kurtosis, which is very stable for healthy operation, can effectively detect signal spikiness and impulsiveness which makes it useful for early fault detection. Lastly, low-frequency indicators were found to be less effective at detecting bearing faults. The final proposed solution combines the use of RMS acceleration to monitor long-term increases in vibration levels along with kurtosis to detect abnormal spikes in the signal.

While the study did not contribute to an ideal method for predicting the remaining useful life of the bearings, it provided valuable insights into the vibration behaviour of bearings during extended operation. In conclusion, the findings in this study contribute to a deeper understanding on how vibration patterns evolve with bearing condition and how various indicators can be applied to monitor bearing health effectively.

5.2 Recommendations for Future Work

For future work, several recommendations can be made to improve the experimental setup and result accuracy. First, testing can be conducted on bearings with larger diameters to study the effect of bearing size. Larger bearings can support greater loads, which may provide a better understanding of failure modes under high load conditions. Additionally, they generally have a longer operational lifespan, which is beneficial for the study of long-term wear and degradation. Moreover, operating at a higher running speeds and heavier loads will help to simulate more realistic operational conditions. Additionally, using damaged bearings from actual operations in manufacturing plants would provide more accurate findings into actual failure modes.

In terms of the experimental setup, it is recommended to incorporate more sensors. Sensors can be installed in horizontal or axial directions. Additionally, three-axis sensors can be utilized to capture vibration data with greater details. Exploring the use of wireless sensors could also be beneficial as they would be easier to integrate into a cloud processing platform for real-time monitoring. For envelope spectrum analysis, future work may focus on exploring the development of inner race and ball faults to identify these specific fault frequencies. Furthermore, applying denoising techniques to the envelope spectrum will increase the signal-to-noise ratio which will enhance its reliability.

Lastly, for future work in the prediction of remaining useful life, it is suggested to use overloading or overspeeding on healthy bearings rather than inducing artificial damage. This approach could provide more realistic data on the gradual degradation of bearings over time. Additionally, the vibration monitoring should be conducted for a longer period of time, possibly in the region of hundreds of hours. This allows for more accurate RUL predictions and contributes to the development of RUL prediction models.

REFERENCES

Aherwar, A. and Khalid, S., 2012. Vibration analysis techniques for gearbox diagnostic: A review. *International Journal of Advanced Engineering Technology*, 3(2).

Ahmadi, H., Subchan, M., Rachmanita, R.E., Audora, R.D. and Wibuana, A., 2020. Vibration analysis of Kartini reactor secondary cooling pump using FFT analyzer. *Journal of Physics Conference,* 1511(1). http://dx.doi.org/10.1088/1742-6596/1511/1/012080.

Al-Badour, F., Sunar, M. and Cheded, L., 2011. Vibration analysis of rotating machinery using time–frequency analysis and wavelet techniques. *Mechanical systems and signal processing*, 25(6), pp.2083–2101. https://doi.org/10.1016/j.ymssp.2011.01.017.

Almeida, F.R. and Almeida, M.T., 2005. Statistical Analysis of Vibration Signals for Condition Monitoring of Defects in Rolling Element Bearings. In: *18th International Congress of Mechanical Engineering*. Brazilian Society of Mechanical Sciences and Engineering.

Borghesani, P., Ricci, R., Chatterton, S. and Pennacchi, P., 2013. A new procedure for using envelope analysis for rolling element bearing diagnostics in variable operating conditions. *Mechanical Systems and Signal Processing*, 38(1), pp.23–35. https://doi.org/10.1016/j.ymssp.2012.09.014.

Boudinar, A.H., Aimer, A.F., Khodja, M.E.A.K. and Benouzza, N., 2019. Induction motor’s bearing fault diagnosis using an improved short time Fourier transform. *Springer Nature Switzerland AG*, 522, pp.411–426. https://doi.org/10.1007/978-3-319-97816-1_31.

Dolenc, B., Boškoski, P. and Juričić, Đ., 2016. Distributed bearing fault diagnosis based on vibration analysis. *Mechanical systems and signal processing*, 66-67, pp.521–532. https://doi.org/10.1016/j.ymssp.2015.06.007.

Dron, J.P., Bolaers, F. and Rasolofondraibe, l., 2004. Improvement of the sensitivity of the scalar indicators (crest factor, kurtosis) using a de-noising method by spectral subtraction: Application to the detection of defects in ball bearings. *Journal of sound and vibration*, 270(1-2), pp.61–73. https://doi.org/10.1016/s0022-460x(03)00483-8.

Dyer, D. and Stewart, R.M., 1978. Detection of rolling element bearing damage by statistical vibration analysis. *Journal of mechanical design*, 100(2), pp.229–235. https://doi.org/10.1115/1.3453905.

Dynamox, 2024. *DynaLogger HF+ / HF+S*. [online] Available at: <https://content.support.dynamox.net/wp-content/uploads/2024/06/DataSheet-HF-062024-04-EN.pdf> [Accessed 6 October 2024].

El-Thalji, I. and Jantunen, E., 2015. A summary of fault modelling and predictive health monitoring of rolling element bearings. *Mechanical Systems* *and Signal Processing*, 60-61, pp.252–272. https://doi.org/10.1016/j.ymssp.2015.02.008.

Fahy, K. and Pérez, E., 1993. *Fast Fourier Transforms and Power Spectra in LabVIEW*. [online] Available at: <https://citeseerx.ist.psu.edu/document?repid=rep1&type=pdf&doi=bc5ffe63a26521370d72cbff5ec48aed4791601f> [Accessed 14 September 2024].

Feng, G.-J., Gu, J., Zhen, D., Aliwan, M., Gu, F.-S. and Ball, A.D., 2015. Implementation of envelope analysis on a wireless condition monitoring system for bearing fault diagnosis. *International Journal of Automation and Computing*, 12(1), pp.14–24. https://doi.org/10.1007/s11633-014-0862-x.

Filippenko, A., Brown, S. and Neal, A., 1999. *Vibration analysis for predictive maintenance of rotating machines*. [online] Available at: <https://patents.google.com/patent/US6370957B1/en> [Accessed 17 September 2024].

Gatzke, K.G. and Sobon, C.A., 2000. *US6448209B1 - Brake cleaner compositions comprising methyl acetate and acetone and method of using same.* [online] Google Patents. Available at: <https://patents.google.com/patent/US6448209B1/en> [Accessed 9 September 2024].

Goepfert, O., Ampuero, J., Pahud, P. and Boving, H.J., 2008. Surface roughness evolution of ball bearing components. *Tribology Transactions*, 43(2), pp.275–280. https://doi.org/10.1080/10402000008982340.

Hsu, C.-W., Chang, C.-C. and Lin, C.-J., 2016. *A Practical Guide to Support Vector Classification*. [online] Taipei, Taiwan. Available at: <https://www.csie.ntu.edu.tw/~cjlin/papers/guide/guide.pdf>.

Huang, H.-P., Hsu, F. and Ahn, A., 2022. *MEMS vs. Piezoelectric Accelerometer*. [online] Labfront. Available at: <https://www.labfront.com/article/mems-vs-piezoelectric-accelerometer> [Accessed 7 October 2024].

International Organization for Standardization, 2017. *ISO 15243:2017*. [online] *ISO*. Available at: <https://www.iso.org/standard/59619.html> [Accessed 28 April 2024].

International Organization for Standardization, 2022. *ISO 20816-3:2022*. [online] *ISO*. Available at: <https://www.iso.org/standard/78311.html> [Accessed 28 April 2024].

Jang, G. and Jeong, S.-W., 2004. Vibration analysis of a rotating system due to the effect of ball bearing waviness. *Journal of Sound and Vibration*, 269(3-5), pp.709–726. https://doi.org/10.1016/s0022-460x(03)00127-5.

Kim, H.-E., Tan, A.C.C., Mathew, J. and Choi, B.-K., 2012. Bearing fault prognosis based on health state probability estimation. *Expert Systems with*

Applications, 39(5), pp.5200–5213. https://doi.org/10.1016/j.eswa.2011.11.019.

Kim, H.-Y., 2013. Statistical notes for clinical researchers: assessing normal distribution (2) using skewness and kurtosis. *Restorative Dentistry & Endodontics*, 38(1), pp.52–54. https://doi.org/10.5395/rde.2013.38.1.52.

Kistler Instrument Corporation, 2008. *K-Shear Accelerometers*. [online] Available at: <https://intertechnology.com/Kistler/pdfs/Accelerometer_Model_8702B_8704B.pdf> [Accessed 13 September 2024].

Kondhalkar, G.E. and Diwakar, G., 2019. Crest factor measurement by experimental vibration analysis for preventive maintenance of bearing. *Springer eBooks*, pp.133–138. https://doi.org/10.1007/978-981-13-8507-0_21.

Kulkarni, S. and Bewoor, A., 2016. Vibration based condition assessment of ball bearing with distributed defects. *Journal of Measurements in Engineering*, 4(2), pp.43–121.

Lee, J.-Y., 2013. Variable short-time Fourier transform for vibration signals with transients - June-Yule Lee, 2015. *Journal of Vibration and Control*, 0(0), pp.1–15. https://doi.org/10.1177/1077546313499389.

Liu, H., Mo, Z., Zhang, H., Zeng, X., Wang, J. and Miao, Q., 2018. Investigation on rolling bearing remaining useful life prediction: A review. In: *Prognostics and System Health Management Conference*. IEEE. https://doi.org/10.1109/phm-chongqing.2018.00175.

Lord, D., Qin, X. and Geedipally, S.R., 2021. Exploratory analyses of safety data. *Elsevier eBooks*, pp.135–177. https://doi.org/10.1016/b978-0-12-816818-9.00015-9.

Malla, C. and Panigrahi, I., 2019. Review of condition monitoring of rolling element bearing using vibration analysis and other techniques. *Journal of Vibration Engineering & Technologies*, 7(4), pp.407–414. https://doi.org/10.1007/s42417-019-00119-y.

Mateo, C. and Talavera, J.A., 2018. Short-time Fourier transform with the window size fixed in the frequency domain. *Digital Signal Processing*, 77, pp.13–21. https://doi.org/10.1016/j.dsp.2017.11.003.

Mathew, J. and Alfredson, R.J., 1984. The condition monitoring of rolling element bearings using vibration analysis. *Journal of Vibration and Acoustics*, 106(3), pp.447–453. https://doi.org/10.1115/1.3269216.

McInerny, S.A. and Dai, Y., 2003. Basic vibration signal processing for bearing fault detection. *IEEE Transactions on Education*, 46(1), pp.149–156. https://doi.org/10.1109/te.2002.808234.

Muniyappa, A. and Praveen Krishna, I.R., 2019. Experimental Investigations to Assess Surface Contact Fatigue Faults in the Rolling Contact Bearings by

Enhancement of Sound and Vibration Signals. *Journal of Nondestructive Evaluation*, 38(1). https://doi.org/10.1007/s10921-019-0571-z.

National Instruments, 2024. *NI-9234 Specification*. [online] Available at: <https://www.ni.com/docs/en-US/bundle/ni-9234-specs/page/specs.html> [Accessed 13 September 2024].

Neisi, N., Sikanen, E., Heikkinen, J.E. and Sopanen, J., 2018. Effect of off-sized balls on contact stresses in a touchdown bearing. *Tribology International*, 120, pp.340–349. https://doi.org/10.1016/j.triboint.2017.12.036.

Oakland, J.S., 2007. *Statistical Process Control*. 6th ed. *Routledge eBooks*, London . pp.105–112. https://doi.org/10.4324/9780080551739.

Pachaud, C., Salvetat, R. and Fray, C., 1997. Crest factor and kurtosis contributions to identify defects inducing periodical impulsive forces. *Mechanical Systems and Signal Processing*, 11(6), pp.903–916. https://doi.org/10.1006/mssp.1997.0115.

Patel, V.N., Tandon, N. and Pandey, R.K., 2012. Defect detection in deep groove ball bearing in presence of external vibration using envelope analysis and Duffing oscillator. *Measurement*, 45(5), pp.960–970. https://doi.org/10.1016/j.measurement.2012.01.047.

Patidar, S. and Soni, P.K., 2013. An overview on vibration analysis techniques for the diagnosis of rolling element bearing faults. *International Journal of Engineering Trends and Technology*, 4(5).

Peng, B., Bi, Y., Xue, B., Zhang, M. and Wan, S., 2022. A survey on fault diagnosis of rolling bearings. *Algorithms*, 15(10), pp.347–347. https://doi.org/10.3390/a15100347.

Prudhom, A., Antonino-Daviu, J., Razik, H. and Climente-Alarcon, V., 2017. Time-frequency vibration analysis for the detection of motor damages caused by bearing currents. *Mechanical Systems and Signal Processing*, 84, pp.747–762. https://doi.org/10.1016/j.ymssp.2015.12.008.

Raje, N. and Sadeghi, F., 2009. Statistical numerical modelling of sub-surface initiated spalling in bearing contacts. *Proceedings of the Institution of Mechanical Engineers, Part J: Journal of Engineering Tribology*, 223(6), pp.849–858. https://doi.org/10.1243/13506501JET481.

Randall, R.B. and Sawalhi, N., 2011. A new method for separating discrete components from a signal. *Sound & Vibration*, 45(5), pp.6–9.

Renaudin, L., Bonnardot, F., Musy, O., Doray, J.B. and Rémond, D., 2010. Natural roller bearing fault detection by angular measurement of true instantaneous angular speed. *Mechanical Systems and Signal Processing*, 24(7), pp.1998–2011. https://doi.org/10.1016/j.ymssp.2010.05.005.

Rocchi, M., Mosciaro, F., Grottesi, F., Scortichini, M., Giantomassi, A., Pirro, M., Grisostomi, M. and Ippoliti, G., 2014. Fault prognosis for rotating electrical machines monitoring using recursive least square. In: *Proceedings of the 6th European Embedded Design in Education and Research, 2014*. https://doi.org/10.1109/ederc.2014.6924402.

Saidy, C., Xia, K., Kircaliali, A., Harik, R. and Bayoumi, A., 2020. The application of statistical quality control methods in predictive maintenance 4.0: An unconventional use of statistical process control (SPC) charts in health monitoring and predictive analytics. *Advances in Asset Management and Condition Monitoring*, pp.1051–1061. https://doi.org/10.1007/978-3-030-57745-2_87.

Salles , R.S., Almeida, G.C.S., Silva, L.R.M., Duque, C.A. and Ribeiro, P.F., 2020. Visualization of quality performance parameters using wavelet scalograms images for power systems. https://doi.org/10.48011//asba.v2i1.1497.

Selcuk, S., 2016. Predictive maintenance, its implementation and latest trends. *Journal of Engineering Manufacture*, 231(9), pp.1–10. https://doi.org/10.1177/0954405415601640.

Sikora, E.A., 2015. Detection of bearing damage by statistic vibration analysis (Diagnosis using the excess, the concept of crest factor). In: International Conference on Mechanical Engineering, Automation and Control Systems. https://doi.org/10.1109/meacs.2015.7414970.

Tse, P.W., Peng, Y.H. and Yam, R., 2001. Wavelet analysis and envelope detection for rolling element bearing fault diagnosis—their effectiveness and flexibilities. *Journal of Vibration and Acoustics*, 123(3), pp.303–310. https://doi.org/10.1115/1.1379745.

Upadhyay, S.H., Harsha, S.P. and Jain, S.C., 2009. Vibration signature analysis of high-speed unbalanced rotors supported by rolling-element bearings due to off-sized rolling elements. *International Journal of Acoustics and Vibration*, 14(3), pp.163–171. https://doi.org/10.20855//ijav.2009.14.3247.

Wang, J., Cui, L., Wang, H. and Chen, P., 2013. Improved Complexity Based on Time-Frequency Analysis in Bearing Quantitative Diagnosis. *Advances in Mechanical Engineering*. https://doi.org/10.1155/2013/258506.

Wang, W. and Zhang , W., 2008. Early defect identification: Application of statistical process control methods. *Journal of Quality in Maintenance Engineering,* 14(3), pp.225–236. https://doi.org/10.1108//jqme.

Xiang, J., Zhong, Y. and Gao, H., 2015. Rolling element bearing fault detection using PPCA and spectral kurtosis. *Measurement*, 75, pp.180–191. https://doi.org/10.1016/j.measurement.2015.07.045.

Xie, H., Fu, W., Jiang, L. and Bie, Z., 2022. Resilience assessment for natural gas systems and electrical power systems without complete integration. *IET Generation, Transmission & Distribution*, 16(24), pp.4893–4913.

https://doi.org/10.1049/gtd2.12629.

Yang, I-Tung. and Prayogo, H., 2022. Efficient reliability analysis of structures using symbiotic organisms search-based active learning support vector machine. *Buildings*, 12(455). https://doi.org/10.3390//buildings12040455.

Zheng, J., Xiang, D., Li, H. and Quach, D.-C., 2021. An Investigation into the Effect of Bearing Grease Degradation on the High-frequency dv/dt Bearing Current in an Inverter-fed Motor System. *6th International Conference on Power and Renewable Energy*. https://doi.org/10.1109/ICPRE52634.2021.9635227.

Zonta, T., Costa, C.A., Righi, R.R., Lima, M.J., Trindade, E.S. and Li , G.P., 2020. Predictive maintenance in the Industry 4.0: A systematic literature review. *Computers & Industrial Engineering*, 150. https://doi.org/10.1016/j.cie.2020.106889.

APPENDICES

Appendix A: Figures

Figure A-1: DynaLogger HF+ IoT Sensor from MITS Solutions Asia.

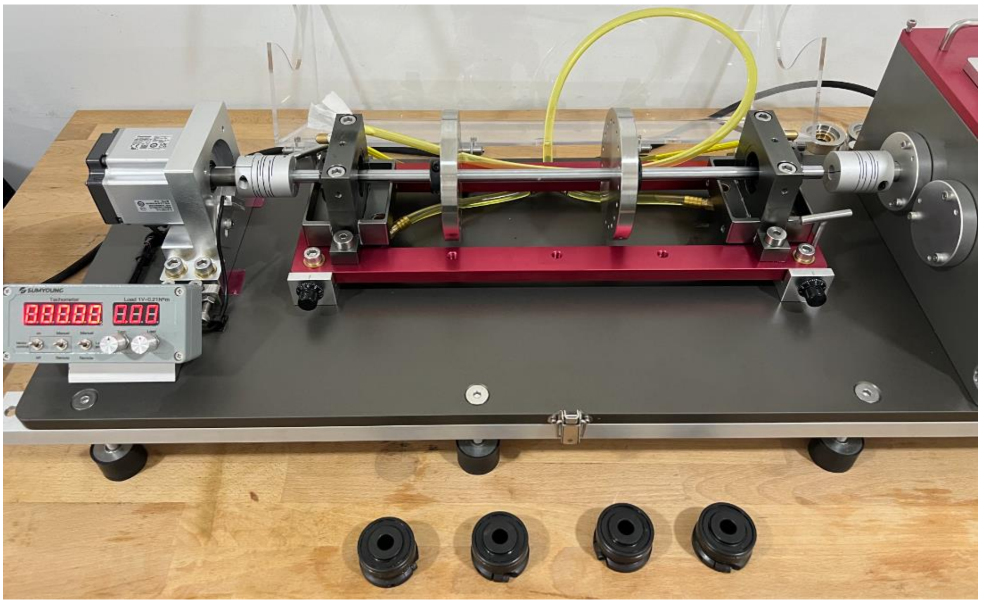

Figure A-2: Bearing vibration learning rig by Dynamox.

Appendix B: Gantt Chart

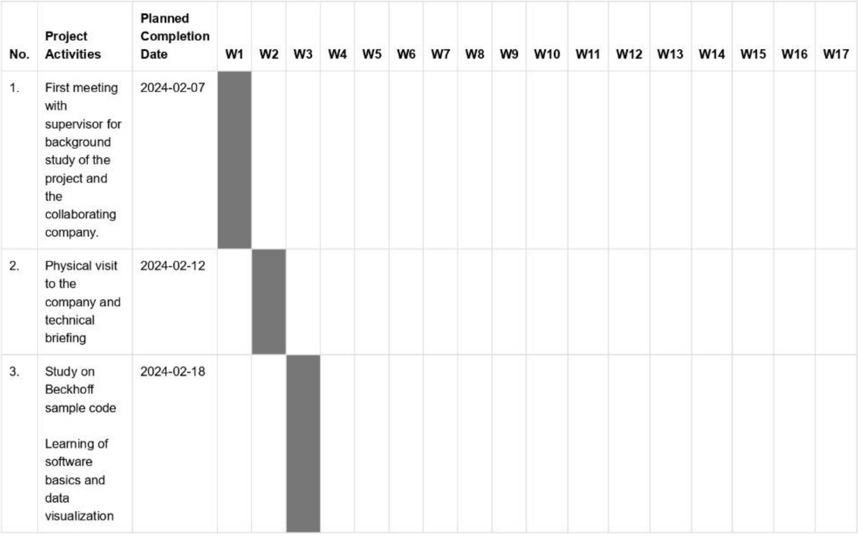

No.	Project Activities	Planned Completion Date	W1	W2	W3	W4	W5	W6	W7	W8	W9	W10	W11	W12	W13	W14	W15	W16	W17
1.	First meeting with supervisor for background study of the project and the collaborating company.	2024-02-07	■																
2.	Physical visit to the company and technical briefing	2024-02-12		■															
3.	Study on Beckhoff sample code Learning of software basics and data visualization	2024-02-18			■														

Graph B-1: Gantt Chart of Final Year Project 1.

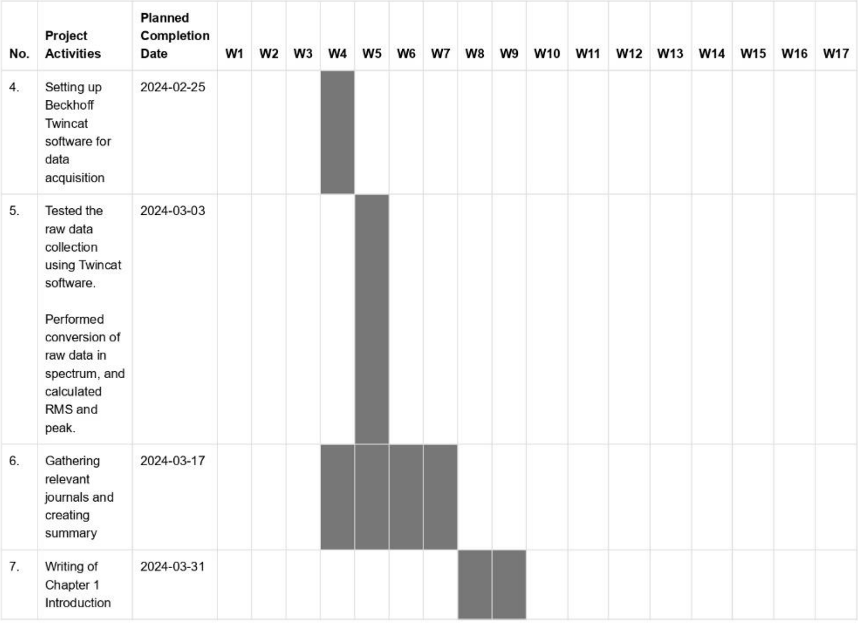

No.	Project Activities	Planned Completion Date	W1	W2	W3	W4	W5	W6	W7	W8	W9	W10	W11	W12	W13	W14	W15	W16	W17
4.	Setting up Beckhoff Twincat software for data acquisition	2024-02-25				■													
5.	Tested the raw data collection using Twincat software. Performed conversion of raw data in spectrum, and calculated RMS and peak.	2024-03-03					■												
6.	Gathering relevant journals and creating summary	2024-03-17				■	■	■	■										
7.	Writing of Chapter 1 Introduction	2024-03-31								■	■								

Graph B-2: Gantt Chart of Final Year Project 1.

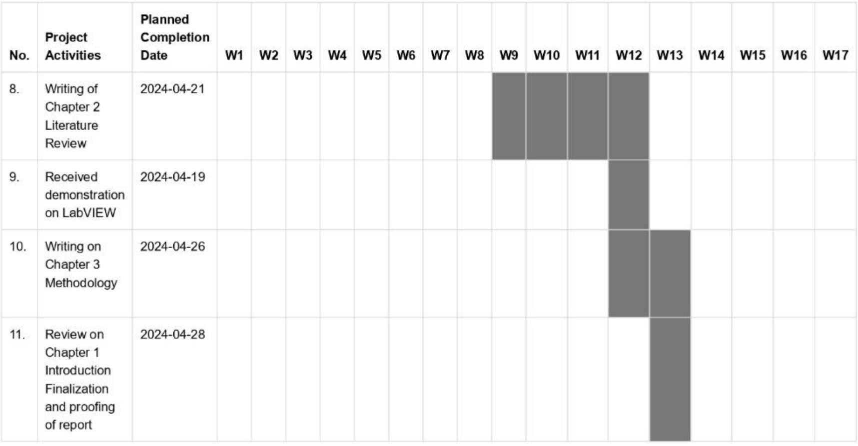

No.	Project Activities	Planned Completion Date	W1	W2	W3	W4	W5	W6	W7	W8	W9	W10	W11	W12	W13	W14	W15	W16	W17
8.	Writing of Chapter 2 Literature Review	2024-04-21									■	■	■	■					
9.	Received demonstration on LabVIEW	2024-04-19												■					
10.	Writing on Chapter 3 Methodology	2024-04-26												■	■				
11.	Review on Chapter 1 Introduction Finalization and proofing of report	2024-04-28													■				

Graph B-3: Gantt Chart of Final Year Project 1.

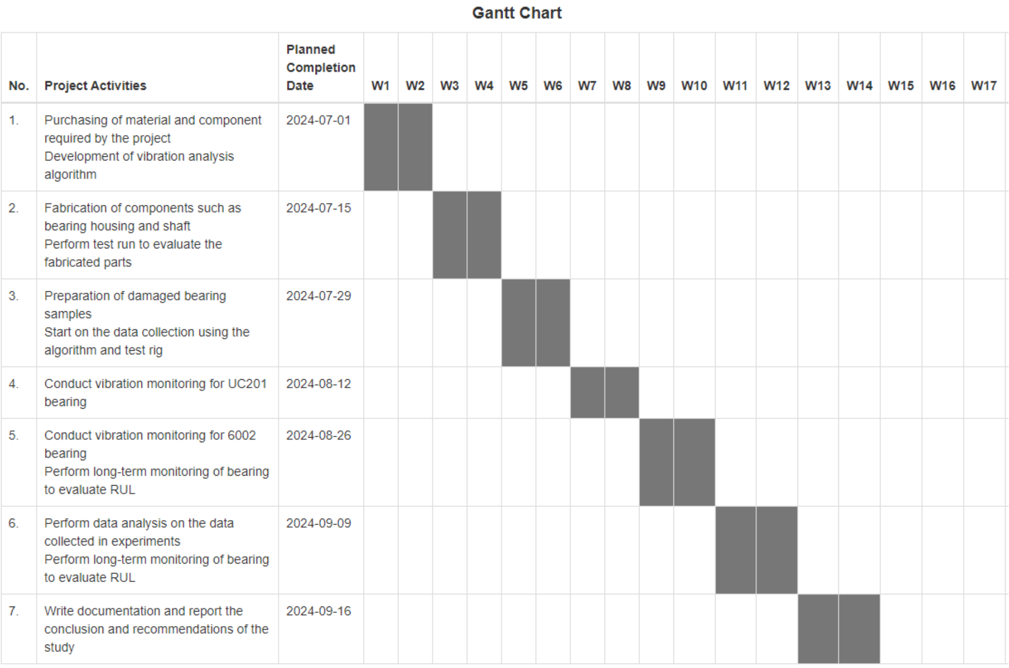

Gantt Chart

No.	Project Activities	Planned Completion Date	W1	W2	W3	W4	W5	W6	W7	W8	W9	W10	W11	W12	W13	W14	W15	W16	W17
1.	Purchasing of material and component required by the project Development of vibration analysis algorithm	2024-07-01	■	■															
2.	Fabrication of components such as bearing housing and shaft Perform test run to evaluate the fabricated parts	2024-07-15			■	■													
3.	Preparation of damaged bearing samples Start on the data collection using the algorithm and test rig	2024-07-29					■	■											
4.	Conduct vibration monitoring for UC201 bearing	2024-08-12							■	■									
5.	Conduct vibration monitoring for 6002 bearing Perform long-term monitoring of bearing to evaluate RUL	2024-08-26									■	■							
6.	Perform data analysis on the data collected in experiments Perform long-term monitoring of bearing to evaluate RUL	2024-09-09											■	■					
7.	Write documentation and report the conclusion and recommendations of the study	2024-09-16													■	■			

Graph B-4: Gantt Chart of Final Year Project 2.